

Appearance Modeling of Iridescent Feathers with Diverse Nanostructures

Supplemental Document

This document contains supplemental materials for our paper, *Appearance Modeling of Iridescent Feathers with Diverse Nanostructures*. In this document, we cover a list of topics that we did not get to discuss in detail in the main paper.

1 Overview on Iridescent Feathers and Barbules

As mentioned in the main paper, many types of birds have iridescent feathers thanks to specially arranged nanostructures in their barbules, and the exact coloration mechanisms vary among bird species. Table 1 is adapted from the main paper and lists the seven types of feathers studied in our work.

Species	Major coloration scheme
Rock dove (<i>columba livia</i>)	Thin film interference from a keratin cortex
European starling (<i>sturnus vulgaris</i>)	A keratin thin film on top of a basal melanin layer
Common bronzewing (<i>phaps chalcoptera</i>)	Multiple layers of melanosomes with regular spacing
Anna's hummingbird (<i>calypte anna</i>)	Layers of pancake-shaped, air-filled melanosomes
Common mallard (<i>anas platyrhynchos</i>)	2D photonic crystal: solid melanosomes in a hexagonal grid
Black-billed magpie (<i>pica hudsonia</i>)	2D photonic crystal: air-filled melanosomes in a hexagonal grid
Indian peafowl (<i>pavo cristatus</i>)	2D photonic crystal: melanosomes and air channels in a rectangular grid

Table 1: An overview of the different types of feather barbules studied in this work. In these descriptions, a melanosome refers to a nano-sized structure that contains melanin. Melanosomes are considered rod-shaped, except in hummingbird feathers, where they are described as pancake-shaped.

In this section, we provide detailed information on each type of feather's barbule structures. Since our wave simulations assume translational symmetry in all barbules, we only model the cross section of each type of barbule. For each type of barbule we consider in this work, we have developed procedural code for random barbule geometry generation, and each run of the code produces a unique configuration of a barbule. Barbules of the same type, procedurally generated, are guaranteed to be overall similar, with geometric properties such as average layer thicknesses and average lattice periods accurately modeled. Example cross section models for each type of barbule will be provided in each subsection.

1.1 Rock dove

Rock dove neck feathers exhibit a two-color iridescence caused by thin film interference from the keratin cortex of each barbule (Nakamura et al., 2008). Within the keratin cortex, the interior of each barbule contains air and a collection of spherical melanin granules, as shown in Fig. 1. The air outside and inside each barbule, together with the keratin cortex, forms an air-keratin-air thin film structure.

The feathers on the upper part of a rock dove's neck appear green at normal incidence and purple at larger illumination or viewing angles. The keratin cortex layers in these green-colored barbules have an average thickness of 595nm, and the rock dove BRDFs demonstrated in this work are derived with the 595nm cortex barbule models. In our renderings of the rock dove feather assembly, we also included

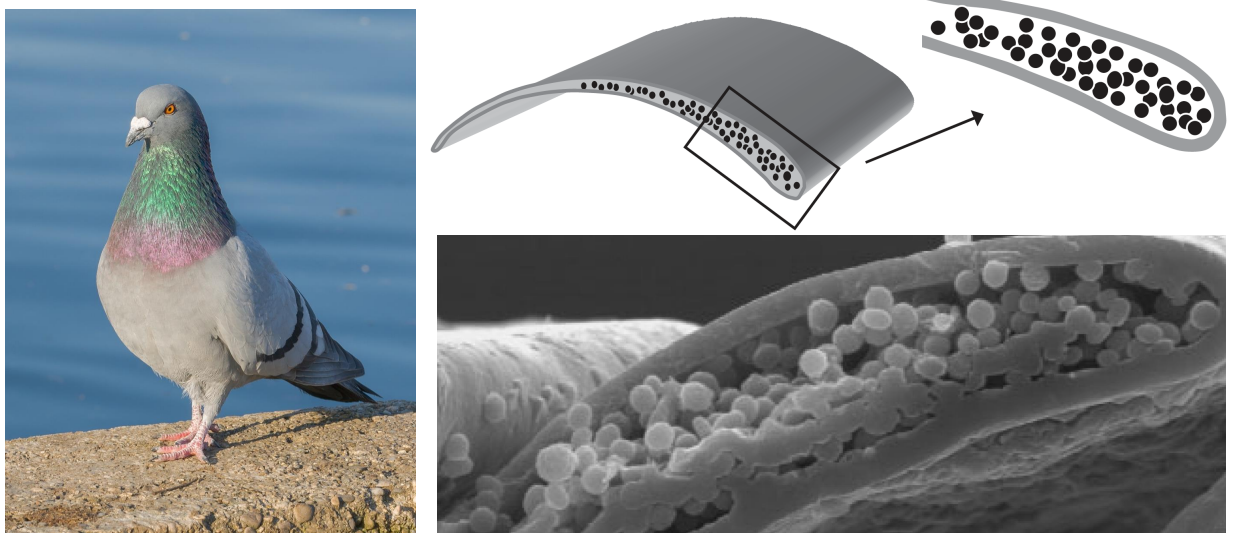


Figure 1: A rock dove with green and purple iridescent feathers and its feather barbule structure.

feathers on the lower part of the neck, which appear purple at normal incidence and turn green at larger angles. The keratin thin films in these purple barbules are modeled as 530nm thick. For the transition region, we also modeled barbules whose cortex thicknesses are somewhere between 530nm and 595nm .

Our geometric modeling of rock dove barbules focuses on modeling the keratin thin films with desired thicknesses. An entire barbule from a rock dove feather has a cross section around $40\mu\text{m}$ wide (Nakamura et al., 2008), and the barbule is highly curved, with a long and thin tail that does not contain many melanin granules, as shown in Fig. 1. In a rock dove feather, the long tail in each barbule is, most of the time, covered by the thicker end of another neighboring barbule. Thus, we only model the exposed parts of the barbules, which are around $20\mu\text{m}$. Examples of our geometric models are shown in Fig. 2.

In each barbule cross section in Fig. 2, the two light gray regions represent the thin keratin layers at the top and bottom of the barbules. The white regions inside the barbules represent air, and the black-gray regions have varying index of refraction (IOR), modeling a volume packed with numerous melanin granules. The varying IORs are computed from the estimated percentages of melanin and air inside the barbules. The keratin layer at the top of each barbule, placed in between the air outside and inside the barbule, is most responsible for the green-purple coloration, while the melanin underneath also modulates the color and contributes to spatial variations along each barbule.

1.2 European Starling

The European starling is a bird whose feathers exhibit weak iridescence, with colors ranging from light green to light purple. The structural coloration in starling barbules is caused by another type of thin film, as shown in the barbule TEM in Fig. 3. The entire starling barbule is filled with keratin, and cylindrical melanosomes are distributed in the keratin hosting medium. The arrangements of melanosomes seem to be very organized near the barbule top surface (and arguably also the bottom surface), as these melanosomes grow along the surfaces and approximately form a connected layer. Importantly, the single

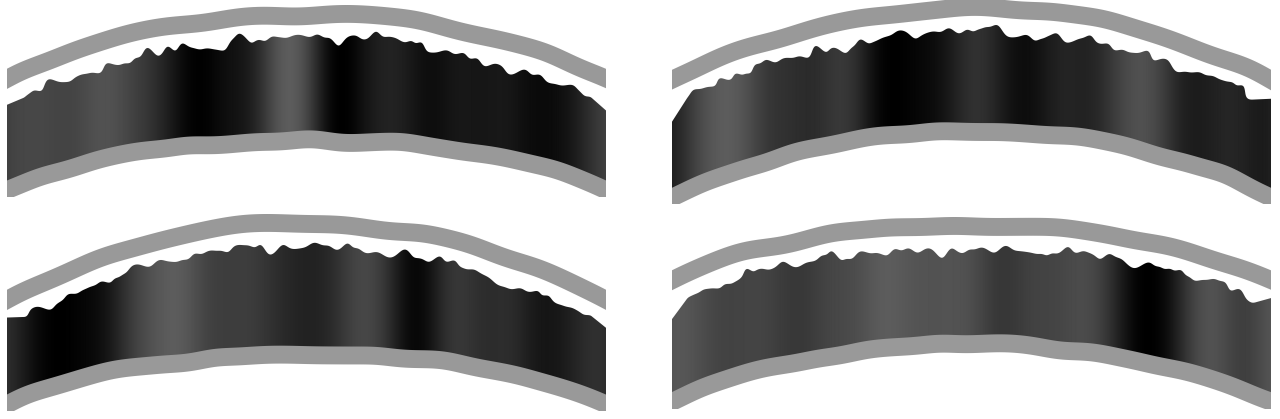


Figure 2: Examples of procedurally generated rock dove barbule cross sections.

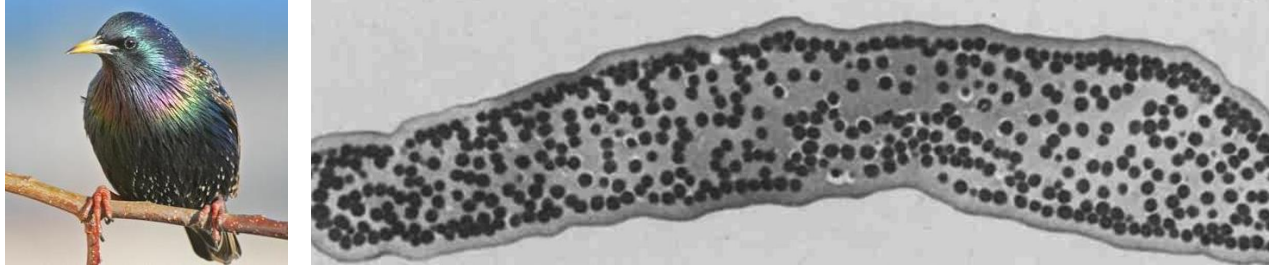


Figure 3: An European starling and the its feather barbule structure TEM.

layer of melanosomes near the barbule top surface gives rise to a keratin thin film, in between the air outside of the barbule and the melanosome layer itself. This air-keratin-melanin arrangement leads to the unique, weak iridescence in starling barbules.

As shown in Fig. 3, starling feathers have varying colors, and the exact colors are modulated by the keratin thin films in the barbules (Freyer et al., 2021). The starling BRDFs demonstrated in our work model light green chest feathers on starlings. In these green colored barbules, the keratin thin films are around 320nm thick, and the diameters of the melanosomes are on average 250nm (Freyer et al., 2021). In brown, purple, and light blue colored feathers, the keratin cortex thickness ranges from 300nm to 440nm , while the average melanosome diameter is about the same across these barbules.

According to the description in (Freyer et al., 2021), starling barbules are relatively small, and our starling barbule cross section models are $25\mu\text{m}$ wide. Some example, procedurally generated cross section models are in Fig. 4. In each of the cross sections, the gray regions at the top and bottom are the keratin layers, and the black regions near the top and bottom of the barbule represent two layers of melanosomes. In our simplified model, instead of modeling the melanosomes one by one, we approximate them as connected layers in order to accelerate our geometry processing steps in our wave simulations. The middle region in each barbule, consisting of melanosomes randomly scattered in the keratin hosting medium, is again modeled as a region with varying IOR—mixing between the IORs of keratin and melanin.

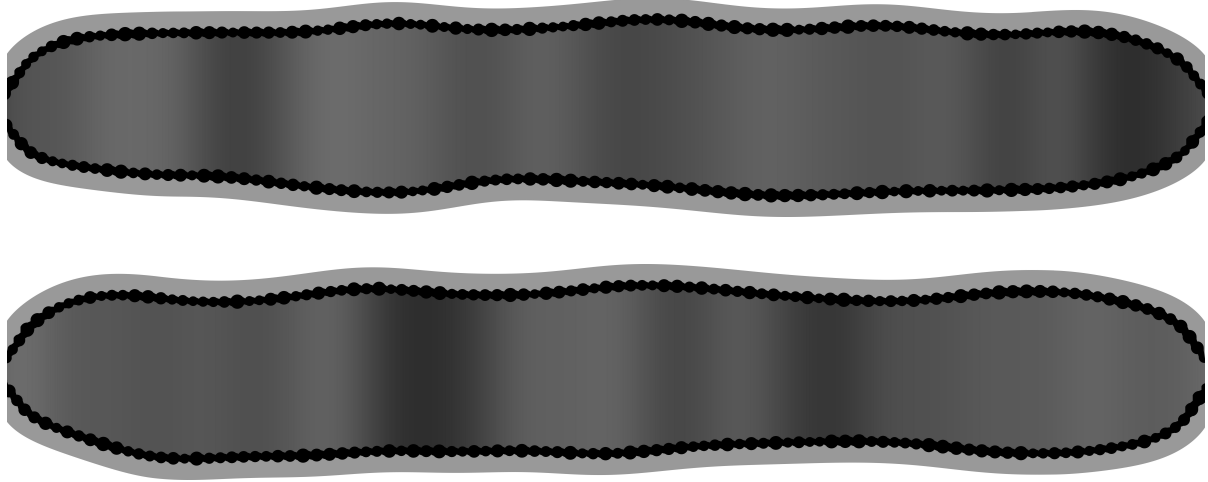


Figure 4: Examples of procedurally generated starling barbule cross sections.

1.3 The Common Bronzewing

The common bronzewing is a beautiful bird, with a rainbow of feather colors—from red, orange, and yellow to green, cyan, and blue. These dramatic iridescent colors are caused by a classic multilayer structure, as shown in Fig. 5. Each barbule in the bronzewing feather contains two stacks of melanosome layers, and in each layer, melanosomes are very neatly organized. The diameters of the melanosomes are approximately constant, and the spacings between the layers are close to uniform.

The bronzewing BRDFs demonstrated in our work model red colored barbules. In these barbules, the average diameter of the melanosomes is around 99nm , and the spacing between each two melanosome layers in each stack is around 100nm (Xiao et al., 2014). Yellow, green, and blue barbules have smaller melanosome diameters (75 — 91nm) and/or layer spacings (63 — 98nm). The number of melanosome layers in each of the two stacks is modeled as $nL = 6$. Some example cross section models are in Fig. 6. Unfortunately, we were not able to find information on the size of bronzewing barbules, and our cross section models are chosen to be $40\mu\text{m}$ wide, a size comparable to (or slightly smaller than) the coherent area of common light sources. It might not be immediately obvious how the two cross sections presented in Fig. 6 are different, but our procedural code gives each barbule slightly different top and bottom surfaces (which are optically rough), and the size of each melanosome forming a layer is also randomized. This way, the BRDF computed from each barbule instance has unique patterns with rich details.

1.4 Anna's Hummingbird

Hummingbirds are stunning creatures in nature. There have been hundreds of hummingbird species discovered by biologists, and each type of hummingbird features some unique structural coloration—particularly on the crown and gorget feathers. Hummingbird barbules are probably the most unique among all types of barbules considered in this work: instead of classic multilayers or periodic structures forming photonic crystals, hummingbird barbules contain layers of pancake-shaped melanosomes, where each melanosome is filled with air bubbles. As shown in Fig. 7, these pancake-shaped melanosomes



Figure 5: A common bronzewing and the its feather barbule structure TEM.

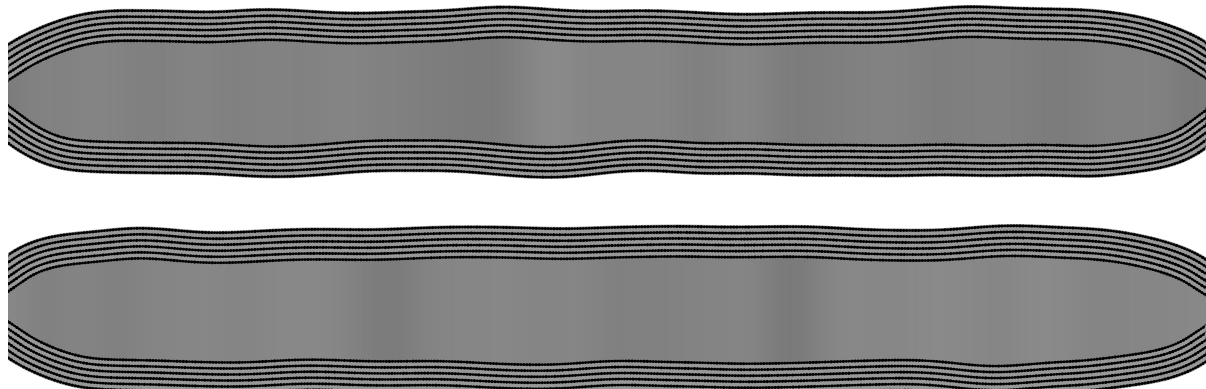


Figure 6: Examples of procedurally generated bronzewing barbule cross sections.

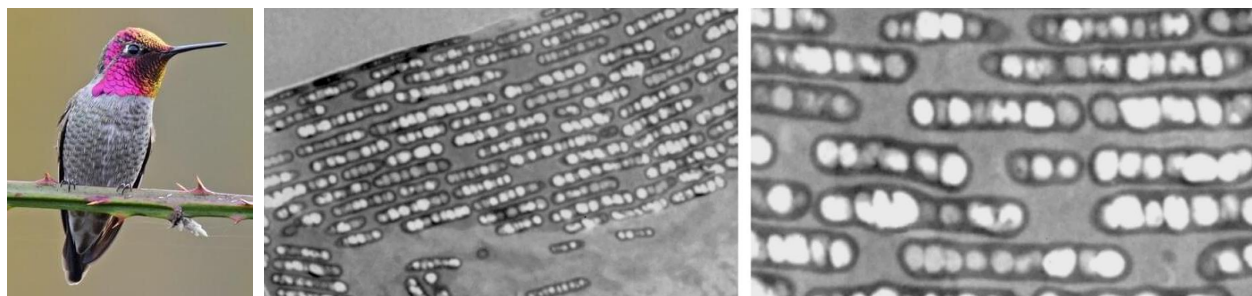


Figure 7: An Anna's hummingbird and the its feather barbule structure TEM.

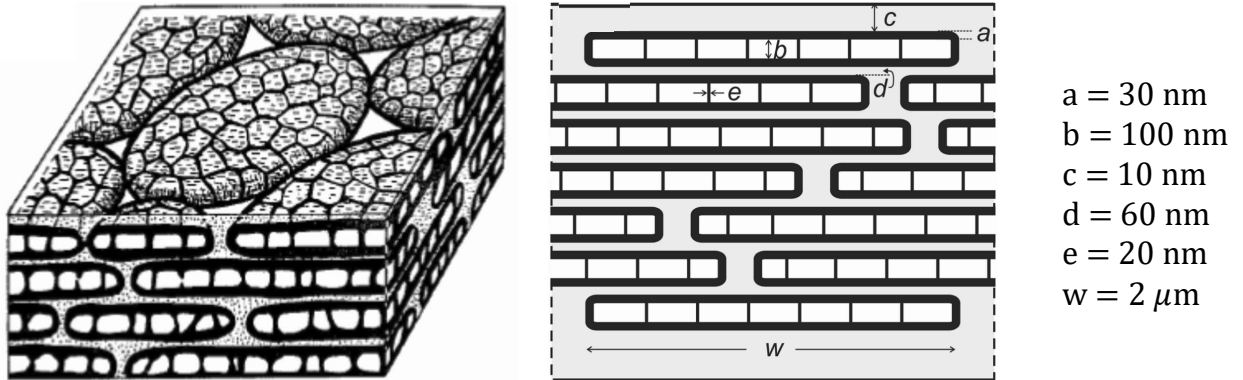


Figure 8: Geometric modeling parameters for hummingbird feather barbules.

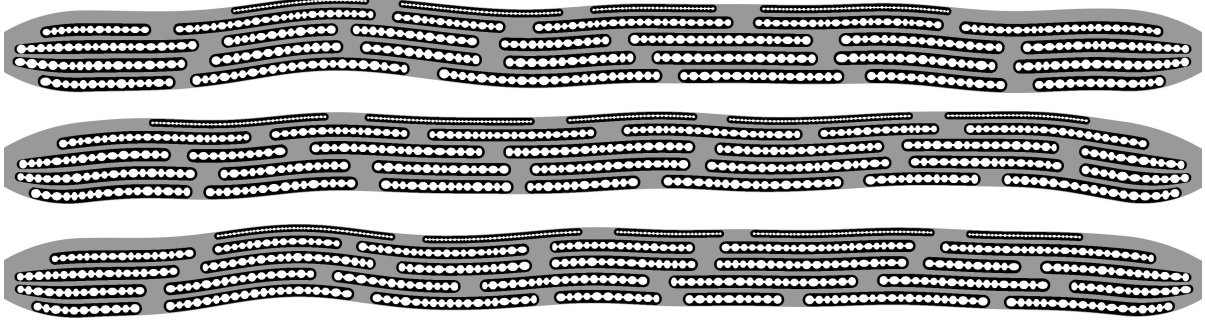


Figure 9: Examples of procedurally generated hummingbird barbule cross sections.

appear very organized in a barbule, and this complicated layer structure needs to be carefully described. Anna's hummingbird has been studied in (Giraldo et al., 2018), where the models and parameters shown in Fig. 8 were invented. Our code for generating hummingbird barbule cross sections was developed based on the model shown in Fig. 8, where we listed the model parameters used for Anna's hummingbird barbules. As mentioned in (Giraldo et al., 2018), the melanosomes in the topmost layer are slightly smaller than those in other layers, and we incorporated this feature in our procedural barbule generation. Examples of our geometric models are in Fig. 9, where the presented barbules, $15\mu\text{m}$ wide with five layers of melanosomes, are smaller than the barbules we simulate (so that the small features are easier to see). For deriving BRDFs, we use barbules that are $40\mu\text{m}$ wide with $nL = 12$ layers of melanosomes.

Our procedural code, if given different parameters, can generate models for barbules of many different types of hummingbirds. Interested readers can find a dataset of hummingbird barbule geometric parameters in (Eliason et al., 2020).

We mention that due to the pancaked-shaped melanosomes, a hummingbird barbule does not really possess translational symmetry, which our simulations assume. Rock dove barbules also do not have translational symmetry, mostly due to the spherical melanin granules in the interior. However, the structural colors in these two types of barbules are mostly modulated by layer thicknesses, which 2D cross sections can

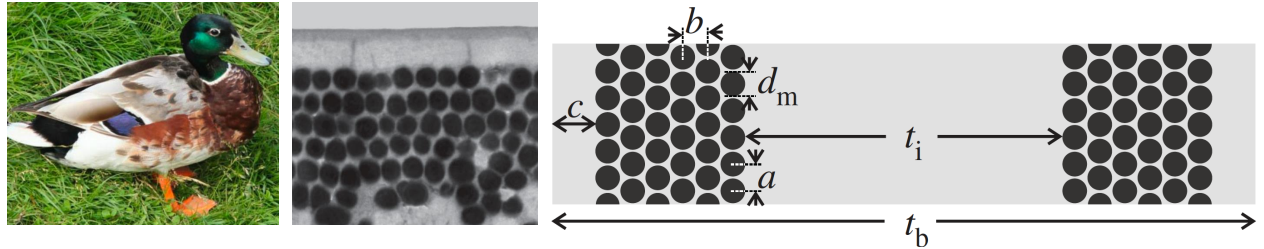


Figure 10: A male mallard and its feather barbule structure TEM, along with a model for the underlying 2D photonic crystal that describes the barbule structure, which we adopted from ([Stavenga et al., 2017](#)).

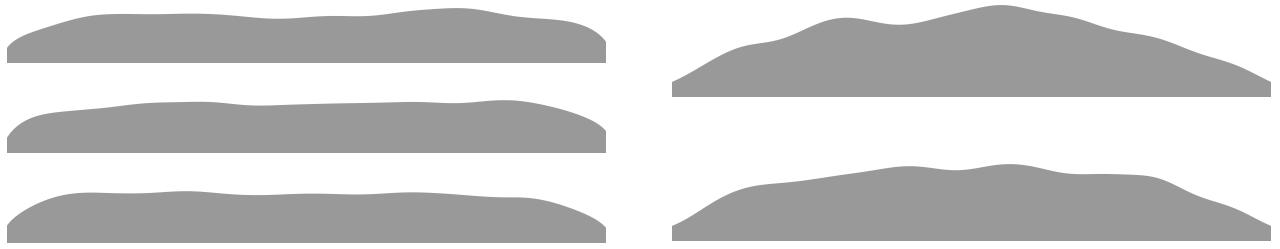


Figure 11: Examples of procedurally generated barbule top surfaces. Note that mallard and magpie barbule surfaces (left) are flatter than peacock barbule surfaces (right), which are mildly curved.

sufficiently model. This is why we find that using 2D geometric models and 2.5D simulations on these barbules lead to realistic appearance models for the feathers. In our main paper and some later sections in this document, we present comparisons between BRDFs of rock dove and hummingbird barbules computed from 2.5D and 3D simulations (that compute scattering from 3D barbule structures), and such comparisons also show that using 2.5D simulations are sufficient for the purpose of appearance modeling.

1.5 The Common Mallard

The common mallard has structurally colored feathers—blue wing feathers on male and female mallards and green head feathers on male mallards. These colors are caused by 2D photonic crystals formed by melanosomes arranged in hexagonal grids, within some keratin hosting media ([Stavenga et al., 2017](#)).

A common mallard and its feather barbule structure are illustrated in Fig. 10, along with the 2D photonic crystal formed by melanosome hexagonal grids. For barbules characterized by photonic crystals, our wave simulations rely on precomputations of the reflection coefficients of photonic crystals, which we realize with periodic FDTD simulations. However, even though the mallard barbule has two stacks of approximate photonic crystal structures, as shown in Fig. 10, we only simulate the top half of the structure—containing one stack of photonic crystal in an infinite half space filled with keratin. This is because each mallard barbule has spatially varying thickness, making it hard to choose specific values of t_b and t_i (see Fig. 10). Also, as shown in ([Stavenga et al., 2017](#)), modeling the top half of the structure is sufficient for analyzing the coloration. Thus, our modeling of the photonic crystal requires four parameters—the

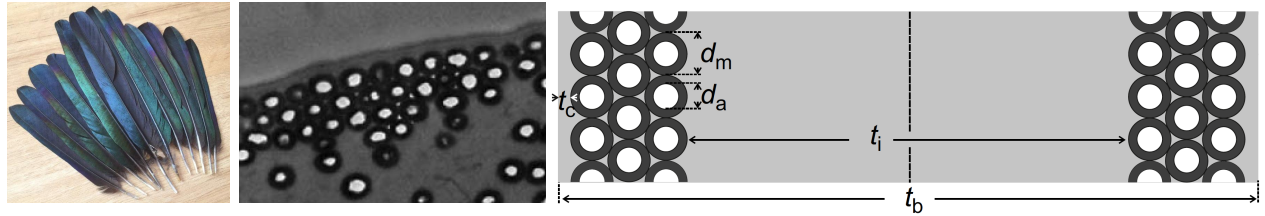


Figure 12: Some black-billed magpie feathers and the magpie barbule structure TEM, along with a model for the underlying 2D photonic crystal, adopted from ([Stavenga et al., 2018](#)).

horizontal spacing a and vertical spacing b between the melanosomes, the keratin cortex thickness c , and the melanosome diameter d_m . For green head feathers, we use $a = 200\text{nm}$, $b = 180\text{nm}$, $c = 280\text{nm}$, and $d_m = 130\text{nm}$. For blue wing feathers, we use $a = 180\text{nm}$, $b = 160\text{nm}$, $c = 260\text{nm}$, and $d_m = 130\text{nm}$. In both cases, we model $nL = 6$ layers of melanosomes in the hexagonal grid.

Since the reflection coefficients from photonic crystal structures are precomputed, we do not need to explicitly represent any melanosome when modeling barbules. In fact, as mentioned in the main paper, only the top surface of each barbule needs to be explicitly generated. Each barbule is again modeled as $40\mu\text{m}$ wide and examples of moderately rough barbule top surfaces are shown in Fig. 11 (left).

1.6 Black-Billed Magpie

The black-billed magpies have colorful tails, with structural coloration caused by another type of 2D photonic crystal, which consists of hollow (air-filled) melanosomes arranged in a hexagonal grid, embedded in a keratin hosting medium ([Han et al., 2017; Stavenga et al., 2018](#)).

Magpie feathers and a magpie barbule TEM are illustrated in Fig. 12, together with a model for the underlying 2D photonic crystal. In our periodic FDTD simulations, we again only simulate the top half of the photonic crystal structure, containing one stack of hollow melanosomes. Our modeling of the photonic crystal requires three parameters—the melanosome diameter d_m , the interior air channel diameter d_a , and the keratin cortex thickness t_c , as shown in Fig. 12. Our magpie BRDFs presented in this work feature violet colored barbules, corresponding to parameter values $d_m = 180\text{nm}$, $d_a = 90\text{nm}$, and $t_c = 130\text{nm}$. Magpie barbules of other colors have different parameter values, with d_m ranging from 160nm to 200nm , d_a ranging from 70nm to 100nm , and t_c ranging from 75nm to 160nm ([Han et al., 2017](#)). There are usually $nL = 2$ or 3 layers of hollow melanosomes in the modeled structures.

Same as for mallard barbules, we only model the moderately rough top surfaces in magpie barbules, and each barbule is modeled as $40\mu\text{m}$ wide.

1.7 Indian Peafowl

The Indian peafowl, also known as the common peacock, also exhibits brilliant structural colors on its neck and tail feathers. Specifically, a peacock tail feather has a unique eye pattern, whose colors are entirely structure-based. The structural colors in peacock feathers are caused by a special type of 2D photonic crystal, consisting of melanosomes and air channels in a rectangular grid, arranged in a keratin

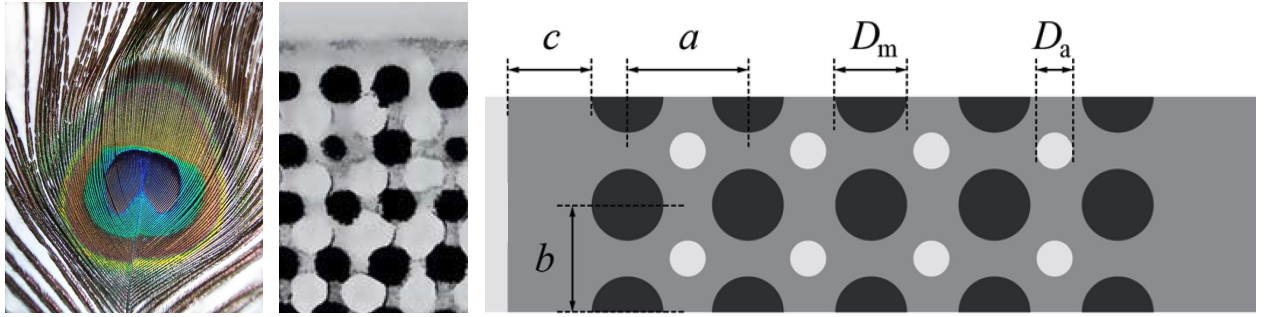


Figure 13: A peacock feather and the peacock barbule TEM, along with a model for the underlying 2D photonic crystal, adopted from ([Freyer and Stavenga, 2020](#)).

hosting medium ([Freyer and Stavenga, 2020](#)).

A peacock feather and peacock barbule TEM are illustrated in Fig. 13, together with the underlying 2D photonic crystal model. Peacock barbules also contain two stacks of photonic crystals, and we only simulate the top stack. Our modeling requires five parameters—the vertical period a , the horizontal period b , the keratin cortex thickness c , the melanosome diameter D_m , and the air channel diameter D_a . We present BRDFs of the yellow colored barbules in our work, which correspond to the yellow ring in the eye pattern in Fig. 13. The parameters are given as $a = 190\text{nm}$, $b = 160\text{nm}$, $c = 90\text{nm}$, $D_m = 120\text{nm}$, and $D_a = 55\text{nm}$, and we model $nL = 6$ layers of melanosomes and $nL - 1 = 5$ layers of air channels in the stack. Unfortunately, the geometric parameters corresponding to some other parts of the eye pattern, as provided in ([Freyer and Stavenga, 2020](#)), gave rise to structural color predictions different from what we observed from our measurements (so we did not manage to render a peacock feather in the main paper).

Peacock barbules are curved, so in our geometric models we use curved top surfaces in their barbule models, as shown in Fig. 11 (right). Each barbule is again modeled as $40\mu\text{m}$ wide.

As a summary, we comment again on the barbule sizes chosen in our simulations: rock dove barbules are $20\mu\text{m}$ wide and starling barbules are $25\mu\text{m}$ wide, and these numbers roughly reflect the true widths of the (exposed part of the) barbules. Bronzewing, hummingbird, mallard, magpie, and peacock barbules are modeled to be $40\mu\text{m}$ wide, our default size, as the true sizes of these barbules are either unknown or much larger than the coherence areas of common light sources.

2 Behind 2.5D Fast Wave Simulations

In Section 4 of our main paper, we presented a 2.5D approximate wave simulator used for computing scattering from different types of barbules. Here we explain some ideas and concepts in more details and provide derivations of a few equations, as promised in the main paper.

2.1 Periodic FDTD Simulations and Diffraction Modes

In this section, we expand on Section 4.3 in our main paper. To promote understanding, here we explicitly write out the analytical expressions of the incident field and reflected field quantities relevant to our

periodic FDTD simulations.

In each of our 2D FDTD simulation on a given photonic crystal structure, we are given a wavelength λ and an incident direction $\omega_i \sim (\theta_i, \phi_i)$, where θ_i, ϕ_i come from our parameterization of ω_i in the main paper. We define a plane wave that illuminates the photonic crystal

$$\mathbf{E}_i(\mathbf{r}) = \vec{\mathcal{E}}_i \cdot e^{j\mathbf{k}_i \cdot \mathbf{r}}; \quad \mathbf{H}_i(\mathbf{r}) = \vec{\mathcal{H}}_i \cdot e^{j\mathbf{k}_i \cdot \mathbf{r}} \quad (\text{S.1})$$

where \mathbf{k}_i is the wave vector of the plane wave. Note that ω_i is defined to point outward from the scattering surface, so we have $\mathbf{k}_i = -2\pi/\lambda \cdot \langle \cos \theta_i \sin \phi_i, \sin \theta_i, \cos \theta_i \cos \phi_i \rangle$. Moreover, the vectors $\vec{\mathcal{E}}_i$, $\vec{\mathcal{H}}_i$, and \mathbf{k}_i are mutually perpendicular.

The field quantities in our periodic domain satisfy a Bloch boundary condition (BC), which is associated with the wave vector \mathbf{k}_i and the domain's periodicity Δ_x . Specifically, the reflected field from the photonic crystal satisfies:

$$\mathbf{E}_r(\mathbf{r} + \Delta_x \vec{\mathbf{x}}) = e^{jk_x \Delta_x} \mathbf{E}_r(\mathbf{r}); \quad \mathbf{H}_r(\mathbf{r} + \Delta_x \vec{\mathbf{x}}) = e^{jk_x \Delta_x} \mathbf{H}_r(\mathbf{r}) \quad (\text{S.2})$$

where $k_x = -2\pi/\lambda \cdot \cos \theta_i \sin \phi_i$.

The reflected field from the photonic crystal structure can be decomposed into a weighted sum of plane waves, and given the constraints in Eq. S.2, we know that the reflected field contains only a few plane wave components that each propagate in a “valid” direction. Mathematically, we have

$$\mathbf{E}_r(\mathbf{r}) = \sum_{m=m_1}^{m_2} \vec{\mathcal{E}}_m \cdot e^{j\mathbf{k}_m \cdot \mathbf{r}}; \quad \mathbf{H}_r(\mathbf{r}) = \sum_{m=m_1}^{m_2} \vec{\mathcal{H}}_m \cdot e^{j\mathbf{k}_m \cdot \mathbf{r}} \quad (\text{S.3})$$

and the wavevectors \mathbf{k}_m can further be written as

$$\mathbf{k}_m = \frac{2\pi}{\lambda} \cdot \langle \cos \theta_i \sin \phi_m, -\sin \theta_i, \cos \theta_i \cos \phi_m \rangle \quad (\text{S.4})$$

where $\sin \phi_m = -\sin \phi_i + m \cdot \frac{\lambda}{\cos \theta_i \Delta_x}$

Note that the longitudinal angle of the reflected directions should always be $-\theta_i$, because the 2D photonic crystals reflect specularly along the y -axis, thanks to their translational symmetry. The constraints on the azimuthal angles ϕ_m can be easily derived from combining Eq. S.2 and Eq. S.3, and the lower and upper bounds of the integer m can be determined by the requirement that $\sin \phi_m \in [-1, 1]$.

Therefore, an ideal 2D photonic crystal, when illuminated by an incident plane wave, can in general reflect light into a discrete set of directions, corresponding to the different diffraction modes of the photonic crystal structure. Also, the larger Δ_x is, the more diffraction modes there tend to be, as can be seen from Eq. S.4. On the other hand, if the photonic crystal period is very small, such that $\Delta_x \leq 0.5\lambda$, there will only be one diffraction mode. This is because in Eq. S.4, we have $\sin \phi_i, \cos \theta_i \in [-1, 1]$, and if $\lambda/\Delta_x \geq 2$, then any value of m other than 0 will make $|\sin \phi_m|$ exceed 1, thereby making $\sin \phi_m$ an invalid sine value. Thus, $m = 0$ corresponds to the only possible diffraction order, which is associated with reflection into the exact specular direction.

2.2 Some Derivations of Equations

We also hope to provide derivations for a few equations in the main paper.

Deriving Eq. 8

We derive Eq. 8 in the paper, which computes the total reflected power per unit length from a barbule:

$$\Phi_r(\lambda, \omega_i) = c_0 \cos \theta_i \int_{-\pi/2}^{\pi/2} |\vec{\mathcal{E}}_s(\lambda, \omega_i; \phi_o)|^2 d\phi_o \quad (\text{S.5})$$

where $\vec{\mathcal{E}}_s(\lambda, \omega_i; \phi_o)$ is a far field quantity describing the scattered electric field, and $\Phi_r(\lambda, \omega_i)$ is the total reflected power, as introduced in the main paper.

To compute the barbule's total reflected power per unit length, we evaluate the barbule's scattered field along a semicircle with radius ρ . This semicircle represents a slice from a cylinder with radius ρ , and the cylinder's longitudinal axis coincides with the barbule's longitudinal axis, i.e. the y -axis. The point on the semicircle corresponding to the azimuthal angle ϕ_o is given by $\mathbf{P}(\rho, \phi_o) = (\rho \sin \phi_o, 0, \rho \cos \phi_o)$, where $\phi_o \in (-\pi/2, \pi/2)$. Using Eq. 7 from the main paper, the scattered field at $\mathbf{P}(\rho, \phi_o)$ is given by

$$\begin{aligned} \mathbf{E}_s(\lambda, \omega_i; \mathbf{P}) &= e^{jk\rho} \sqrt{1/\rho} \cdot \vec{\mathcal{E}}_s(\lambda, \omega_i; \phi_o) \\ \mathbf{H}_s(\lambda, \omega_i; \mathbf{P}) &= e^{jk\rho} \sqrt{1/\rho} \cdot \vec{\mathcal{H}}_s(\lambda, \omega_i; \phi_o) \end{aligned} \quad (\text{S.6})$$

where $\vec{\mathcal{H}}_s(\lambda, \omega_i; \phi_o)$ is the magnetic field analog to $\vec{\mathcal{E}}_s(\lambda, \omega_i; \phi_o)$.

The time-averaged Poynting vector at \mathbf{P} , associated with the vector irradiance at \mathbf{P} (Xia et al., 2020), is

$$\begin{aligned} \mathbf{S}(\lambda, \omega_i; \mathbf{P}) &= \frac{1}{2} \operatorname{Re} [\mathbf{E}_s(\lambda, \omega_i; \mathbf{P}) \times \mathbf{H}_s^*(\lambda, \omega_i; \mathbf{P})] \\ &= \frac{1}{2\rho} \operatorname{Re} [\vec{\mathcal{E}}_s(\lambda, \omega_i; \phi_o) \times \vec{\mathcal{H}}_s^*(\lambda, \omega_i; \phi_o)] \end{aligned} \quad (\text{S.7})$$

The far field quantities $\vec{\mathcal{E}}_s$ and $\vec{\mathcal{H}}_s$ are highly related, and one can be computed from the other. Their magnitudes are in fact related by a constant scale factor, and we have:

$$\begin{aligned} |\mathbf{S}(\lambda, \omega_i; \mathbf{P})| &= \frac{\sqrt{\varepsilon_0/\mu_0}}{2\rho} |\vec{\mathcal{E}}_s(\lambda, \omega_i; \phi_o)|^2 \\ &= \frac{c_0}{\rho} |\vec{\mathcal{E}}_s(\lambda, \omega_i; \phi_o)|^2 \end{aligned} \quad (\text{S.8})$$

where ε_0 , μ_0 , and c_0 are defined in the main paper. The total reflected power per unit length can be computed by integrating the vector irradiance along the semicircle we consider, i.e.

$$\Phi_r(\lambda, \omega_i) = \int_{\Omega} \mathbf{S}(\lambda, \omega_i; \mathbf{P}) \cdot \mathbf{n}(\mathbf{P}) d\mathbf{P} \quad (\text{S.9})$$

where $\mathbf{n}(\mathbf{P})$ is the normal vector of the semicircle at point \mathbf{P} . For an incident direction $\omega_i \sim (\theta_i, \phi_i)$, the Poynting vector forms an angle of θ_i with the normal for each point \mathbf{P} . Thus, we have:

$$\begin{aligned} \Phi_r(\lambda, \omega_i) &= \cos \theta_i \int_{\Omega} |\mathbf{S}(\lambda, \omega_i; \mathbf{P})| d\mathbf{P} \\ &= \cos \theta_i \int_{-\pi/2}^{\pi/2} \frac{c_0}{\rho} |\vec{\mathcal{E}}_s(\lambda, \omega_i; \phi_o)|^2 d\rho d\phi_o \\ &= c_0 \cos \theta_i \int_{-\pi/2}^{\pi/2} |\vec{\mathcal{E}}_s(\lambda, \omega_i; \phi_o)|^2 d\phi_o \end{aligned} \quad (\text{S.10})$$

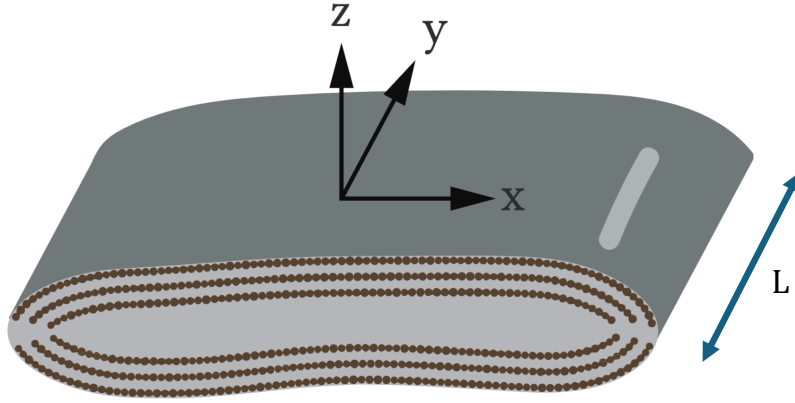


Figure 14: Illustration of a 3D barbule segment that has an invariant cross section, with a length of L along the longitudinal axis.

Deriving Eq. 12

We also briefly explain how we arrived at Eq. 12 in the main paper:

$$\int_{H^2} \hat{f}_r(\lambda, \omega_i, \omega_o) (\hat{\mathbf{z}} \cdot \omega_o) d\omega_o = \cos \theta_i \int_{-\pi/2}^{\pi/2} U(\lambda, \omega_i; \phi_o) d\phi_o \quad (\text{S.11})$$

where \hat{f}_r is the smooth, average BRDF we construct for each type of barbule, and U was defined in the main paper, i.e.

$$U(\lambda, \omega_i; \phi_o) = \frac{c_0}{M} \sum_{m=1}^M \frac{|\tilde{\mathcal{E}}_s^{(m)}(\lambda, \omega_i; \phi_o)|^2}{\Phi_i(\lambda, \omega_i)} \quad (\text{S.12})$$

recalling that M barbule instances need to be simulated to construct a barbule BRDF, and $\tilde{\mathcal{E}}_s^{(m)}(\lambda, \omega_i; \phi_o)$ is the far field scattered field quantity of the instance m . $\Phi_i(\lambda, \omega_i)$ is the total incident power (per unit length) on each barbule surface, which is considered constant across all the barbule instances.

To explain Eq. S.11 (or Eq. 12 in the main paper), we consider a 3D barbule segment that has an invariant cross section, with a length of L along the longitudinal axis, as shown in Fig. 14.

We multiply a factor of $L \cdot \Phi_i(\lambda, \omega_i)$ to both sides of Eq. S.11. The left hand side of Eq. S.11 becomes

$$L \cdot \Phi_i(\lambda, \omega_i) \int_{H^2} \hat{f}_r(\lambda, \omega_i, \omega_o) (\hat{\mathbf{z}} \cdot \omega_o) d\omega_o \quad (\text{S.13})$$

Note that since $\Phi_i(\lambda, \omega_i)$ is the total incident power per unit length on a barbule with translational symmetry, the quantity $L \cdot \Phi_i(\lambda, \omega_i)$ represents the total incident power of the light source on the 3D barbule segment with length L . Since \hat{f}_r is the constructed BRDF, the quantity in Eq. S.13 represents the total reflected power from the 3D barbule segment.

Moreover, using the definition in Eq. S.12 (Eq. 10 in the main paper), the right hand side of Eq. S.11, multiplied by $L \cdot \Phi_i(\lambda, \omega_i)$, becomes

$$\frac{L c_0 \cos \theta_i}{M} \sum_{m=1}^M \int_{-\pi/2}^{\pi/2} |\vec{\mathcal{E}}_s^{(m)}(\lambda, \omega_i; \phi_o)|^2 d\phi_o \quad (\text{S.14})$$

Using Eq. S.5 (Eq. 8 from the main paper), Eq. S.14 simplifies to

$$\frac{L}{M} \sum_{m=1}^M \Phi_r(\lambda, \omega_i) \quad (\text{S.15})$$

which is the average total reflected power per unit length from the simulated barbules multiplied by the length L , giving rise to the expected total reflected power from the 3D barbule segment. Thus, when constructing the average BRDF \hat{f}_r for a type of barbule, we hope to equate Eq. S.13 and Eq. S.14, leading to the requirement in Eq. S.11, or Eq. 12 in the main paper.

3 Smooth Average BRDF and Analytical Fitting

In the previous section, we discussed the smooth, analytical BRDF \hat{f}_r that represents the average reflectance from each type of barbule, which we introduced in Section 5.1 of the main paper. In Section 5.2 of our main paper, we presented our analytical fitting pipeline for computing \hat{f}_r from simulation data on each type of barbule, and this BRDF \hat{f}_r is constructed from three important model parameters, m_{eff} , ϕ_{eff} , and F_{eff} , which are functions of the wavelength λ and incident direction ω_i . The first two parameters are obtained from analytical fitting, and the last parameter is determined from making \hat{f}_r satisfy Eq. S.11 (or Eq. 12 in the main paper). Here, we hope to demonstrate our analytical fitting, by comparing the average reflectance functions computed from simulations to the fitted GGX models. We would also like to show how the BRDF model parameters m_{eff} , ϕ_{eff} , and F_{eff} change with incident conditions (e.g. ω_i).

As shown in the next few pages, our analytical fitting of the average reflectance functions from all types of barbules seem to be highly accurate. The parameter maps with respect to $\cos \theta_i$ and $\cos \phi_i$ reveal the ways how m_{eff} , ϕ_{eff} , and F_{eff} change with the incident direction ω_i . All the parameter maps were made for a single wavelength of $\lambda = 400\text{nm}$, and unfortunately we cannot present the parameter maps corresponding to all the 50 wavelengths we simulated.

m_{eff} , the effective roughness parameter, varies with $\cos \theta_i$ and $\cos \phi_i$ in different fashions for different types of barbules, as m_{eff} depends on the roughness level and curvature of each type of barbule. Specifically, rock dove and peacock barbules are curved, giving rise to unique-looking parameter maps for m_{eff} .

ϕ_{eff} , the effective incident direction parameter, was introduced to improve the accuracy of the fitting. For nearly flat barbules in starlings, bronzewings, hummingbirds, mallards, and magpies, we almost always have $\phi_{\text{eff}} \approx \phi_i$ at each ω_i , while for modeling curved barbules, the ϕ_{eff} becomes less predictable, as shown in Fig. 15 and Fig. 21. This is because different parts of the curved barbules form different angles with incident light coming from one direction, resulting in reflection into a range of directions. With iridescence, light of different colors can be reflected into different directions, as shown in the rock dove and peacock BRDFs. Thus, the peak reflectance from a curved barbule may occur at different directions for different wavelengths, making ϕ_{eff} a nontrivial function of λ and ω_i .

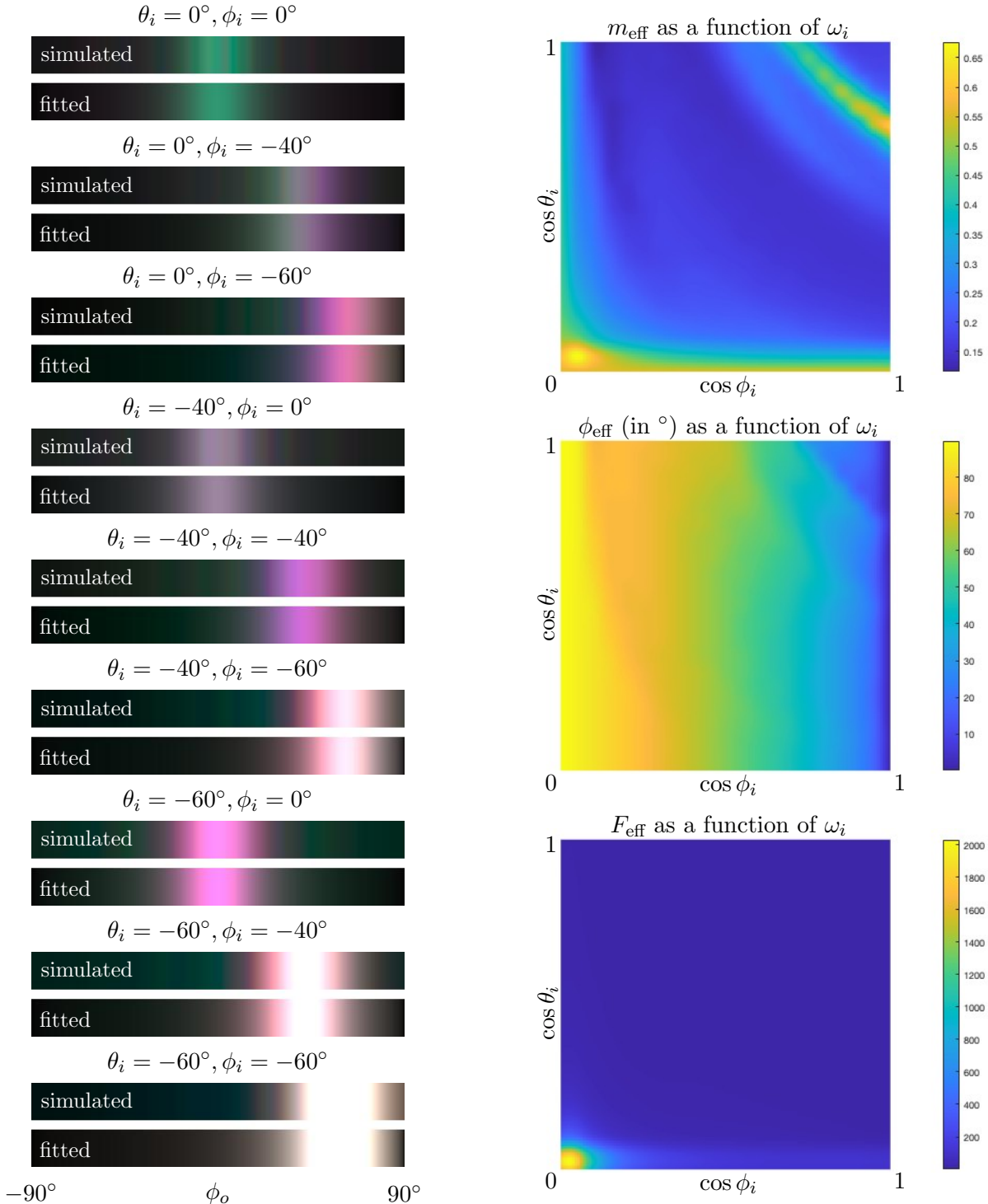


Figure 15: We compare the average reflectance from rock dove barbules, computed from simulation data, to the analytical average reflectance function fitted to a GGX model. We demonstrate our comparison for a few incident directions, in the specular cone of each incident direction. We also show how the BRDF parameters change with the incident direction, at a fixed wavelength of $\lambda = 400\text{nm}$.

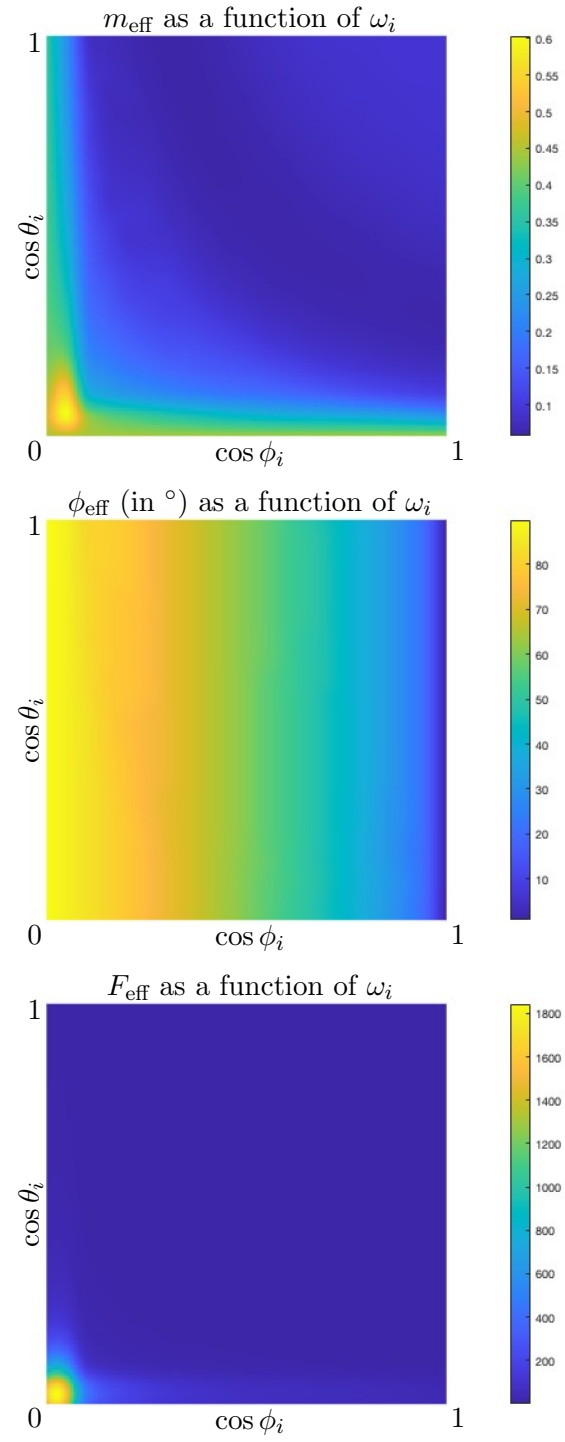
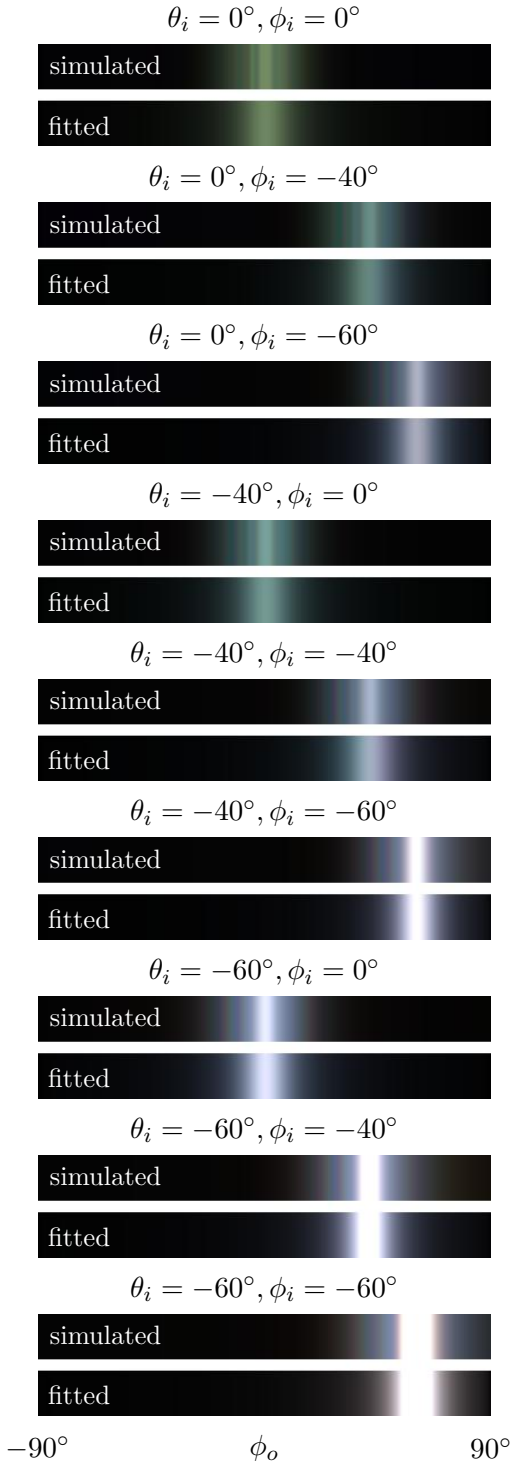


Figure 16: We compare the average reflectance from European starling barbules, computed from simulation data, to the analytical average reflectance function fitted to a GGX model. We demonstrate our comparison for a few incident directions, in the specular cone of each incident direction. We also show how the BRDF parameters change with the incident direction, at a fixed wavelength of $\lambda = 400nm$.

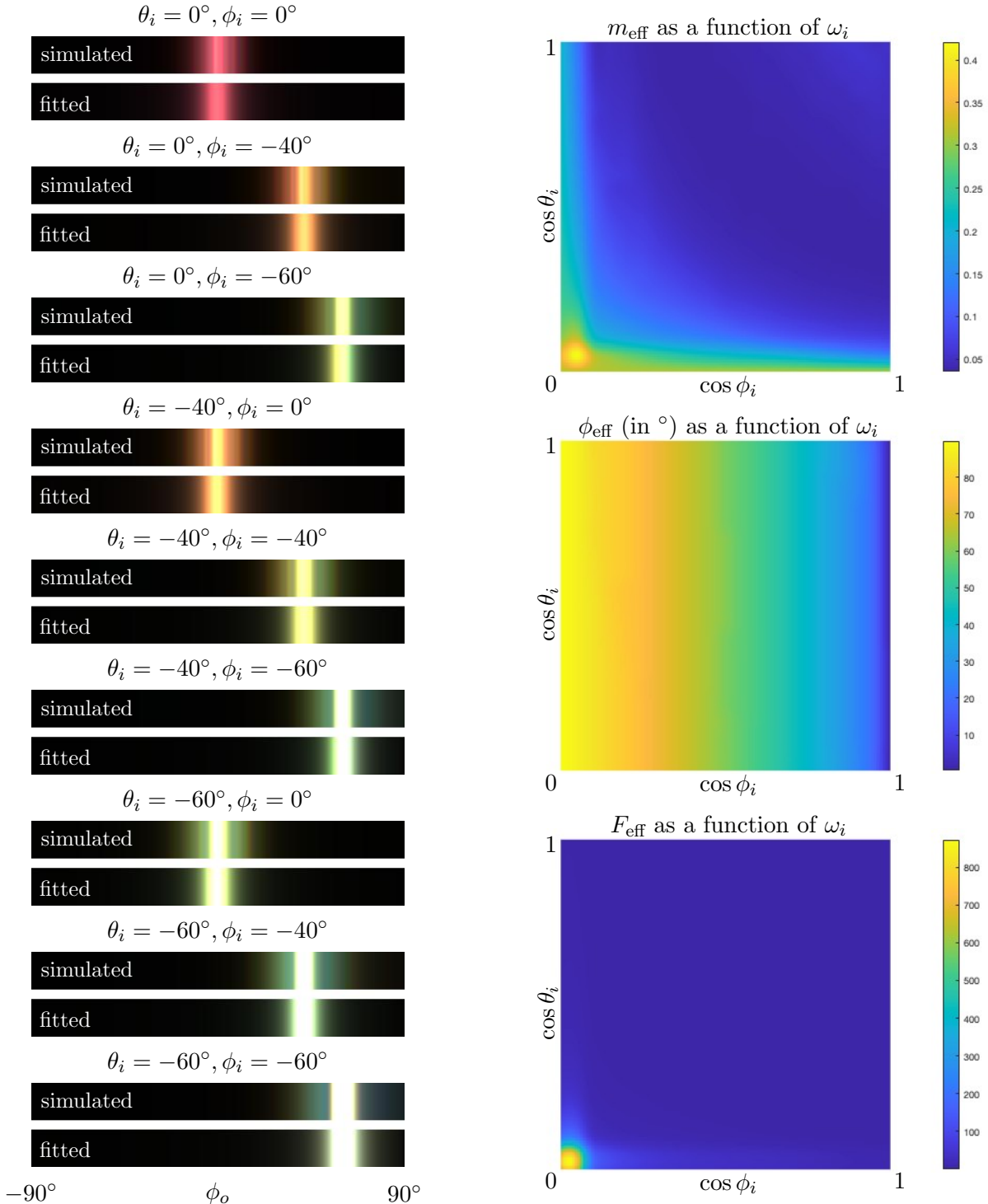


Figure 17: We compare the average reflectance from bronzewing barbules, computed from simulation data, to the analytical average reflectance function fitted to a GGX model. We demonstrate our comparison for a few incident directions, in the specular cone of each incident direction. We also show how the BRDF parameters change with the incident direction, at a fixed wavelength of $\lambda = 400nm$.

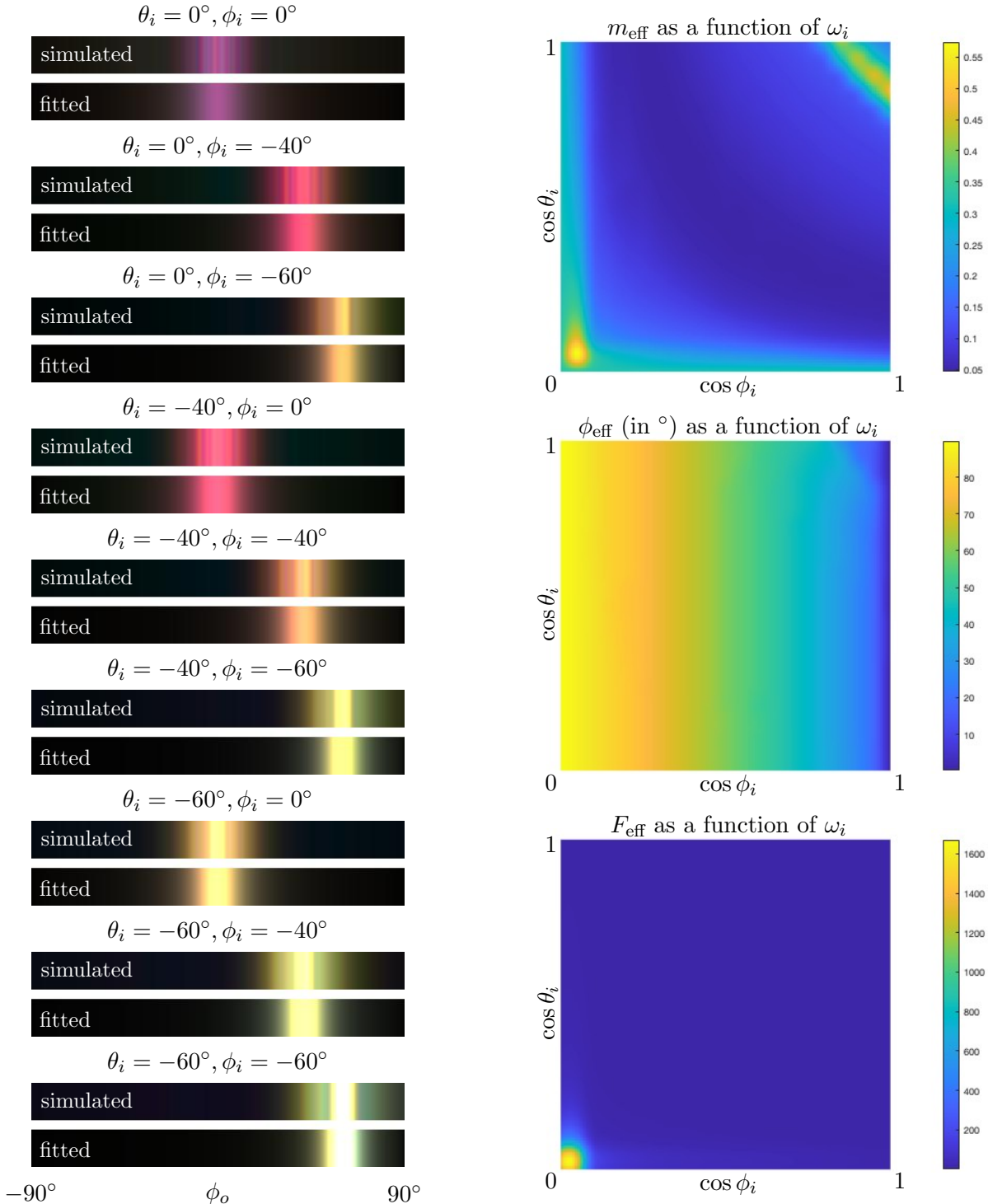


Figure 18: We compare the average reflectance from Anna's hummingbird barbules, computed from simulation data, to the analytical average reflectance function fitted to a GGX model. We demonstrate our comparison for a few incident directions, in the specular cone of each incident direction. We also show how the BRDF parameters change with the incident direction, at a fixed wavelength of $\lambda = 400nm$.

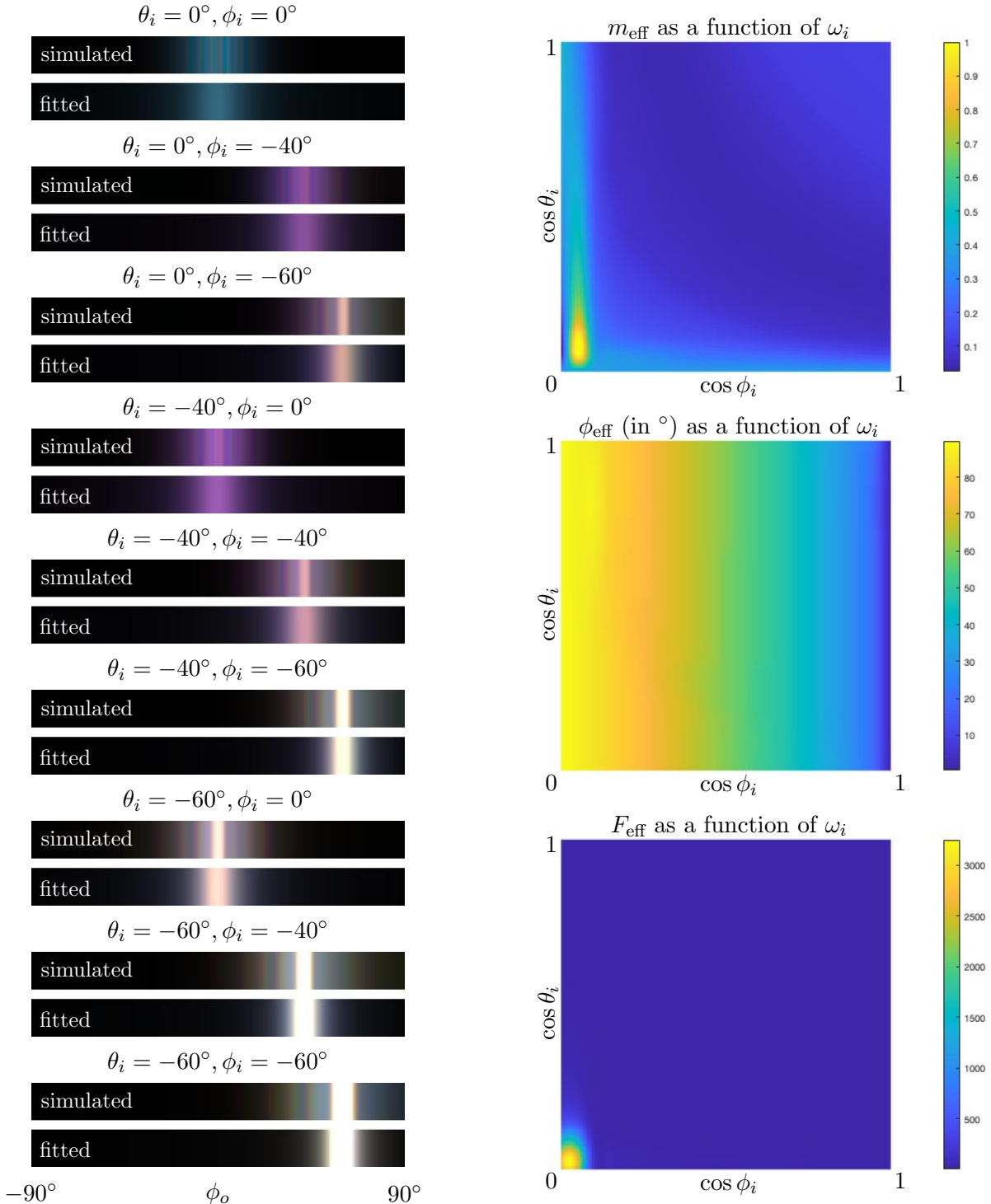


Figure 19: We compare the average reflectance from mallard barbules, computed from simulation data, to the analytical average reflectance function fitted to a GGX model. We demonstrate our comparison for a few incident directions, in the specular cone of each incident direction. We also show how the BRDF parameters change with the incident direction, at a fixed wavelength of $\lambda = 400nm$.

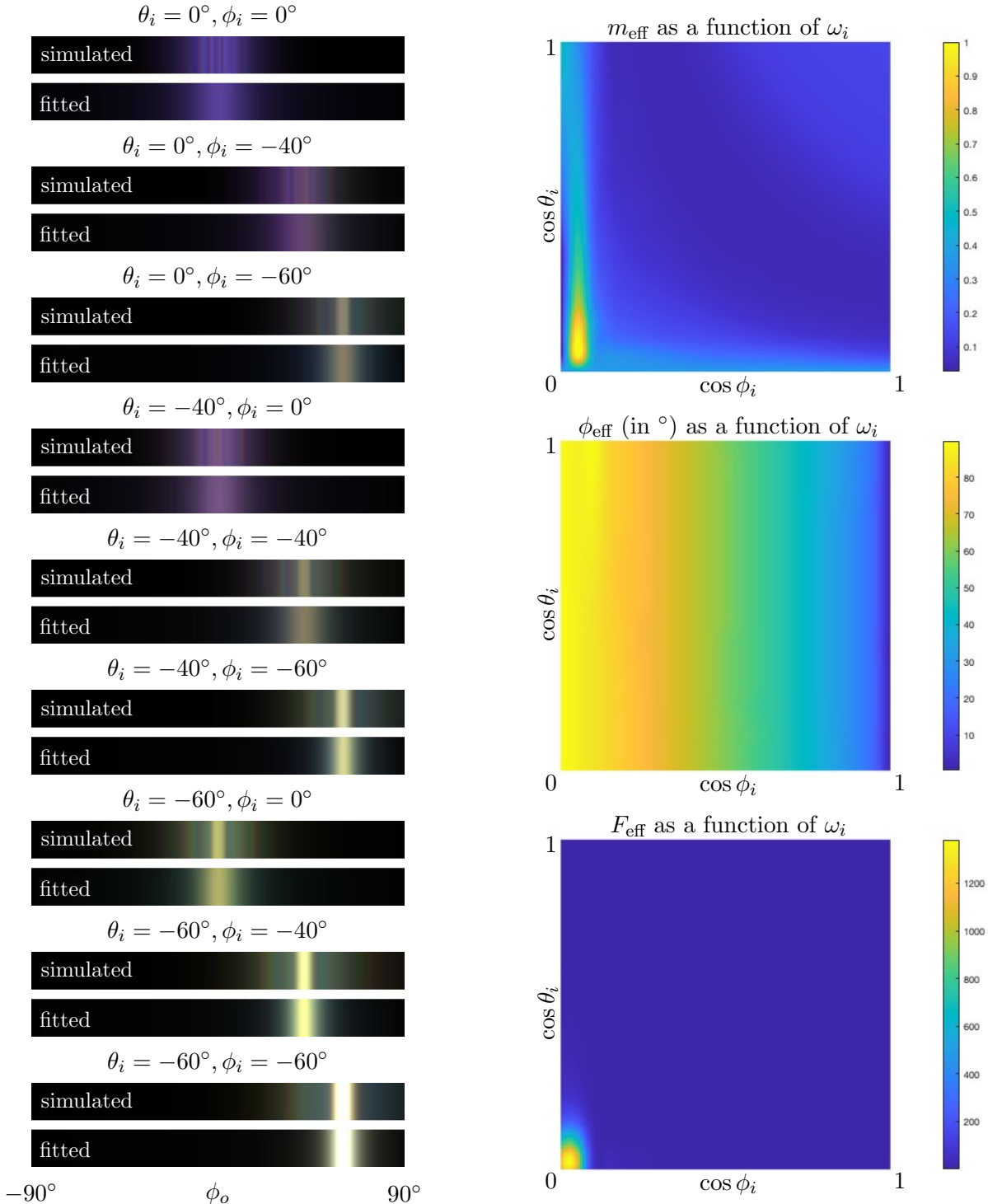


Figure 20: We compare the average reflectance from magpie barbules, computed from simulation data, to the analytical average reflectance function fitted to a GGX model. We demonstrate our comparison for a few incident directions, in the specular cone of each incident direction. We also show how the BRDF parameters change with the incident direction, at a fixed wavelength of $\lambda = 400nm$.

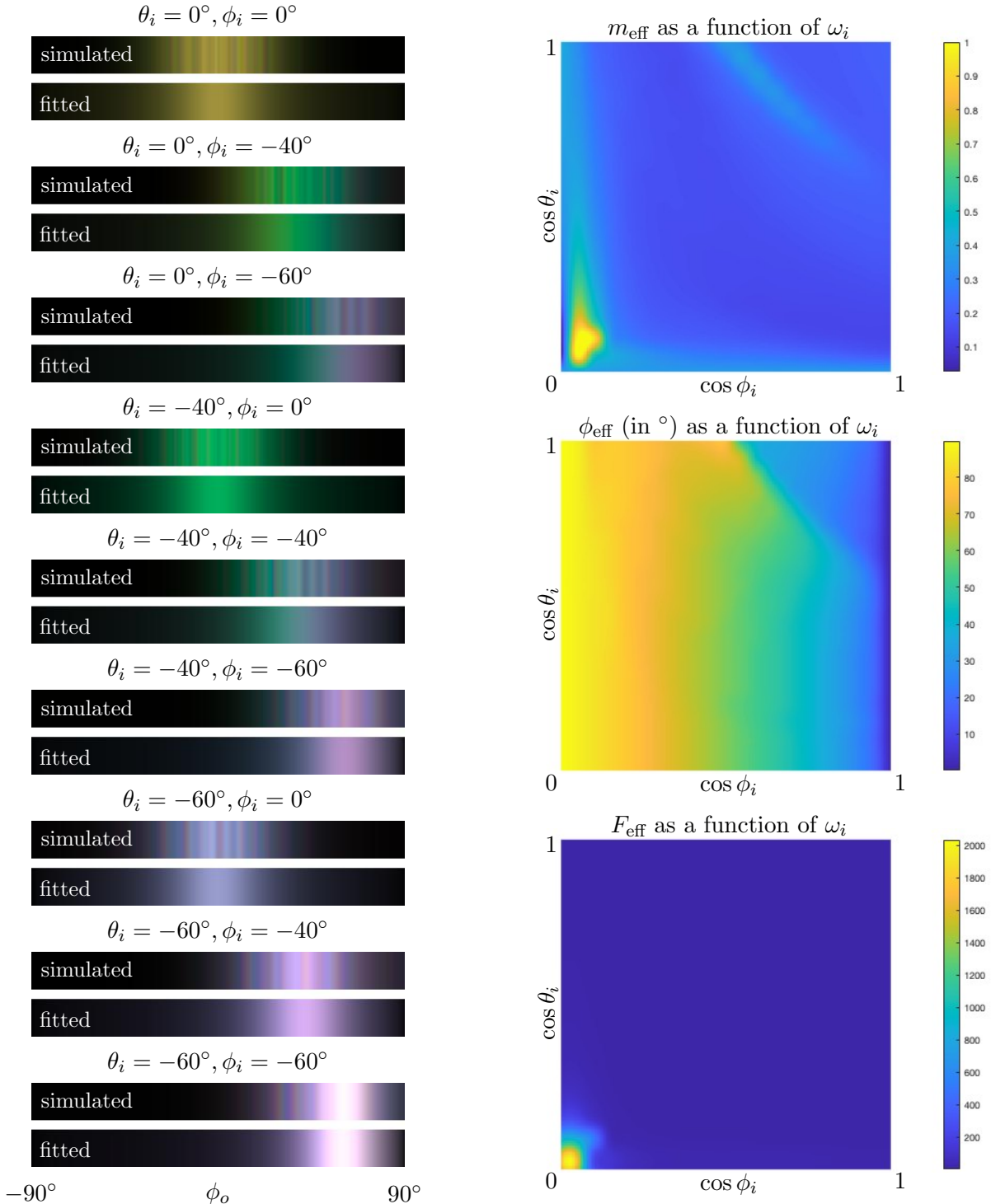


Figure 21: We compare the average reflectance from peacock barbules, computed from simulation data, to the analytical average reflectance function fitted to a GGX model. We demonstrate our comparison for a few incident directions, in the specular cone of each incident direction. We also show how the BRDF parameters change with the incident direction, at a fixed wavelength of $\lambda = 400nm$.

Finally, F_{eff} , which models the total amount of reflectance at each wavelength and incident direction, always has a peak near the exact grazing angle (lower left corner of the maps), since the barbules' reflectance increases as the incident angle approaches 90 degrees. It is not shown in our figures, but F_{eff} tends to be highly wavelength dependent, and modeling this strong dependence of the overall reflectance on the incident light's wavelength is the key to modeling iridescence.

4 Synthesizing BRDF Instances

In Section 5.3 of the main paper, we very briefly introduced our methods for synthesizing a distribution of BRDF instances based on the smooth BRDF \hat{f}_r as well as the statistics computed from wave simulations. We present our full pipeline for constructing BRDF instances in this supplemental document.

4.1 A Distribution of BRDFs

In Section 5.2 of the main paper, we fitted an analytical BDRF \hat{f}_r to model the average reflection from barbules coming from a distribution of slightly different structures. This model could be directly used to render birds from a large distance where no irregularity across a feather is visible, but for closer views this would result in an unrealistically uniform appearance, with all the barbules reflecting in exactly the same way. In fact, we have observed from many sets of simulation results that reflection patterns of individual barbules, which are slightly different from each other, are usually similar in overall form but entirely different in their details. Thus, for rendering we need an efficient model for this variation in individual BRDFs, which preserves the statistical variations in color and brightness that are very important to the overall appearance. We achieve this by synthesizing a distribution of BRDFs based on \hat{f}_r , where the BRDF instances $f_r^{(n)}$ preserve important statistics of the simulated BRDFs.

Because the rapid angular variations seen in barbule BRDFs arise through diffraction from a random geometry, their statistical variation resembles partially developed optical speckle (Goodman, 2007). On this basis, when investigating the scattered fields from a distribution of barbules that are structurally similar, we can assume that each far field scattered field value follows a Gaussian distribution in the complex plane; also, each scattered field value produces a BRDF value as its squared magnitude (Xia et al., 2023; Steinberg and Yan, 2022). A distribution of barbules corresponds to a distribution of BRDFs—the mean of this BRDF distribution is given by \hat{f}_r , and we analyze the variation in terms of single-point and two-point statistics in the angular domain. The single-point statistics, discussed in this section, are the mean and variance of the field scattered to a particular direction; this describes the variation that will be seen in a single still frame. The two-point statistics, discussed in the next section, model the correlations between views of the same barbule from different directions and encode the variations that occur when the camera, object, or light are moving.

Each scattered field vector computed from our 2.5D simulations can be approximated in the form $\vec{\mathcal{E}}_s^{(m)} = E_s^{(m)} \cdot \vec{\mathbf{e}}$, where $\vec{\mathbf{e}}$ is some unit vector and the scalar $E_s^{(m)}$ can be further decomposed into its real and imaginary parts. Thus, we have

$$|\vec{\mathcal{E}}_s^{(m)}(\lambda, \omega_i; \phi_o)|^2 = [R^{(m)}(\lambda, \omega_i; \phi_o)]^2 + [I^{(m)}(\lambda, \omega_i; \phi_o)]^2 \quad (\text{S.16})$$

for each $(\lambda, \omega_i, \phi_o)$. The $R^{(m)}(\lambda, \omega_i; \phi_o)$ and $I^{(m)}(\lambda, \omega_i; \phi_o)$ corresponding to simulated barbule instances

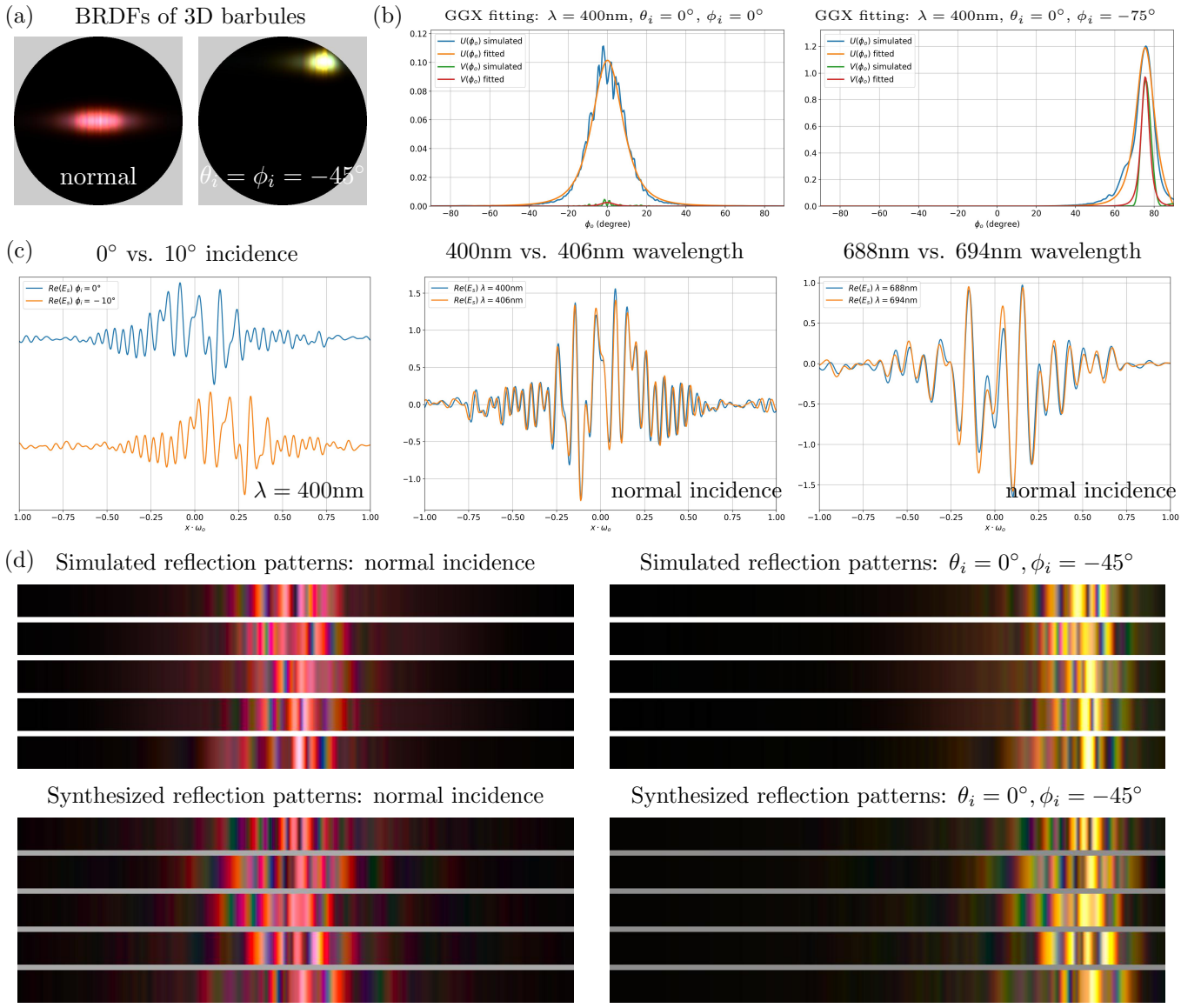


Figure 22: Steps in our BRDF generation pipeline. (a) Some full hemisphere BRDF lobes computed from the 3D version of our wave simulations, performed on 3D barbule segments with explicitly modeled translational symmetry (average of 50 instances). The BRDF lobes are visualized in the projected hemisphere, where we see strong correlations in the BRDF patterns along the y -axis. (b) GGX fitting of the 1D intensity distributions U (see Section 5.2 of the main paper) and V (introduced in Section 4.1 here). The fits are shown for simulation data corresponding to small and large incidence angles. (c) The real parts of the scattered field values from one simulated barbule, i.e. $R^{(m)}(\lambda, \omega_i; \phi_o)$, with respect to the outgoing directions, for a few combinations of (λ, ω_i) . These figures show that a barbule's scattered field pattern "shifts" and "stretches" in response to changes in the incident direction and the simulated wavelength, with the structure of the pattern preserved. (d) Simulated and synthesized BRDF instances, visualized for two incident directions, in their respective specular cones.

should each follow a Gaussian distribution, which we have verified from simulation data on all the simulated barbules.

Importantly, as BRDFs are linearly related to scattered field intensities $|\vec{\mathcal{E}}_s|^2$, we also construct each BRDF value in $f_r^{(n)}$ as the sum of squares of two Gaussian variables, $r^{(n)}$ and $i^{(n)}$, using

$$f_r^{(n)}(\lambda, \omega_i, \omega_o) = [r^{(n)}(\lambda, \omega_i, \omega_o)]^2 + [i^{(n)}(\lambda, \omega_i, \omega_o)]^2 \quad (\text{S.17})$$

where $r^{(n)}, i^{(n)}$ have mean and standard deviation given by μ_r, σ_r, μ_i , and σ_i , which we need to estimate for each $(\lambda, \omega_i, \omega_o)$.

To start with, the synthesized BRDFs need to average to \hat{f}_r , i.e

$$E[f_r^{(n)}(\lambda, \omega_i, \omega_o)] = \hat{f}_r(\lambda, \omega_i, \omega_o) \quad (\text{S.18})$$

Thus, combining Eq. S.17 and Eq. S.18 gives us one constraint on the single-point statistics

$$\hat{f}_r = \mu_r^2 + \sigma_r^2 + \mu_i^2 + \sigma_i^2 \quad (\text{S.19})$$

at each $(\lambda, \omega_i, \omega_o)$. To further constrain these quantities, we also want to estimate $(\mu_r^2 + \mu_i^2)/\hat{f}_r$. Therefore, we define the mean scattered field values as

$$\bar{R}(\lambda, \omega_i; \phi_o) = \frac{1}{M} \sum_{m=1}^M R^{(m)}(\lambda, \omega_i; \phi_o) \quad (\text{S.20})$$

where $R^{(m)}$ comes from Eq. S.16, along with a similarly defined quantity \bar{I} . Related to the mean scattering distribution U defined in Eq. S.12, we define another distribution V as

$$V(\lambda, \omega_i; \phi_o) = c_0 \frac{[\bar{R}(\lambda, \omega_i; \phi_o)]^2 + [\bar{I}(\lambda, \omega_i; \phi_o)]^2}{\Phi_i(\lambda, \omega_i)} \quad (\text{S.21})$$

Thus V represents the portion in U “contributed” by the squared mean field values, and so $U - V$ represents the contribution from the fields’ variation about their mean values. To estimate the single-point statistics μ_r, σ_r, μ_i , and σ_i for all pairs of directions, we first need to extend the 1D distribution V into the full hemisphere. Therefore, we perform GGX fitting of V in ω_i ’s specular cone and obtain another roughness parameter $m_{\text{sta}}(\lambda, \omega_i)$ and effective incident direction parameter $\phi_{\text{sta}}(\lambda, \omega_i)$, in the same way as we fit U . From m_{sta} and ϕ_{sta} , we construct a statistics function s , such that

$$s(\lambda, \omega_i, \omega_o) = F_{\text{sta}} \frac{D(m_{\text{sta}}, \sigma; \omega_h) G(m_{\text{sta}}; \omega_{\text{sta}}, \omega_o)}{4(\hat{\mathbf{z}} \cdot \omega_{\text{sta}})(\hat{\mathbf{z}} \cdot \omega_o)} \quad (\text{S.22})$$

where we choose the same σ value as for \hat{f}_r . F_{sta} , formally written as $F_{\text{sta}}(\lambda, \omega_i)$, plays a similar role as F_{eff} , guaranteeing

$$\int_{H^2} s(\lambda, \omega_i, \omega_o) \cdot (\hat{\mathbf{z}} \cdot \omega_o) d\omega_o = \cos \theta_i \int_{-\pi/2}^{\pi/2} V(\lambda, \omega_i; \phi_o) d\phi_o \quad (\text{S.23})$$

Our GGX fittings of U and V are illustrated in Fig. 22(b). With small incident angles, V tends to be very small compared to U , and the ratio V/U increases with the incident angle, while always satisfying

$V \leq U$, as guaranteed by the underlying Gaussian distributions. As a result, the functions \hat{f}_r and s also satisfy $s \leq \hat{f}_r$ for most $(\lambda, \omega_i, \omega_o)$. At very large incident angles ($< 3^\circ$ from grazing), errors in our GGX fitting result in $s > \hat{f}_r$ at some points, and in these cases we simply set $s = \hat{f}_r$. Given \hat{f}_r and s , for each $(\lambda, \omega_i, \omega_o)$ we assign

$$\mu_r = \sqrt{s}; \quad \mu_i = 0; \quad \sigma_r = \sigma_i = \sqrt{\hat{f}_r - s} \quad (\text{S.24})$$

assuming the real and imaginary parts of scattered field values have the same standard deviation, as predicted by speckle theory and verified empirically for our data. We find that the specific values of μ_r, μ_i do not affect the overall properties of the synthesized BRDFs, as long as they satisfy $\mu_r^2 + \mu_i^2 = s$.

4.2 BRDF Noise Functions

In Eq. S.17, we introduced our scheme for constructing each BRDF value as the sum of squares of two Gaussian variables, but simply using Eq. S.17 to generate one after another BRDF value implies that all the involved Gaussian variables will be independent. This way, these synthesized BRDFs would carry no information about how the reflectance changes when the viewing configuration or wavelength changes. In fact, a synthesized BRDF $f_r^{(n)}$ should be a continuous function of λ, ω_i , and ω_o .

Specifically, we want our synthesized BRDFs to mimic the field variations found in $R^{(m)}(\lambda, \omega_i; \phi_o)$ and $I^{(m)}(\lambda, \omega_i; \phi_o)$. The form of the functions $R^{(m)}(\lambda, \omega_i; \phi_o)$ and $I^{(m)}(\lambda, \omega_i; \phi_o)$ depends on $\lambda, \theta_i, \phi_i$, and ϕ_o , but a few observations about the simulation results allow for some simplifications. Importantly, in keeping with the behavior of optical speckle, the BRDFs predicted by our simulations locally act like functions of the sum of $x_i = \hat{\mathbf{x}} \cdot \omega_i$ and $x_o = \hat{\mathbf{x}} \cdot \omega_o$. This can be seen in the leftmost picture in Figure 22(c), where the scattered field shifts in response to a change in ϕ_i . Also, the change in the scattered field in response to a change of λ is approximately a scaling along the \mathbf{x} direction, as seen in the middle and rightmost pictures in Figure 22(c).

Assuming that a synthesized BRDF instance $f_r^{(n)}$ follows these behaviors exactly, while conforming to the Gaussian variable representation in Eq. S.17, we arrive at the following model:

$$f_r^{(n)}(\lambda, \omega_i, \omega_o) = [\sigma_r(\lambda, \omega_i, \omega_o) \cdot q_r^{(n)}(x) + \mu_r(\lambda, \omega_i, \omega_o)]^2 + [\sigma_i(\lambda, \omega_i, \omega_o) \cdot q_i^{(n)}(x) + \mu_i(\lambda, \omega_i, \omega_o)]^2 \quad (\text{S.25})$$

where $\mu_r, \sigma_r, \mu_i, \sigma_i$ are the single-point statistics defined in Eq. S.24, and the functions $q_r^{(n)}$ and $q_i^{(n)}$ are instances of a one-dimensional noise process. The quantity $x = x(\lambda, \omega_i, \omega_o)$ is given by

$$x(\lambda, \omega_i, \omega_o) = \frac{\hat{\mathbf{x}} \cdot \omega_i + \hat{\mathbf{x}} \cdot \omega_o}{l(\lambda, \omega_i)} \quad (\text{S.26})$$

where $l(\lambda, \omega_i)$ is a scale factor that modulates the autocorrelation in $f_r^{(n)}(\lambda, \omega_i, \omega_o)$ with respect to the outgoing direction. In our tests we have found this autocorrelation needs to vary with both wavelength and incident direction. With this model, it remains to define the length function l , as well as the 1D process that generates the noise functions $q_{r,i}$. Notably, we only need two instances of this noise process to generate a pair of $q_r^{(n)}, q_i^{(n)}$, to define an entire synthesized BRDF for a single barbule.

Together the length function l and the 1D noise process model the variation patterns, or oscillation patterns, in the scattered fields from single barbules. As illustrated in Fig. 22(c) these field variations depend on the incident parameters (λ, ω_i) —e.g. the field values oscillate faster at smaller wavelengths, as shown in the middle and rightmost plots. To summarize the field variation patterns, for each λ and ω_i we treat $R^{(m)}(\lambda, \omega_i; \phi_o)$ as a 1D function of x_o —the x -component of the outgoing direction (recall that R is defined in the specular cone so x_o relates to θ_i and ϕ_o). Within each $R^{(m)}$, we compute the covariance between $R^{(m)}(\lambda, \omega_i; x_o)$ and $R^{(m)}(\lambda, \omega_i; x_o + \Delta_x)$ for each offset Δ_x , while using a weighting function to emphasize regions where $|R^{(m)}|^2$ is large. This gives us an autocovariance (ACV) function corresponding to $R^{(m)}(\lambda, \omega_i; \phi_o)$, and then we average the ACVs for all barbule instances m , obtaining a single ACV parameterized by λ and ω_i . The same process works for $I^{(m)}$ and gives rise to a nearly identical ACV at each (λ, ω_i) , and so in practice we average the ACVs from the real and imaginary field values, arriving at a single ACV function per barbule type, denoted as $C(\lambda, \omega_i; \Delta_x)$. The steps to compute $C(\lambda, \omega_i; \Delta_x)$ will be discussed thoroughly in Section 4.3.

The ACVs defined for each (λ, ω_i) then allow us to define the process for generating $q_{r,i}$ and also compute the length function $l(\lambda, \omega_i)$. We use the ACV for normal incidence and the shortest wavelength, defined as $C_0(\Delta_x) = C(400\text{nm}, \hat{\mathbf{z}}; \Delta_x)$, and a 1D Gaussian process to generate $q_{r,i}$, such that these noise functions have their average ACV given by C_0 . Moreover, the noise functions satisfy

$$E[q_{r,i}^{(n)}(x)] = 0; \quad \text{Var}[q_{r,i}^{(n)}(x)] = 1 \quad (\text{S.27})$$

at any point x , a property required by the model in Eq. S.25, to preserve single-point statistics for each point in the synthesized BRDF. We discuss our 1D Gaussian process in detail in Section 4.4.

The length function $l(\lambda, \omega_i)$ is computed by fitting $C(\lambda, \omega_i; \cdot)$ with a scaled copy of C_0 , i.e.

$$C(\lambda, \omega_i; \Delta_x) \approx C_0\left(\frac{\Delta_x}{l(\lambda, \omega_i)}\right) \quad (\text{S.28})$$

implying that $l = 1$ at 400nm and normal incidence. In general, a larger value of l indicates slower oscillation in the scattered field values as a function of the outgoing direction, as is the case for longer wavelengths. The function $l(\lambda, \omega_i)$ is another important model parameter in our BRDF, associated with evaluating each synthesized BRDF instance. Up until this point, all the introduced BRDF parameters— m_{eff} , ϕ_{eff} , F_{eff} , m_{sta} , ϕ_{sta} , F_{sta} , and l —along with our 1D noise generation process, fully define our iridescent feather appearance model.

4.3 Estimating ACVs from Scattered Field Patterns

We now present our steps to compute the “master” ACV function $C(\lambda, \omega_i; \Delta_x)$, defined in Section 4.2.

We first recall $R^{(m)}(\lambda, \omega_i; \phi_o)$ and $I^{(m)}(\lambda, \omega_i; \phi_o)$, defined in Eq. S.16. By symmetry, R and I have identical statistical properties, so we proceed with our discussions with respect to $R^{(m)}(\lambda, \omega_i; \phi_o)$. For each simulated wavelength λ and incident direction ω_i , $R^{(m)}(\lambda, \omega_i; \phi_o)$, coming from our simulation data, is defined in the specular cone relative to ω_i , and is a 1D function of ϕ_o . Alternatively, we can also see R as a function of $x_o = \hat{\mathbf{x}} \cdot \omega_o$, where ω_o is an outgoing direction in the specular cone, corresponding to the azimuthal angle ϕ_o . As in Fig. 22(c), we plot R with respect to x_o at $\lambda = 400\text{nm}$ and normal incidence in Fig. 23, for one barbule instance.

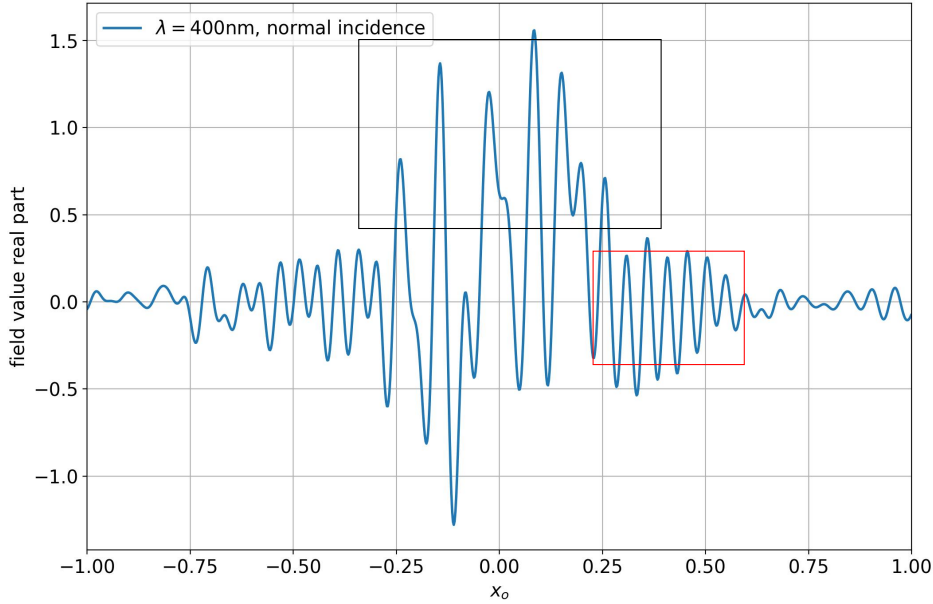


Figure 23: Real part of the scattered field from a barbule, simulated under normal incidence with $\lambda = 400nm$. The scattered field is plotted as a function of the x -component of the outgoing direction. The oscillation frequencies of the field are different in different regions.

As indicated with the black and red boxes, the oscillation in R looks different at different regions. The black box indicates a region where $|R^{(m)}(\lambda, \omega_i; \phi_o)|^2$ is large, and here, the field oscillation seems to be slower and a bit irregular. The red box indicates a region where $|R^{(m)}(\lambda, \omega_i; \phi_o)|^2$ is small, and at this region the field oscillates faster with the outgoing direction, and the oscillation pattern seems more regular. When we summarize the autocovariance in $R^{(m)}(\lambda, \omega_i; \phi_o)$, we want to reinforce the region where $|R^{(m)}(\lambda, \omega_i; \phi_o)|^2$ is large—usually around the specular reflection direction, where the BRDF values are large. Thus, instead of directly computing the ACV function of $R^{(m)}(\lambda, \omega_i; \phi_o)$, we first define another function $r^{(m)}(\lambda, \omega_i; \phi_o)$, i.e.

$$r^{(m)}(\lambda, \omega_i; \phi_o) = \sqrt{U'(\lambda, \omega_i; \phi_o)} \cdot R^{(m)}(\lambda, \omega_i; \phi_o) \quad (\text{S.29})$$

where $U'(\lambda, \omega_i; \phi_o)$ is the GGX fitted version of $U(\lambda, \omega_i; \phi_o)$ (recall Eq. S.12). As an illustration, we plot r with respect to x_o in Fig. 24, for the same barbule instance used in Fig. 23.

Note that our construction of $r^{(m)}(\lambda, \omega_i; \phi_o)$ is fairly empirical—we simply want to weight $R^{(m)}(\lambda, \omega_i; \phi_o)$ in such a way that reinforces directions where $|R^{(m)}(\lambda, \omega_i; \phi_o)|^2$ is large, and there can be many other ways to achieve this. Here, since the mean field intensity U is associated with the squared field values, the amplitude of $r^{(m)}(\lambda, \omega_i; \phi_o)$ at each point is roughly associated with $|R^{(m)}(\lambda, \omega_i; \phi_o)|^2$.

Our next step is to compute an ACV function using $r^{(m)}(\lambda, \omega_i; \phi_o)$. From this point, we note that the function $r^{(m)}(\lambda, \omega_i; \phi_o)$ is discrete, as we can only compute scattered field values at a finite collection of outgoing directions. For convenience, we rewrite $r^{(m)}(\lambda, \omega_i; \phi_o)$ as $r_m(\lambda, \omega_i; x_j)$, suggesting that it is defined at a finite set of N points, x_0, x_1, \dots, x_{N-1} , where each x_j is the x -component of some outgoing direction in ω_i 's specular cone.

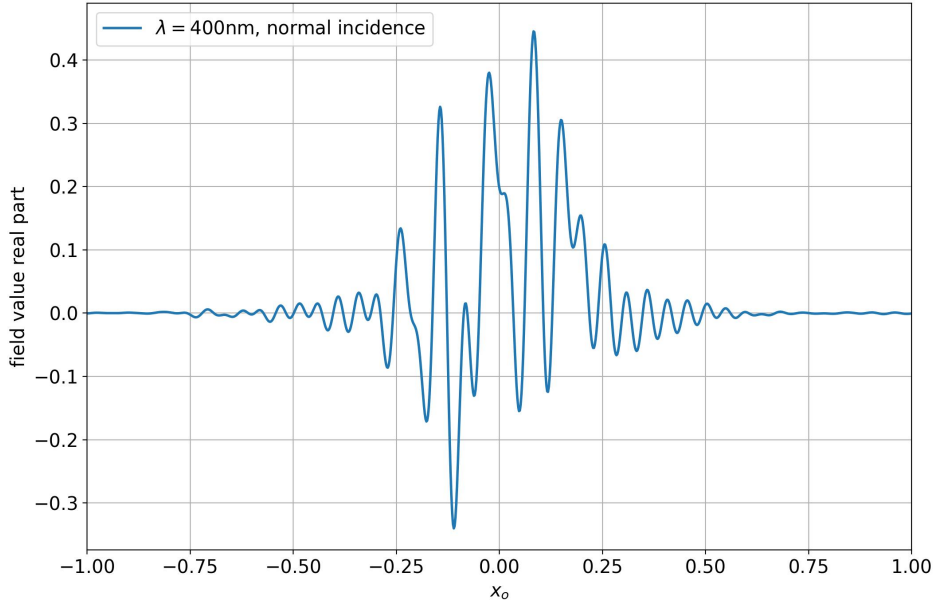


Figure 24: Illustration of the function $r^{(m)}(\lambda, \omega_i; \phi_o)$, computed from enveloping the function $R^{(m)}(\lambda, \omega_i; \phi_o)$ with a window that reinforces directions where $|R^{(m)}(\lambda, \omega_i; \phi_o)|^2$ is large.

The ACV function corresponding to $r_m(\lambda, \omega_i; x_j)$ is therefore also discrete, and we denote it as $C_m(\lambda, \omega_i; \Delta_k)$. Here, k is some integer and we have $\Delta_k = k \cdot \Delta$, where $\Delta = x_1 - x_0$, assuming the $\{x_j\}$ series is uniformly spaced. The ACV function is computed as

$$C_m(\lambda, \omega_i; \Delta_k) = \frac{1}{N-1} \sum_{j=0}^{N-1} [r_m(\lambda, \omega_i; x_j) - \bar{r}_m][r_m(\lambda, \omega_i; x_{j+k}) - \bar{r}_m] \quad (\text{S.30})$$

where $\bar{r}_m = \frac{1}{N} \sum_{j=0}^{N-1} r_m(\lambda, \omega_i; x_j)$

In practice, we usually compute $C_m(\lambda, \omega_i; \Delta_k)$ for $k = -N/2, -N/2 + 1, \dots, -1, 0, 1, \dots, N/2 - 1$. In cases where $j + k < 0$ or $j + k > N - 1$, we set the function value of r_m to 0—because these cases correspond to scattering into (undefined) directions outside of the upper hemisphere. Note that Eq. S.29 implies that $r^{(m)}(\lambda, \omega_i; \phi_o)$ tends to 0 when the outgoing direction approaches grazing ($|\phi_o| = 90^\circ$), because of the shadowing-masking term built into $U'(\lambda, \omega_i; \phi_o)$.

The ACV function is symmetrical, in that we have $C_m(\lambda, \omega_i; \Delta_k) = C_m(\lambda, \omega_i; \Delta_{-k})$. The aforementioned computation can be repeated for $R^{(m)}$, and also $I^{(m)}$, corresponding to all the simulated barbule instances m , giving rise to many individual ACVs, and we compute an average ACV from the individual ones, and denote it as $C(\lambda, \omega_i; \Delta_k)$. As some examples, we plot $C_m(\lambda, \omega_i; \Delta_k)$ for a few barbule instances in Fig. 25(a)–(c), for $\lambda = 400nm$ and normal incidence, and plot the corresponding average ACV (normalized to unit variance) in 25(d). Thanks to symmetry, we only need to plot one side of the ACV functions, and even though these ACV function values are discrete, they can be considered discrete samples from continuous ACV functions. The Δ_x labeling on the x -axes in our plots refers to the offset between the

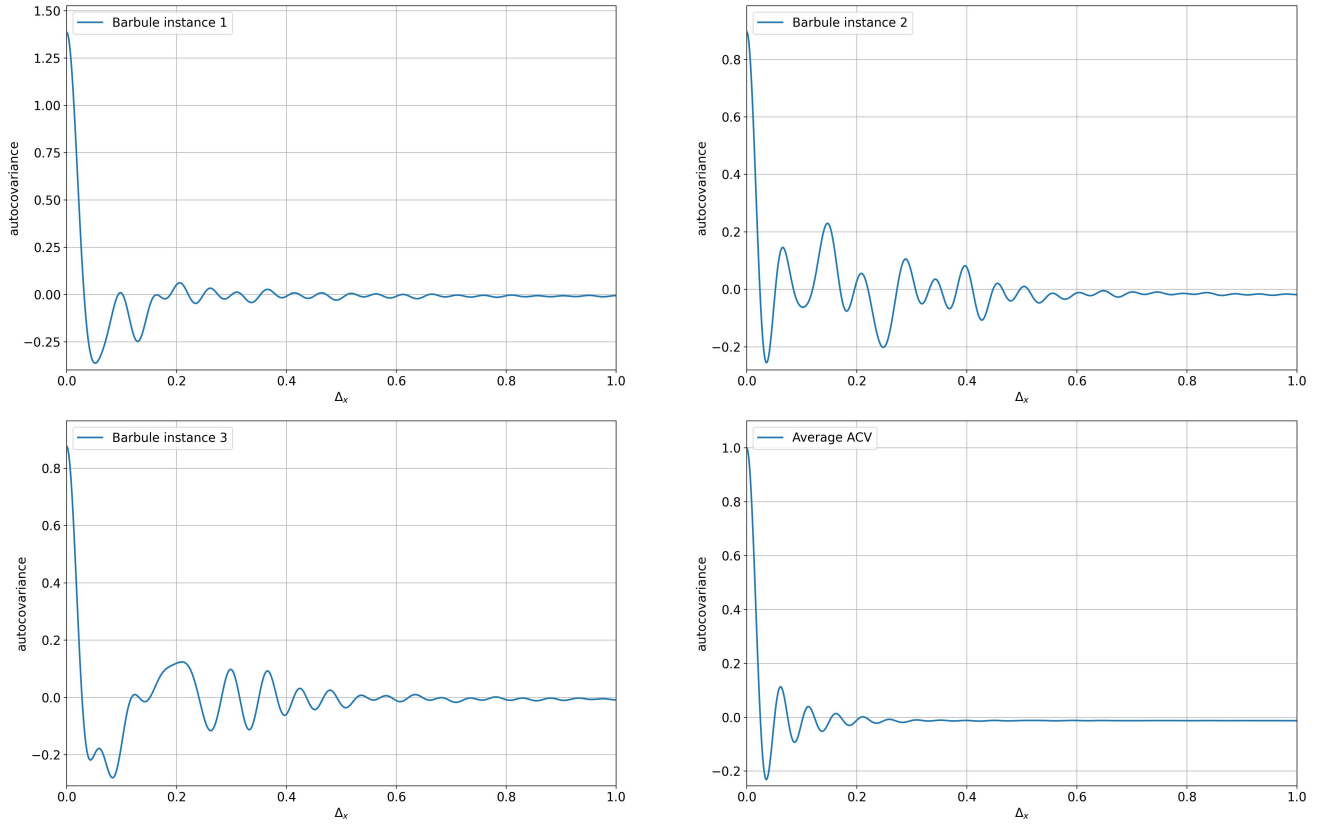


Figure 25: ACV functions of scattered field values from some individual barbule instances, as compared to the smoother, average ACV across all the barbule instances (100 instances). These ACVs correspond to $\lambda = 400\text{nm}$ and normal incidence.

x -components of two (normalized) outgoing directions.

The function $C(\lambda, \omega_i; \Delta_k)$ therefore summarizes the variation patterns (e.g. oscillation frequencies) in the barbules' scattered fields, corresponding to wavelength λ and incident direction ω_i . We compute $C(\lambda, \omega_i; \Delta_k)$ for all our simulated wavelengths and incident directions. As mentioned in Section 4.2, the ACV at $\lambda = 400\text{nm}$ and normal incidence, which we also denote as $C_0(\Delta_k)$, is used for noise function generation. Moreover, ACVs corresponding to other wavelengths or incident directions are used to derive the BRDF parameter $l(\lambda, \omega_i)$, as also described in Section 4.2.

Here, we illustrate the parameter $l(\lambda, \omega_i)$ with an example, shown in Fig. 26. In this example, the average ACV at 694nm , normal incidence is compared to the average ACV at 400nm , normal incidence. When Δ_x is small, the ACV at the longer wavelength decreases more slowly with Δ_x , indicating that it has a longer autocorrelation length. This is because the scattered fields oscillate more slowly with the outgoing direction for the longer wavelength. Importantly, our ACV C_0 (400nm , normal) can be scaled along the x -axis to approximately match the ACV at 694nm , as shown in the figure, where the orange and green

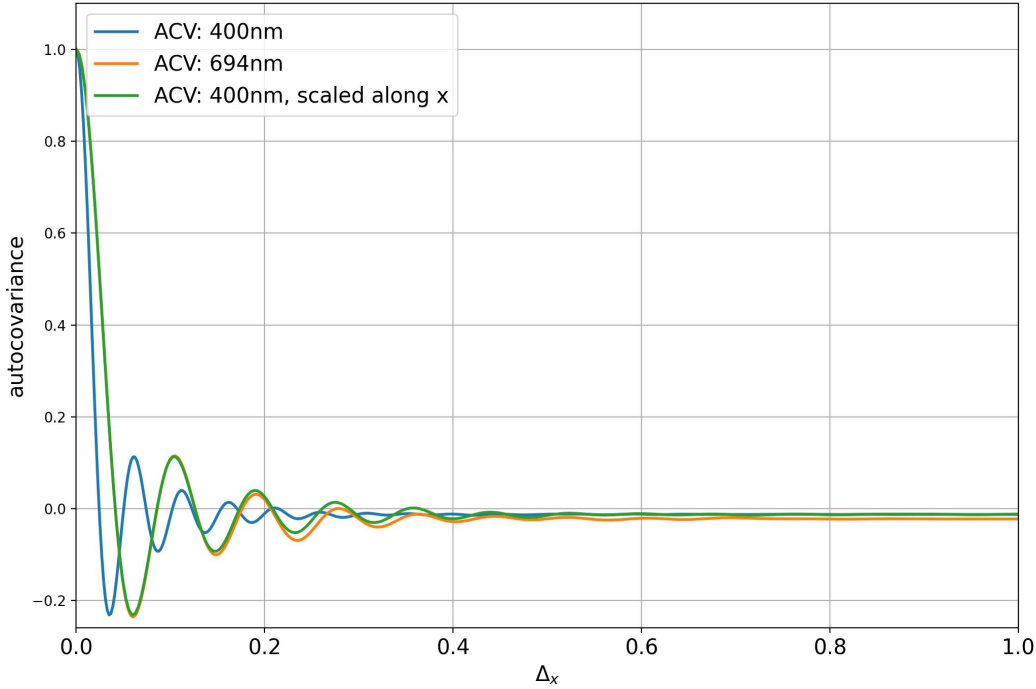


Figure 26: Some illustration of how to compute the BRDF parameter $l(\lambda, \omega_i)$ from the main paper.

curves almost overlap. Mathematically, we have

$$C(694nm, \hat{\mathbf{z}}; \Delta_x) \approx C_0\left(\frac{\Delta_x}{1.6966}\right) \quad (\text{S.31})$$

giving rise to the parameter value $l(694nm, \hat{\mathbf{z}}) = 1.6966$. In the formulation above, the ACV functions are treated as continuous, with their discrete function values understood as discretely sampled from an underlying continuous function. We therefore used Δ_x (where x represents the x -component of a normalized outgoing direction), rather than Δ_k (where k is an integer) in the formulation. Still, the ACVs are computed and stored as discrete function values.

4.4 1D Gaussian Process for Noise Generation

We now expand on the 1D Gaussian process mentioned in Section 4.2. When building BRDF for each type of feather, this Gaussian process takes an ACV function $C_0(\Delta_k)$ as input, and generate 1D noise functions $q(x)$ with matching ACVs (on average). $C_0(\Delta_k)$ was discussed in Section 4.3.

The function values in $C_0(\Delta_k)$ are discrete, and therefore the generated noise functions $q(x)$ are also discretely represented. Specifically, we construct an noise function q by defining its function values at N points, denoted as q_0, q_1, \dots, q_{N-1} .

The discrete function values in q are generated using a process based on the Wiener-Khinchin theorem, and each function value q_k is a Gaussian variable, such that

$$E(q_k) = 0; \quad \text{Var}(q_k) = 1 \quad (\text{S.32})$$

For this reason, we call our noise function generation process a Gaussian process.

The first step in our noise generation is to compute the discrete power spectral density function corresponding to C_0 . We use a discrete Fourier transform (DFT) for this step. We denote the PSD function as P , and use P_l to denote its discrete function values. For convenience, we also use C_k as a short name for $C_0(\Delta_k)$ (recall $\Delta_k = k \cdot \Delta$ for some unit offset Δ). C_0 and P form a Fourier transform pair

$$\begin{aligned} P_l &= \frac{1}{N} \sum_{k=0}^{N-1} C_k \cdot e^{-2\pi i k l / N} \\ C_k &= \sum_{l=0}^{N-1} P_l \cdot e^{2\pi i k l / N} \end{aligned} \quad (\text{S.33})$$

Here, when $k \leq N/2 - 1$, we have $C_k = C_0(\Delta_k)$, while when $k \geq N/2$, we set C_k to equal $C_0(\Delta_{k-N})$, evaluating the ACV function at negative offsets—this is just for convenience, such that we do not need to work with negative indices. There also seems to be a periodic assumption underlying the DFT setup, which makes no physical sense. In fact, we detach any physical meaning from our noise generation process for now and merely understand it as a pipeline for generating noise functions with desired statistics. At the end of this section, we bring back the physical meaning underlying the noise functions and discuss their usage in BRDF synthesis.

By its nature, our ACV should roughly satisfy $\sum_{k=0}^{N-1} C_k = 0$, up to some very small error. In practice, we add a tiny constant ε to all the $\{C_k\}$ values such that $\sum_{k=0}^{N-1} C_k = 0$, and further normalize the function such that $C_0 = 1$. These steps should leave the overall form and properties of the ACV function unchanged. From Eq. S.33, we now have

$$\sum_{l=0}^{N-1} P_l = C_0 = 1 \quad \text{and} \quad P_0 = \frac{1}{N} \sum_{k=0}^{N-1} C_k = 0 \quad (\text{S.34})$$

For illustration purposes, we plot a pair of discrete ACV and PSD functions in Fig. 27. The functions look symmetrical thanks to the symmetry in the ACV function, and we have permuted the function so that our indices are all positive $(0, 1, \dots, N - 1)$.

Given P , we can now generate noise functions from a random process. For generating each noise function q , we first generate a spatial frequency spectrum s based on P :

$$s_l = \begin{cases} \sqrt{P_0} = 0 & \text{for } l = 0 \\ \sqrt{P_l} \cdot (a_l + b_l i) & \text{for } 1 \leq l \leq \frac{N}{2} - 1 \\ \sqrt{P_{N/2}} \approx 0 & \text{for } l = \frac{N}{2} \\ \sqrt{P_{l'}} \cdot (a_{l'} - b_{l'} i), \text{ where } l' = N - l & \text{for } \frac{N}{2} + 1 \leq l \leq N - 1 \end{cases} \quad (\text{S.35})$$

where for $l = 1, 2, \dots, N/2 - 1$, a_l, b_l are random variables drawn from the normal distribution $N(0, \sqrt{0.5})$. Note that from the symmetries in the ACV and PSD functions, we have $P_{l'} = P_l$ if $l' = N - l$. Given s , a noise function q is defined as

$$q_k = \sum_{l=0}^{N-1} s_l \cdot e^{2\pi i k l / N} \quad (\text{S.36})$$

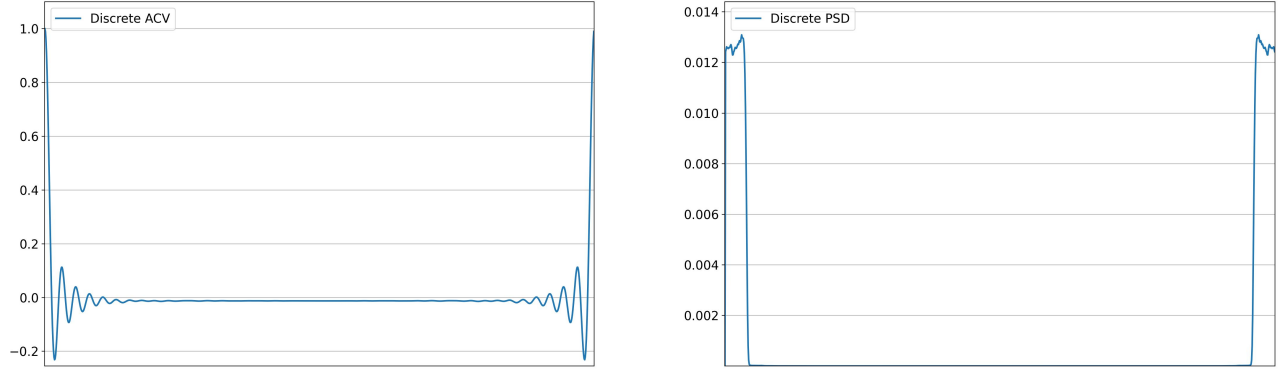


Figure 27: Discrete ACV and PSD functions used for noise generation.

Importantly, Eq. S.35 guarantees that q is real-valued.

We now verify the properties of q , described in Eq. S.32. First of all, Eq. S.36 reveals that each value q_k is fundamentally a linear combination of lots of Gaussian variables a_l, b_l , which makes q_k a Gaussian variable itself. To compute the mean and variance of q_k , we first combine Eq. S.35 and Eq. S.36 to derive

$$\begin{aligned} q_k &= \sum_{l=1}^{N/2-1} \sqrt{P_l} \cdot [(a_l + b_l i) e^{2\pi i k l / N} + (a_l - b_l i) e^{-2\pi i k l / N}] \\ &= \sum_{l=1}^{N/2-1} \sqrt{P_l} \cdot [(a_l + b_l i)(c_l + d_l i) + (a_l - b_l i)(c_l - d_l i)] \quad c_l^2 + d_l^2 = 1 \\ &= \sum_{l=1}^{N/2-1} \sqrt{P_l} \cdot (2c_l a_l - 2d_l b_l) \end{aligned} \quad (\text{S.37})$$

Thus, we can easily verify that

$$E(q_k) = \sum_{l=1}^{N/2-1} \sqrt{P_l} \cdot [2c_l \cdot E(a_l) - 2d_l \cdot E(b_l)] = 0 \quad (\text{S.38})$$

as $a_l, b_l \sim N(0, \sqrt{0.5})$, and

$$\begin{aligned} \text{Var}(q_k) &= \sum_{l=1}^{N/2-1} P_l \cdot [4c_l^2 \text{Var}(a_l) + 4d_l^2 \text{Var}(b_l)] \\ &= \sum_{l=1}^{N/2-1} P_l \cdot (4c_l^2 \cdot 0.5 + 4d_l^2 \cdot 0.5) \\ &= 2 \sum_{l=1}^{N/2-1} P_l \\ &= 1 \quad (\text{by symmetry of the PSD}) \end{aligned} \quad (\text{S.39})$$

We next show that the (discrete) autocovariance functions of the generated noise functions q average to C_0 , the ACV function we started off with. Denoting the individual PSD function corresponding to the generated noise function q as P' , from Eq. S.35 and Eq. S.36, we know that

$$P'_l = P_l \cdot (a_l^2 + b_l^2) \quad (\text{or replace with } a_{l'}^2 + b_{l'}^2 \text{ if } l > \frac{N}{2}) \quad (\text{S.40})$$

We therefore have

$$E[P'_l] = P_l \cdot E(a_l^2 + b_l^2) \quad (\text{S.41})$$

Since $a_l, b_l \sim N(0, \sqrt{0.5})$, the sum of squares $a_l^2 + b_l^2$ follows an exponential distribution:

$$p(a_l^2 + b_l^2) = \frac{1}{2\sigma_0^2} e^{-\frac{a_l^2+b_l^2}{2\sigma_0^2}} \quad (\text{S.42})$$

indicating $E(a_l^2 + b_l^2) = 2\sigma_0^2 = 1$, since $\sigma_0 = \sqrt{0.5}$. This way, we have:

$$E[P'_l] = P_l \quad (\text{S.43})$$

Since the noise functions q have the correct expected PSD function, they also have the correct expected ACV function, given by C_0 . The above arguments on the single-point statistics and expected autocovariance have also been verified numerically, through computing the statistics of many noise functions. Some example noise functions are demonstrated in Fig. 28.

We now bring back the physical meaning in the noise function q . Just like each value in the discrete ACV function C_0 is associated with an offset $\Delta_k = k \cdot \Delta$, each function value q_k is associated with the noise function q evaluated at x_k , and with a total of N points, we have

$$x_k = \frac{2k + 1 - N}{N} \quad \text{for } k = 0, 1, \dots, N - 1 \quad (\text{S.44})$$

Importantly, q has the same length as the discrete function C_0 , and we have $\Delta = x_k - x_{k-1} = 2/N$. In our framework we use $N = 1024$, giving rise to noise functions q explicitly defined at densely sampled $\{x_k\}$ in $(-1, 1)$. But in fact, q can be used as a continuous noise function, and we show how to interpolate q to compute $q(x)$, for $x \in (x_k, x_{k+1})$, while maintaining the properties

$$E[q(x)] = 0; \quad \text{Var}[q(x)] = 1 \quad (\text{S.45})$$

We first write x as

$$x = (1 - t) \cdot x_k + t \cdot x_{k+1}, \quad \text{where } 0 < t < 1 \quad (\text{S.46})$$

and then define

$$\begin{aligned} r_1 &= \frac{1 - t}{\sqrt{(1 - t)^2 + t^2 + 2(1 - t)t \cdot C_1}} \\ r_2 &= \frac{t}{\sqrt{(1 - t)^2 + t^2 + 2(1 - t)t \cdot C_1}} \end{aligned} \quad (\text{S.47})$$

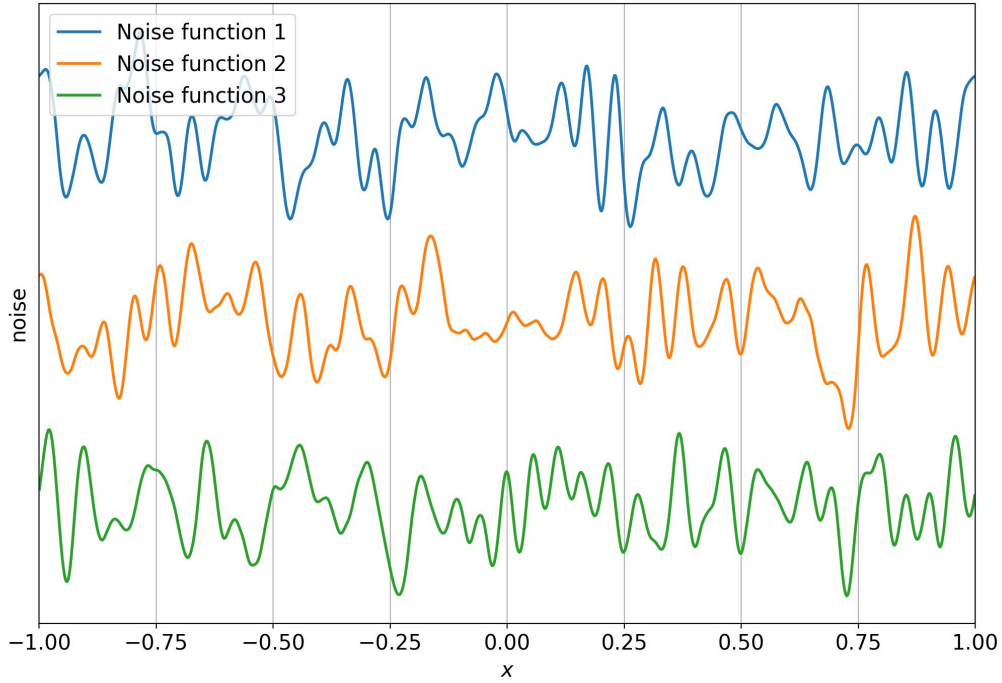


Figure 28: Some example noise functions generated in our Gaussian process.

recalling that $C_1 = C_0(\Delta) = C_0(2/N)$, the autocovariance value corresponding to the smallest positive offset under our discretization resolution. We show that the specially designed interpolation scheme $q(x) = r_1 \cdot q(x_k) + r_2 \cdot q(x_{k+1})$ guarantees the properties in Eq. S.45.

The expected value $E[q(x)] = 0$ follows directly from $E[q(x_k)] = 0$ and $E[q(x_{k+1})] = 0$, and we now show that $\text{Var}[q(x)] = 1$. In fact, we have:

$$\begin{aligned}
q(x) &= r_1 \cdot \sum_{l=1}^{N/2-1} \sqrt{P_l} \cdot [(a_l + b_l i) e^{2\pi i k l / N} + (a_l - b_l i) e^{-2\pi i k l / N}] \\
&\quad + r_2 \cdot \sum_{l=1}^{N/2-1} \sqrt{P_l} \cdot [(a_l + b_l i) e^{2\pi i (k+1) l / N} + (a_l - b_l i) e^{-2\pi i (k+1) l / N}] \\
&= r_1 \cdot \sum_{l=1}^{N/2-1} \sqrt{P_l} \cdot (2 \cos \frac{2\pi k l}{N} \cdot a_l - 2 \sin \frac{2\pi k l}{N} \cdot b_l) \\
&\quad + r_2 \cdot \sum_{l=1}^{N/2-1} \sqrt{P_l} \cdot (2 \cos \frac{2\pi (k+1) l}{N} \cdot a_l - 2 \sin \frac{2\pi (k+1) l}{N} \cdot b_l) \\
&= 2 \sum_{l=1}^{N/2-1} \sqrt{P_l} \cdot [(r_1 \cos \frac{2\pi k l}{N} + r_2 \cos \frac{2\pi (k+1) l}{N}) \cdot a_l - (r_1 \sin \frac{2\pi k l}{N} + r_2 \sin \frac{2\pi (k+1) l}{N}) \cdot b_l]
\end{aligned} \tag{S.48}$$

and so

$$\begin{aligned}
\text{Var}[q(x)] &= 4 \sum_{l=1}^{N/2-1} P_l \cdot (r_1 \cos \frac{2\pi kl}{N} + r_2 \cos \frac{2\pi(k+1)l}{N})^2 \cdot \text{Var}(a_l) \\
&\quad + 4 \sum_{l=1}^{N/2-1} P_l \cdot (r_1 \sin \frac{2\pi kl}{N} + r_2 \sin \frac{2\pi(k+1)l}{N})^2 \cdot \text{Var}(b_l) \\
&= 2 \sum_{l=1}^{N/2-1} P_l \cdot [r_1^2 + r_2^2 + 2r_1r_2(\cos \frac{2\pi kl}{N} \cos \frac{2\pi(k+1)l}{N} + \sin \frac{2\pi kl}{N} \sin \frac{2\pi(k+1)l}{N})] \\
&= 2(r_1^2 + r_2^2) \sum_{l=1}^{N/2-1} P_l + 4r_1r_2 \sum_{l=1}^{N/2-1} P_l \cdot \cos \frac{2\pi l}{N} \\
&= r_1^2 + r_2^2 + 2r_1r_2 \sum_{l=0}^{N-1} P_l \cdot \cos \frac{2\pi l}{N} \\
&= r_1^2 + r_2^2 + 2r_1r_2 C_1 \\
&= 1 \quad \text{using Eq. S.47}
\end{aligned} \tag{S.49}$$

recalling that $\text{Var}(a_l) = \text{Var}(b_l) = 0.5$. Note that when C_1 is close to 1, the scheme reduces to linear interpolation. Also note that increasing the resolution in the space domain samples x_0, x_1, \dots, x_{N-1} (i.e. increasing N and thereby decreasing $x_{k+1} - x_k$) brings the discrete ACV function value C_1 closer to 1.

This way, q can be used as a continuous function in $(-1, 1)$. For evaluating q outside of the range $(-1, 1)$, we note that since q is generated from a DFT process, it is in fact periodic. This periodicity in q creates no visible artifact in our synthesized BRDF—since we rarely need to evaluate q outside of $(-1, 1)$ and the specular lobe of each BRDF corresponds to a small range of x —but allows us to evaluate q for any x .

4.5 BRDF Polarization Dependence

As a closing note for Section 4, we mention that when we discussed our BRDF model parameters $m_{\text{eff}}, \phi_{\text{eff}}, F_{\text{eff}}, m_{\text{sta}}, \phi_{\text{sta}}, F_{\text{sta}}$, and l , we have omitted our discussion on polarization of the incident light. We add in the relevant details here.

To model unpolarized light, for each (λ, ω_i) we perform two sets of simulations using incident fields with mutually perpendicular electric field vectors. Our BRDF generation pipeline discussed in the main paper therefore should be performed twice for the two polarizations. Still, in practice, we tend to construct one set of BRDFs, by averaging the computed BRDF parameters from the two polarizations. In fact, for the same barbule instances, simulations corresponding to both polarizations tend to yield very similar $m_{\text{eff}}(\lambda, \omega_i), \phi_{\text{eff}}(\lambda, \omega_i), m_{\text{sta}}(\lambda, \omega_i), \phi_{\text{sta}}(\lambda, \omega_i)$, and $l(\lambda, \omega_i)$. Moreover, $F_{\text{eff}}(\lambda, \omega_i), F_{\text{sta}}(\lambda, \omega_i)$ are related to the scattering intensities and should be averaged to model unpolarized light. Of course, if we wish to keep the polarizations separate, we can generate two sets of BRDFs using the BRDF parameters computed from simulation results corresponding to the two polarizations.

In the next few figures, we present examples of BRDF instances synthesized using our pipeline presented in the main paper and this document. Each BRDF instance is visualized as hemisphere plots and each hemisphere plot features an incident direction and draws the BRDF as a function of the outgoing direction.

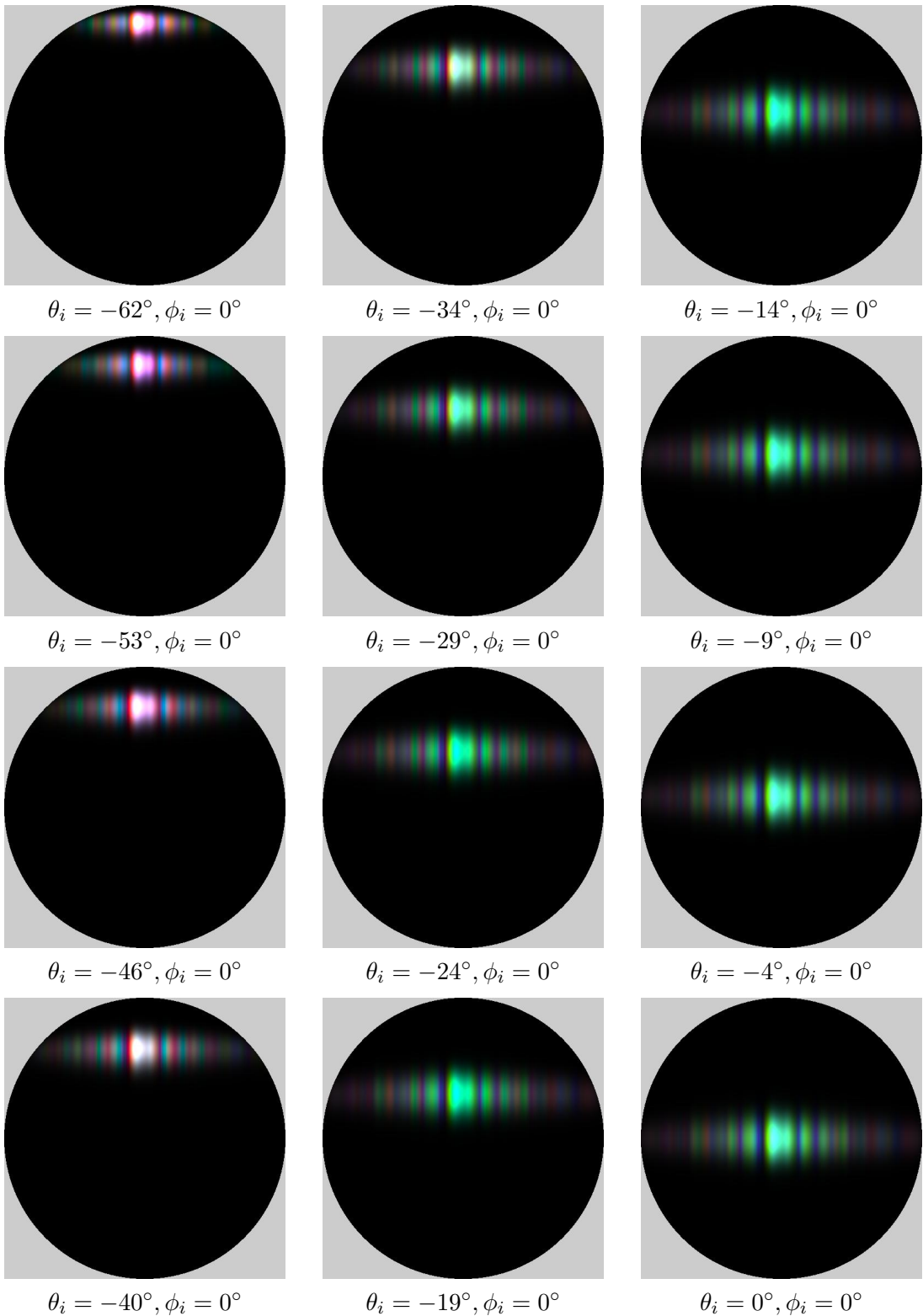


Figure 29: A 2.5D BRDF instance representing a rock dove barbule, visualized for many incident angles.

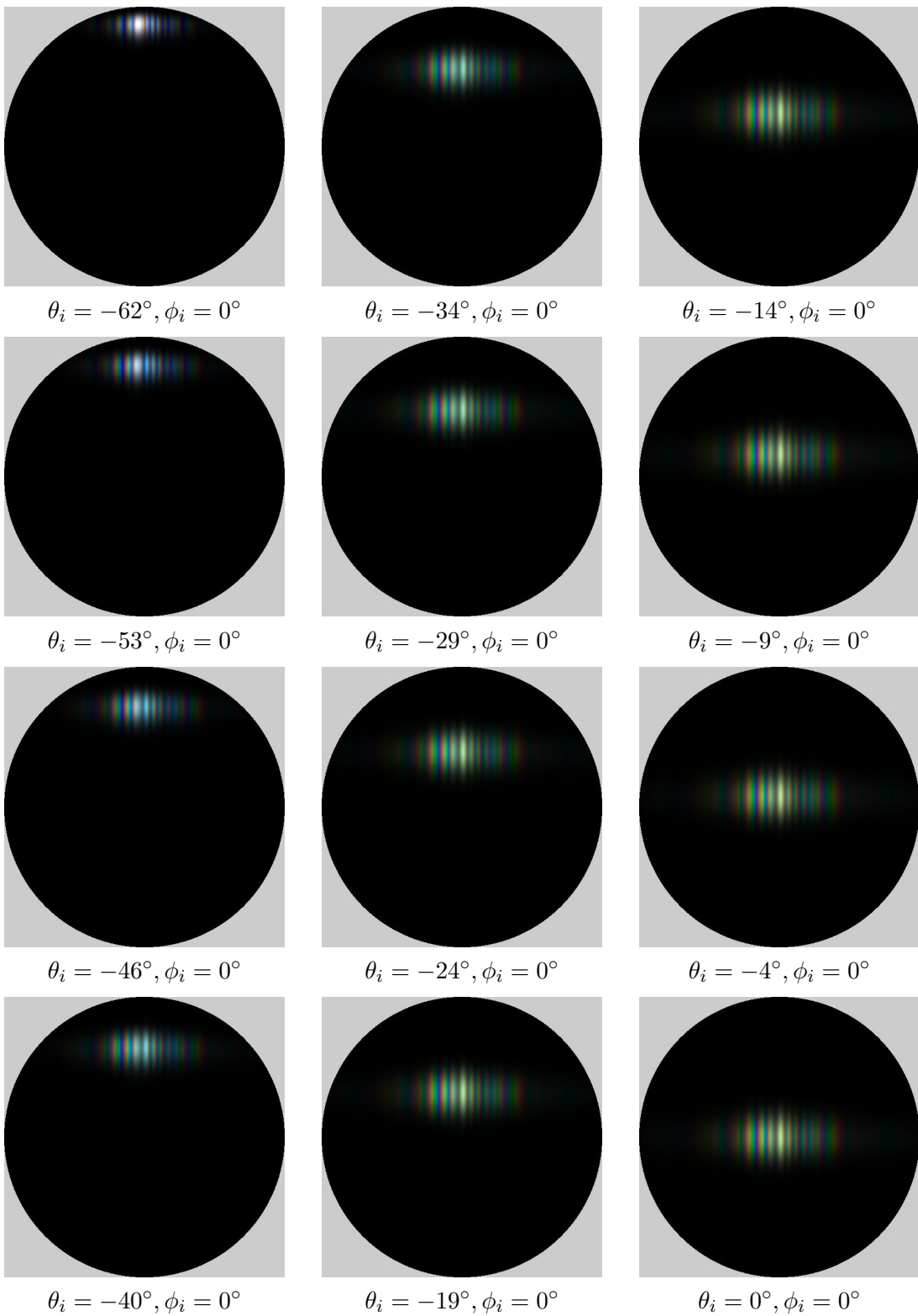


Figure 30: A 2.5D BRDF instance representing a starling barbule, visualized for many incident angles.

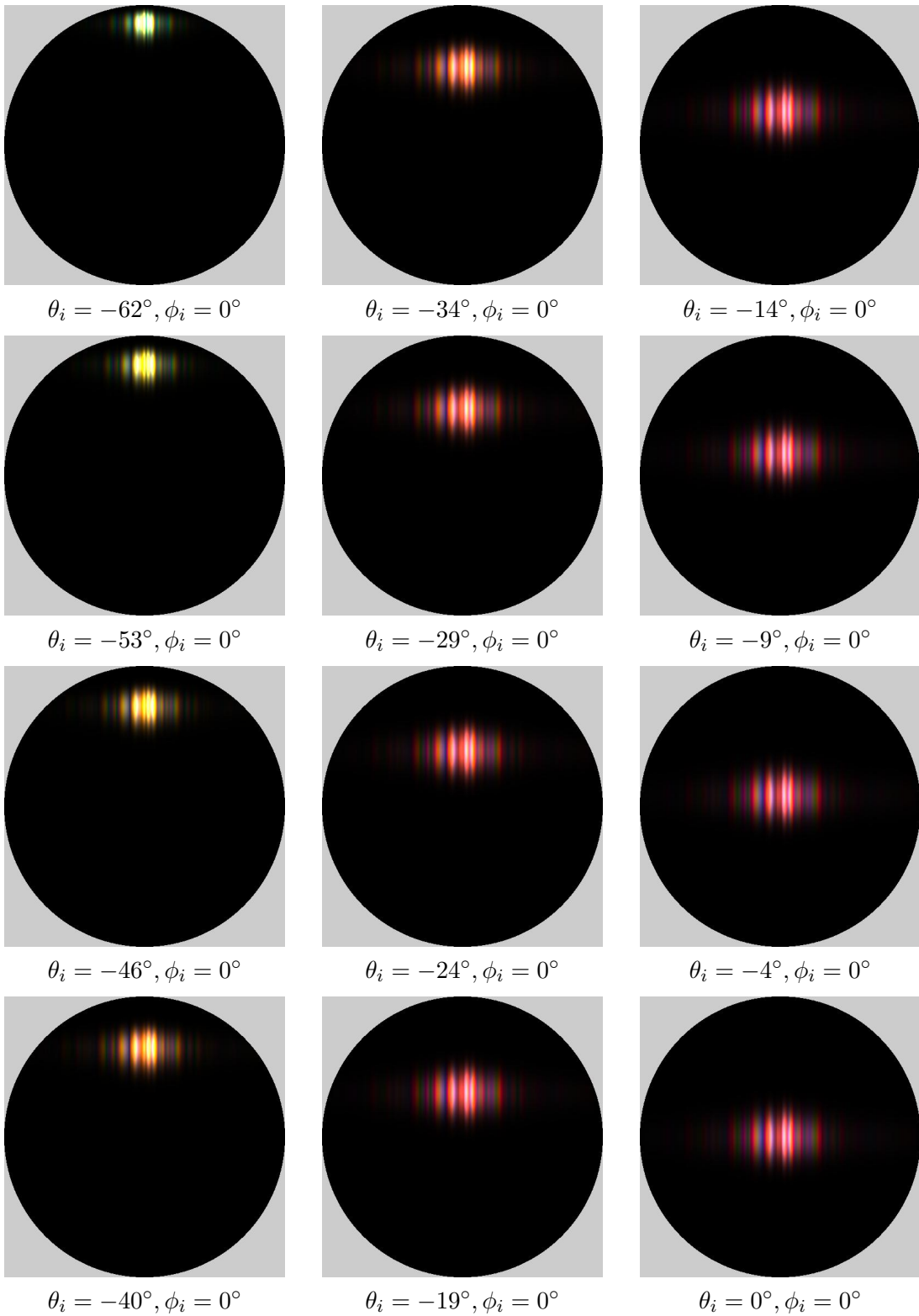


Figure 31: A 2.5D BRDF instance representing a bronzewing barbule, visualized for many incident angles.

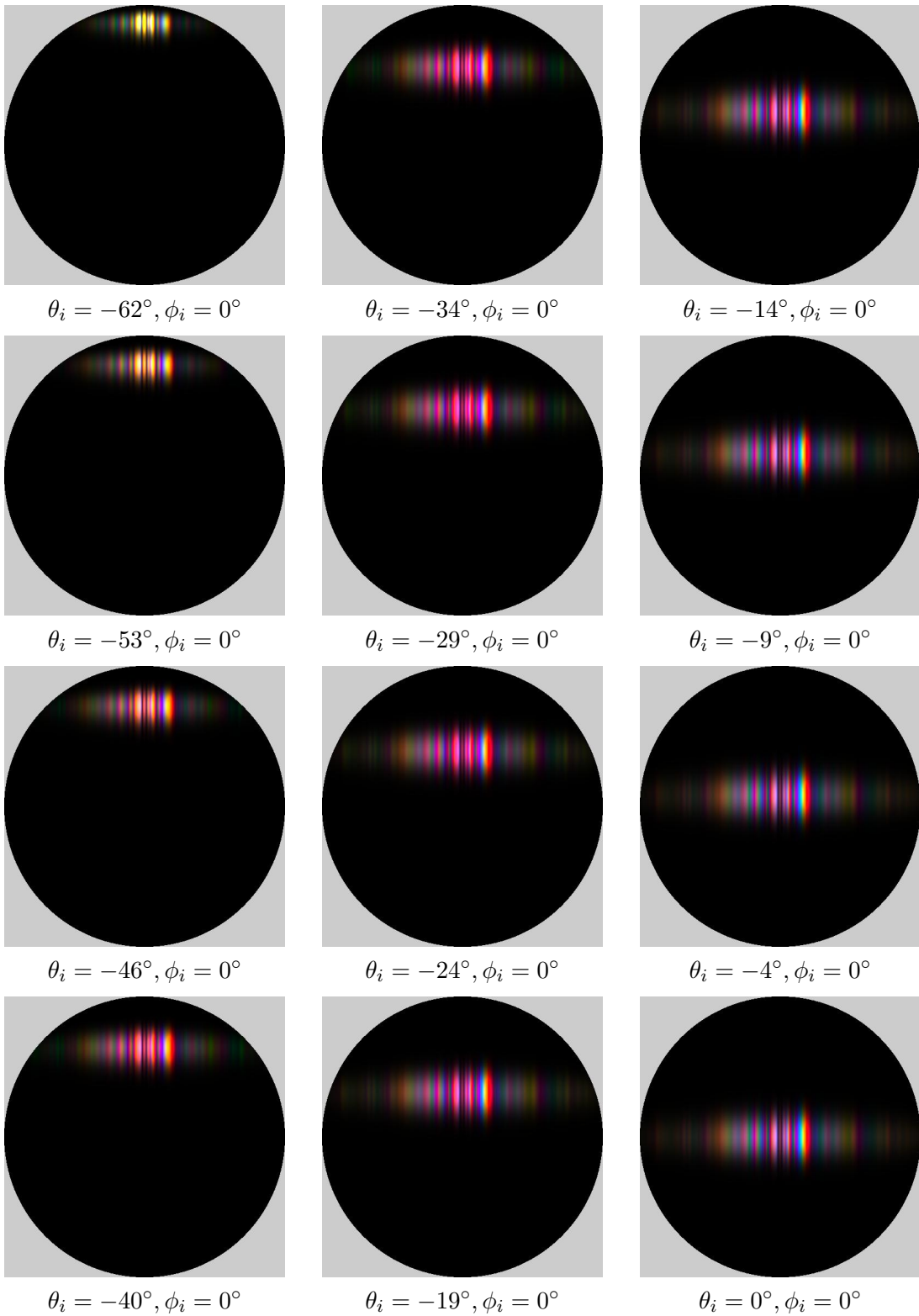


Figure 32: A 2.5D BRDF instance for a hummingbird barbule, visualized for many incident angles.

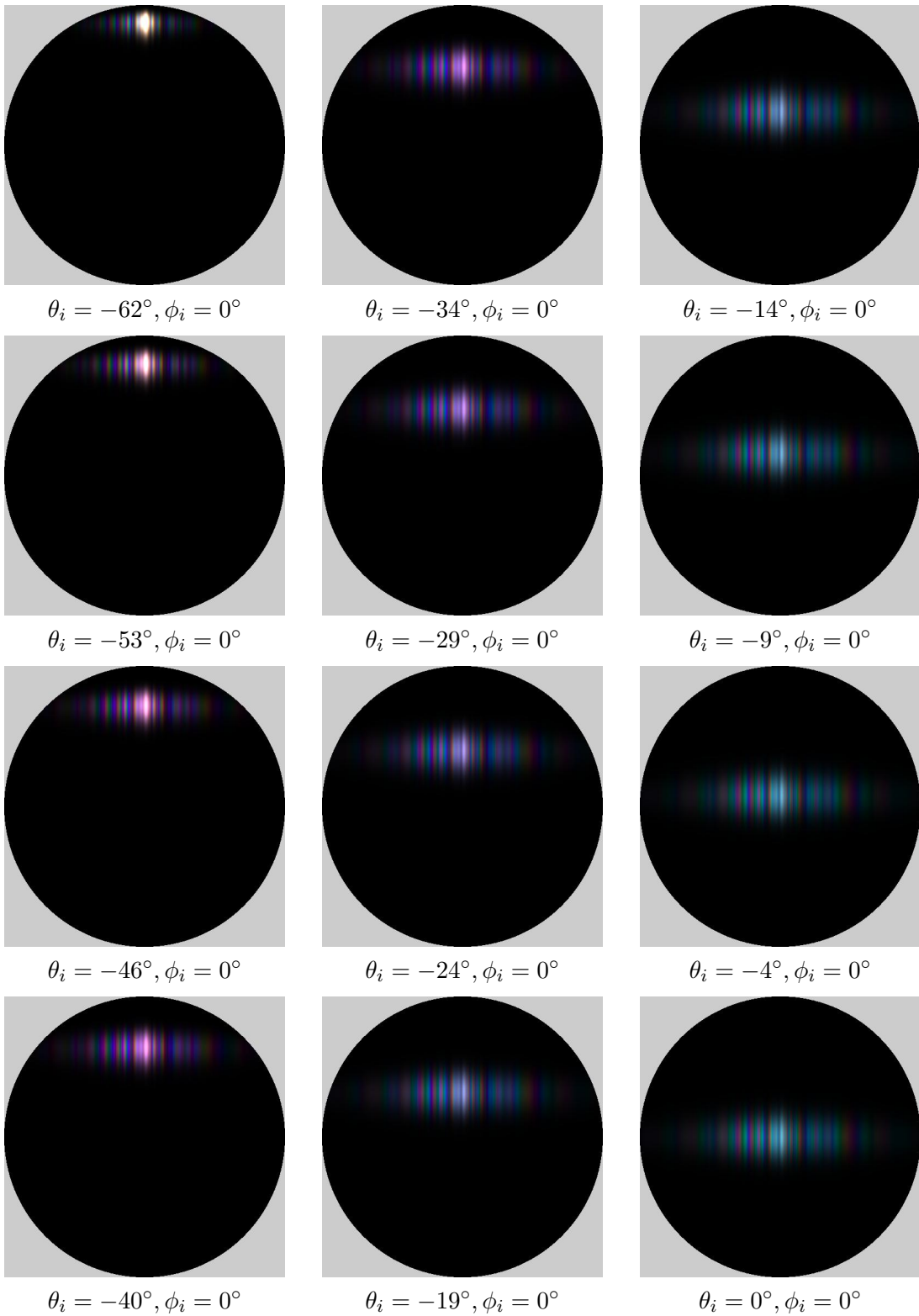


Figure 33: A 2.5D BRDF instance representing a mallard barbule, visualized for many incident angles.

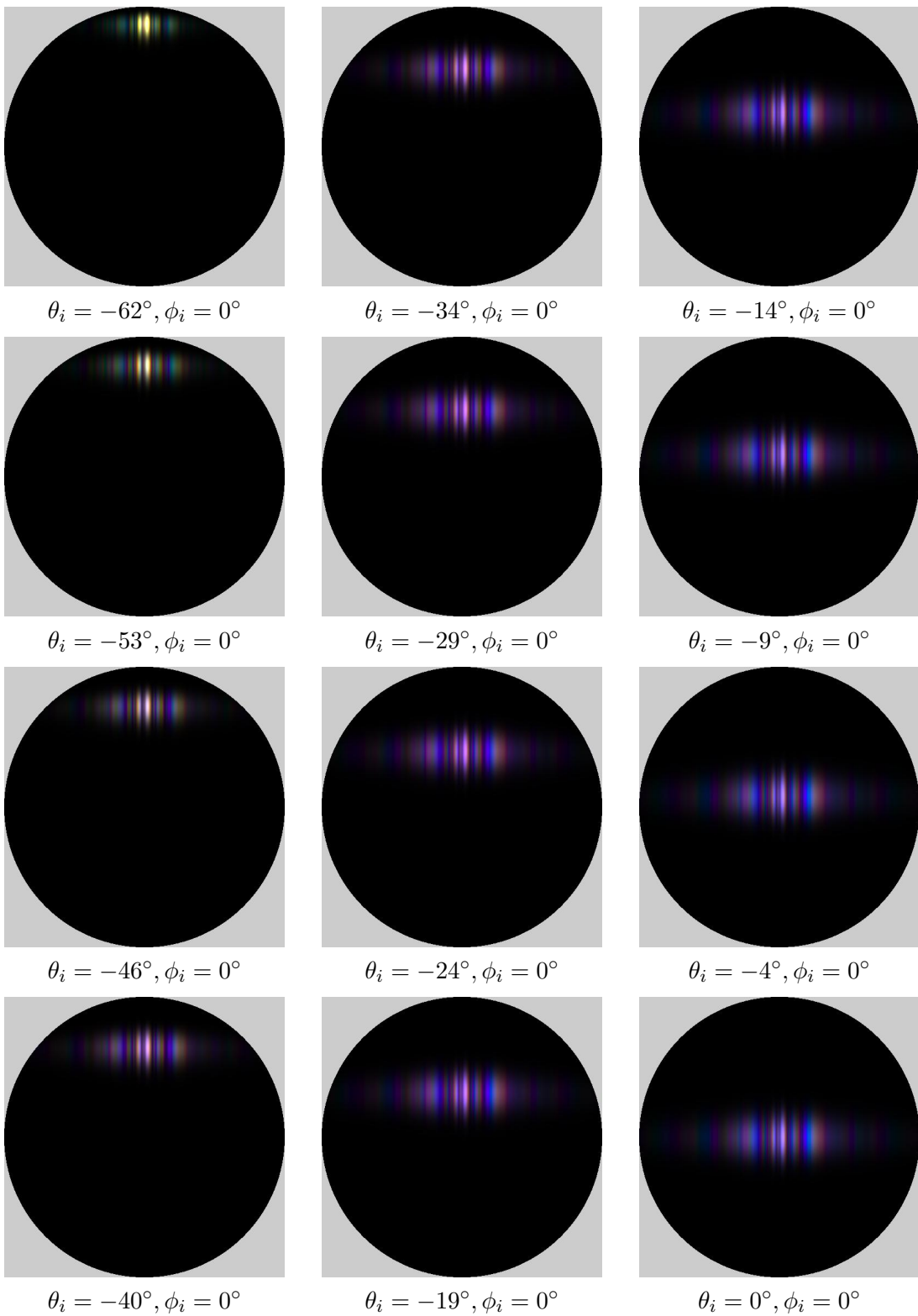


Figure 34: A 2.5D BRDF instance representing a magpie barbule, visualized for many incident angles.

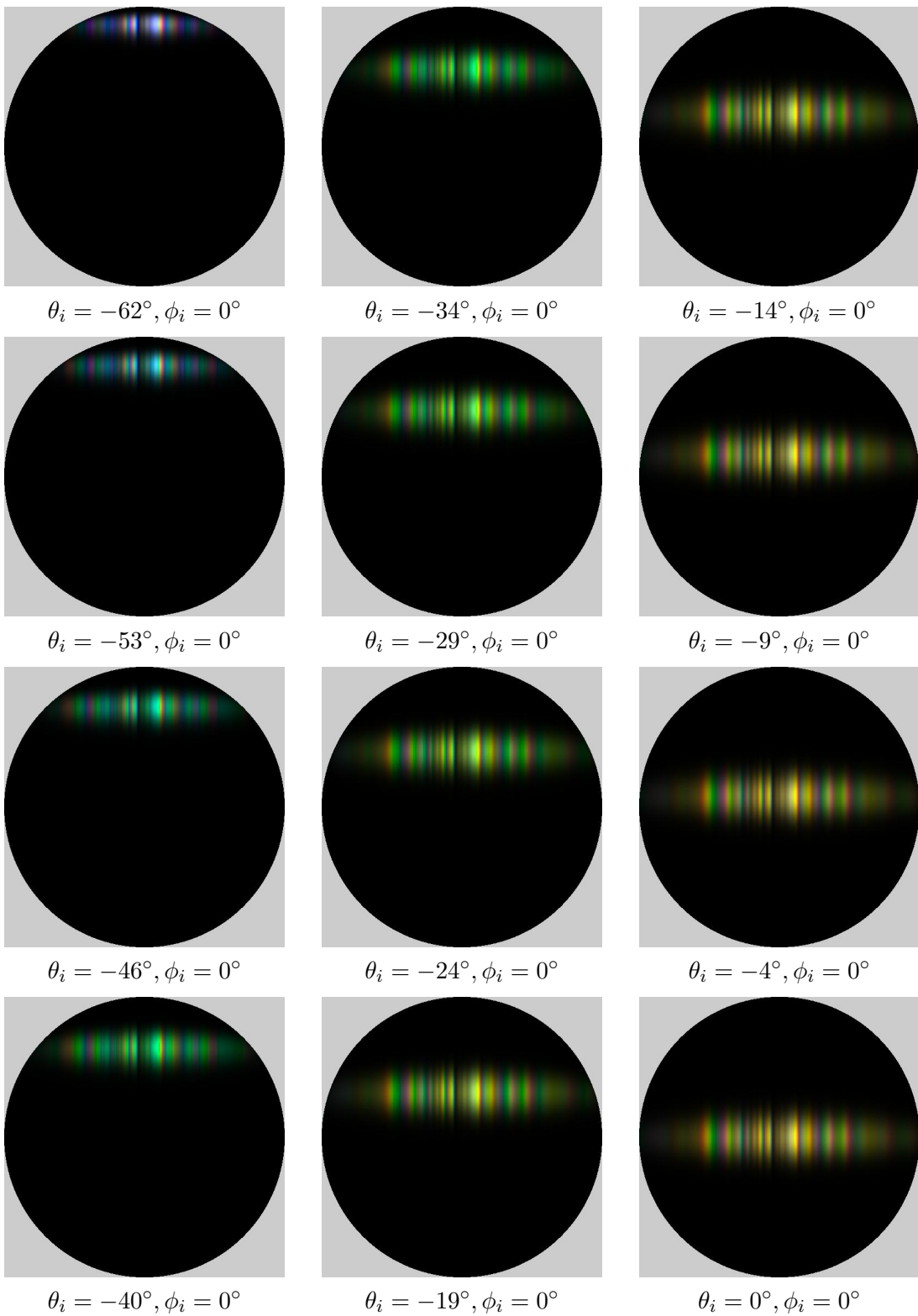


Figure 35: A 2.5D BRDF instance representing a peacock barbule, visualized for many incident angles.

5 Validations with Full-Wave Simulations

In Section 6.1 of our main paper, we validated our fast, approximate wave simulation results against full-wave simulation results. Here we hope to provide details on the principles behind our full-wave simulations, which work on structures with fairly arbitrary internal structures. We also provide the full set of comparisons made between full-wave and approximate simulation results, which we did not get to include in the main paper.

5.1 The Boundary Element Method on Multi-Component Objects

Given a specified barbule cross section, the most accurate way to compute scattering is to perform a full-wave simulation, which is fundamentally based on solving Maxwell's equations. We implemented a full-wave simulator based on the boundary element method (BEM). This simulator serves as a slow reference tool that validates our approximate simulation method.

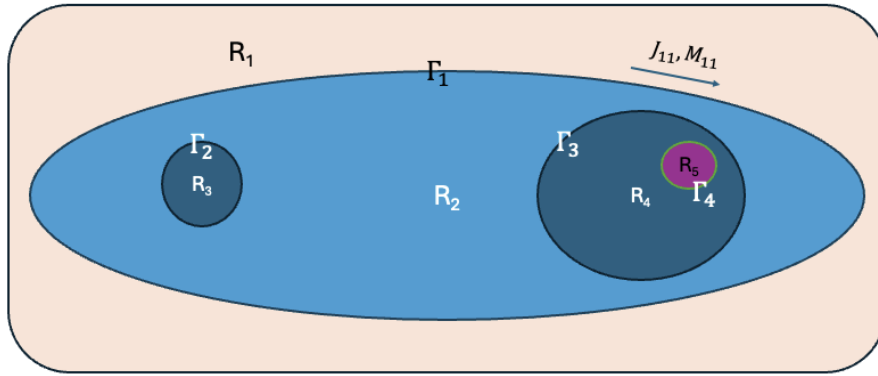


Figure 36: An illustration of a multi-component structure that can be simulated using BEM.

Our implementation of BEM generalizes previous versions proposed in (Xia et al., 2020) and (Yu et al., 2023), which target problems that only involve one scattering object with a uniform IOR. As shown in Fig. 36, our barbule needs to be modeled as a multi-component scattering object, containing N_b boundaries that divides the simulation domain into N_r regions. In our simulations, we work with complex-valued field quantities that carry both amplitude and phase information. We also assume that these field quantities are time-harmonic, with their time dependence given by $e^{-j\omega t}$. The term $e^{-j\omega t}$ is suppressed throughout the text. BEM computes the electromagnetic field in the simulation domain by solving Maxwell's equations, whose time-harmonic form is given by

$$\begin{aligned}\nabla \times \mathbf{E} &= -\mathbf{M} + j\omega\mu\mathbf{H} \\ \nabla \times \mathbf{H} &= \mathbf{J} - j\omega\varepsilon\mathbf{E}\end{aligned}\tag{S.50}$$

where \mathbf{E} and \mathbf{H} are the electric and magnetic fields, and \mathbf{J} and \mathbf{M} are the electric and magnetic current densities, which are fictitious quantities introduced in BEM simulations. μ and ε are the permeability and permittivity of the space, which are collectively referred to as the constitutive parameters.

We denote the boundaries in the scattering object as $\Gamma_1, \Gamma_2, \dots, \Gamma_{N_b}$, and denote the regions in the simulation space as R_1, R_2, \dots, R_{N_r} . The constitutive parameters of region R_k are (ε_k, μ_k) , and the electric and magnetic fields in R_i are given by $\mathbf{E}_k, \mathbf{H}_k$. BEM works by converting the simulation problem—which involves a non-homogeneous domain due to the scattering object—into N_r subproblems with homogeneous domains. In the subproblem k , the constitutive parameters of the entire domain are set to (ε_k, μ_k) ; the fields inside R_k remain to be $\mathbf{E}_k, \mathbf{H}_k$, while the fields are set to zero everywhere else.

This formulation implies that in each subproblem, the electromagnetic fields are discontinuous across region boundaries. To address these discontinuities, fictitious surface currents are introduced on each side of each boundary Γ_l . Specifically, we let $R_{k_1(l)}, R_{k_2(l)}$ be the two regions that border the two sides of Γ_l , and denote the current densities on the two sides as $\mathbf{J}_{l1}, \mathbf{M}_{l1}$ and $\mathbf{J}_{l2}, \mathbf{M}_{l2}$. Boundary conditions of Maxwell's equations, applied in subproblems $k_1(l)$ and $k_2(l)$, require that at each point \mathbf{r} on Γ_l

$$\begin{aligned} \mathbf{J}_{l1}(\mathbf{r}) &= \mathbf{n}_{l1}(\mathbf{r}) \times \mathbf{H}_{k_1(l)}(\mathbf{r}); & \mathbf{M}_{l1}(\mathbf{r}) &= -\mathbf{n}_{l1}(\mathbf{r}) \times \mathbf{E}_{k_1(l)}(\mathbf{r}) \\ \mathbf{J}_{l2}(\mathbf{r}) &= \mathbf{n}_{l2}(\mathbf{r}) \times \mathbf{H}_{k_2(l)}(\mathbf{r}); & \mathbf{M}_{l2}(\mathbf{r}) &= -\mathbf{n}_{l2}(\mathbf{r}) \times \mathbf{E}_{k_2(l)}(\mathbf{r}) \end{aligned} \quad (\text{S.51})$$

where \mathbf{n}_{l1} and \mathbf{n}_{l2} are normal vectors of Γ_l that points into $R_{k_1(l)}$ and $R_{k_2(l)}$, respectively, so $\mathbf{n}_{l1} = -\mathbf{n}_{l2}$. Additionally, the net current densities on Γ_l are required to be zero, i.e.

$$\mathbf{J}_{l1}(\mathbf{r}) + \mathbf{J}_{l2}(\mathbf{r}) = \mathbf{0}; \quad \mathbf{M}_{l1}(\mathbf{r}) + \mathbf{M}_{l2}(\mathbf{r}) = \mathbf{0} \quad (\text{S.52})$$

Note that this guarantees that the tangential components of the electromagnetic fields are continuous across all boundaries in the original, full scattering problem.

As shown in Fig. 36, R_1 represents the region where the incident fields $\mathbf{E}_i, \mathbf{H}_i$ are defined. The total fields in R_1 can be written as $\mathbf{E}_1 = \mathbf{E}_i + \mathbf{E}_s$ and $\mathbf{H}_1 = \mathbf{H}_i + \mathbf{H}_s$, where $\mathbf{E}_s, \mathbf{H}_s$ are the scattered fields induced by the scattering object.

Let Γ_1 be the boundary that borders R_1 and $\mathbf{J}_{11}, \mathbf{M}_{11}$ be the current densities on the exterior side of Γ_1 . The surface equivalence principle (Schelkunoff, 1936) states that \mathbf{E}_s and \mathbf{H}_s can be seen as generated by \mathbf{J}_{11} and \mathbf{M}_{11} , radiating in a homogeneous medium with constitutive parameters (ε_1, μ_1) —in the context of subproblem 1. Thus, $\mathbf{E}_s, \mathbf{H}_s$ can be computed from $\mathbf{J}_{11}, \mathbf{M}_{11}$ through the “source-field relationships” in homogeneous region, which are derived from Maxwell's equations. In a homogeneous region with constitutive parameters (ε_k, μ_k) , the source-field relationships are given by

$$\begin{aligned} \mathbf{E}_{\text{sca}}^k(\mathbf{r}; \mathbf{J}, \mathbf{M}) &= j\omega\mu_k(\mathcal{L}\mathbf{J}_k)(\mathbf{r}) - (\mathcal{K}_k\mathbf{M})(\mathbf{r}) \\ \mathbf{H}_{\text{sca}}^k(\mathbf{r}; \mathbf{J}, \mathbf{M}) &= j\omega\varepsilon_k(\mathcal{L}_k\mathbf{M})(\mathbf{r}) + (\mathcal{K}_k\mathbf{J})(\mathbf{r}) \end{aligned} \quad (\text{S.53})$$

where the operators $\mathcal{L}_k, \mathcal{K}_k$ integrate the current densities \mathbf{J}, \mathbf{M} over the boundary they reside on. The specific forms of these operators can be referenced from (Xia et al., 2020).

The electromagnetic field in R_k , for $k = 2, 3, \dots, N_r$, can similarly be seen as generated by surface currents on the boundaries that border these regions—radiating in a homogeneous medium with constitutive parameters (ε_k, μ_k) , in the context of subproblem k . Therefore, the total field in each region can be written as:

$$\begin{aligned} \mathbf{E}_1(\mathbf{r}) &= \mathbf{E}_i(\mathbf{r}) + \mathbf{E}_{\text{sca}}^1(\mathbf{r}; \mathbf{J}_{11}, \mathbf{M}_{11}) \\ \mathbf{H}_1(\mathbf{r}) &= \mathbf{H}_i(\mathbf{r}) + \mathbf{H}_{\text{sca}}^1(\mathbf{r}; \mathbf{J}_{11}, \mathbf{M}_{11}) \end{aligned} \quad (\text{S.54})$$

and

$$\begin{aligned}\mathbf{E}_k(\mathbf{r}) &= \sum_{i(k)} \mathbf{E}_{\text{sca}}^k(\mathbf{r}; \mathbf{J}_{i(k)}, \mathbf{M}_{i(k)}) \\ \mathbf{H}_k(\mathbf{r}) &= \sum_{i(k)} \mathbf{H}_{\text{sca}}^k(\mathbf{r}; \mathbf{J}_{i(k)}, \mathbf{M}_{i(k)}) \quad \text{for } k \geq 2\end{aligned}\tag{S.55}$$

where each index $i(k)$ refers to one set of current densities relevant to subproblem k.

Combining Eq. S.51, S.52, S.53, S.54, and S.55 allows us to solve for all the fictitious current densities and compute the electromagnetic field anywhere in the domain. Expectedly, this full-wave simulation is very expensive and can only be used as reference tool.

5.2 Additional Results on Simulation Validation

In Section 6.1 of our main paper, we validated our 2.5D simulation methods for both layer-type and crystal-type barbules, using a pink hummingbird barbule and a blue mallard barbule as our simulation targets. Due to limited spacing, we only presented a subset of our results from comparison different simulation methods. Here we present our whole set of results in terms of three-way or two-way comparisons—some figures are repeated from the main paper.

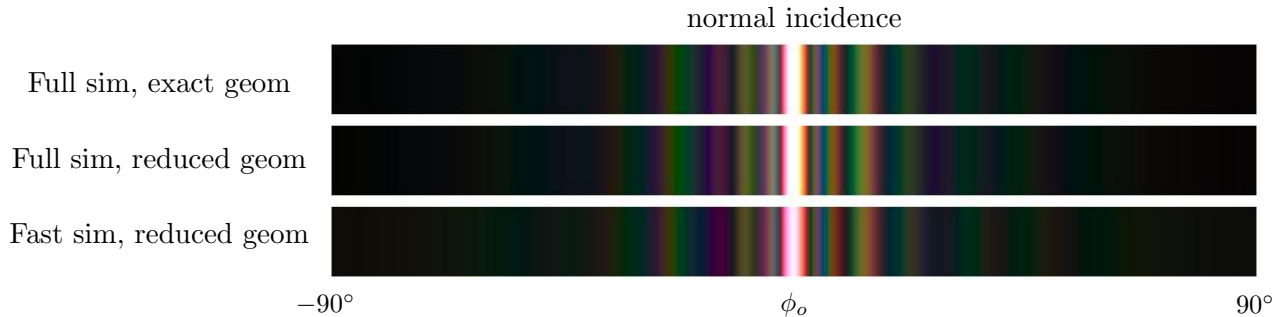


Figure 37: Hummingbird barbule scattering corresponding to 0° incidence, shown in RGB colors.

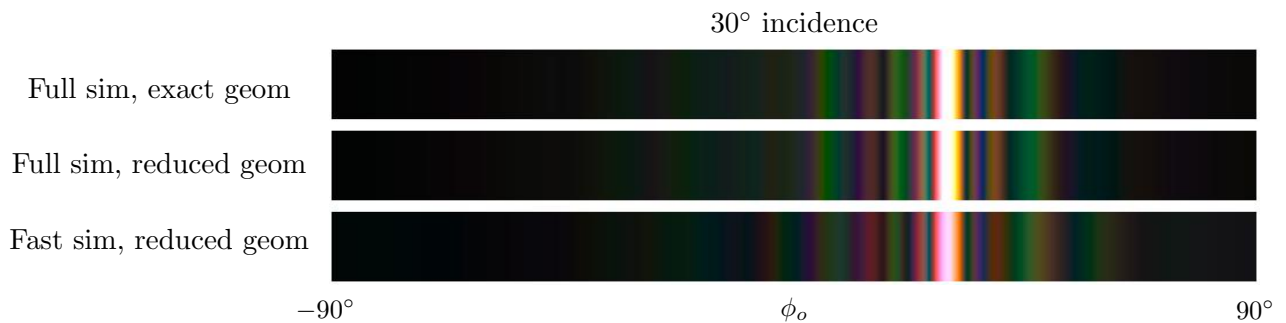


Figure 38: Hummingbird barbule scattering corresponding to 30° incidence, shown in RGB colors.

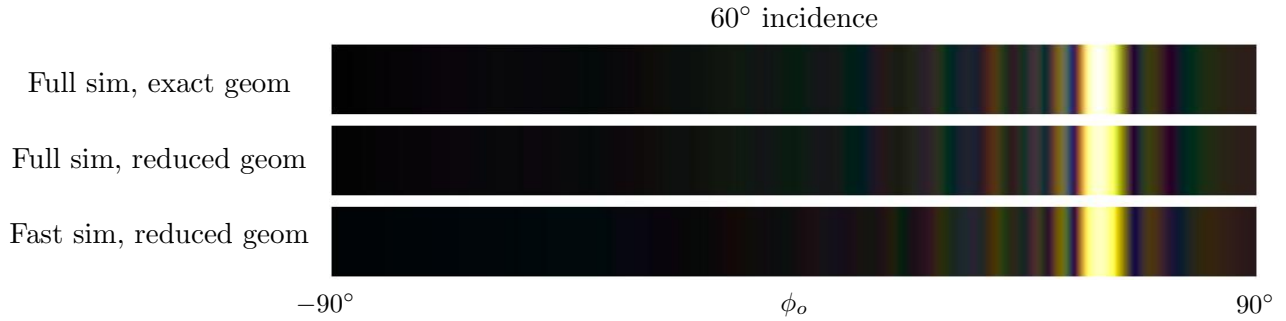


Figure 39: Hummingbird barbule scattering corresponding to 60° incidence, shown in RGB colors.

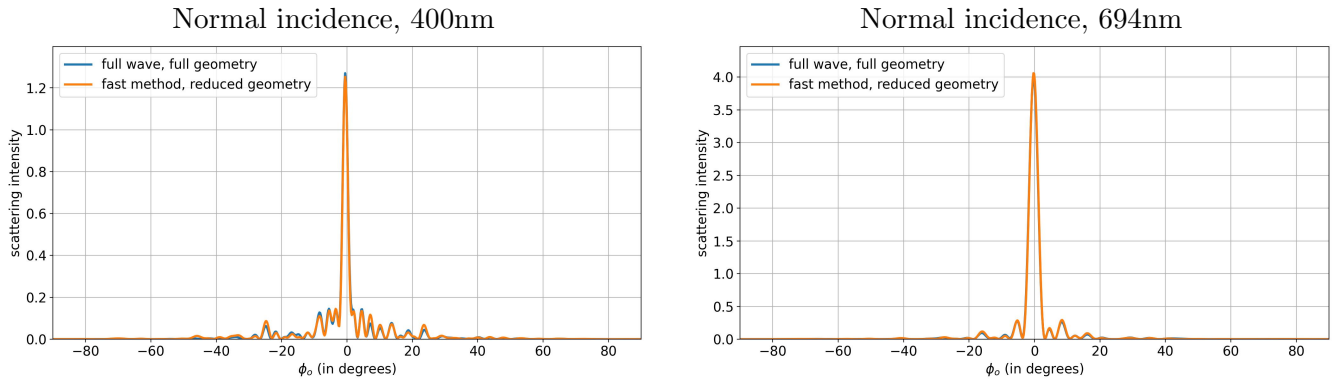


Figure 40: Hummingbird barbule scattering at 0° incidence, shown for $\lambda_1 = 400\text{nm}$ and $\lambda_2 = 694\text{nm}$.

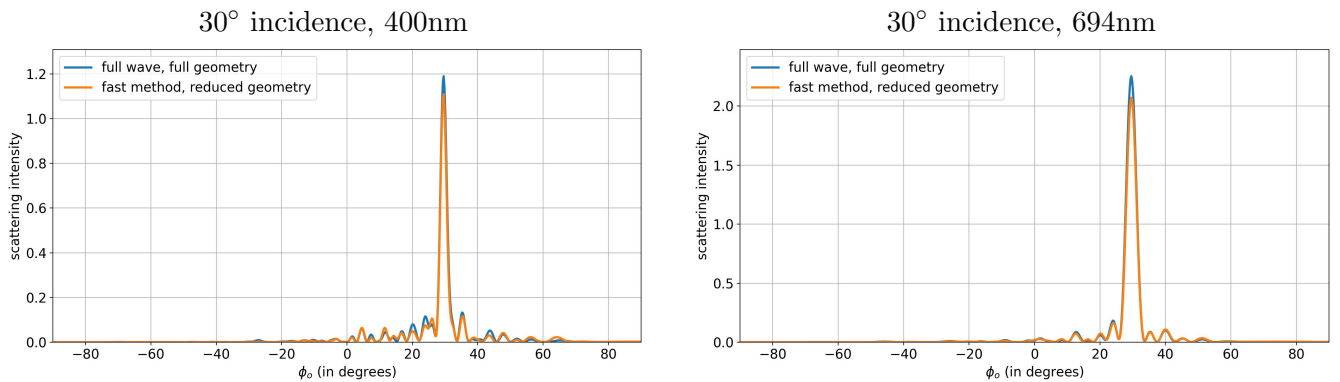


Figure 41: Hummingbird barbule scattering at 30° incidence, shown for $\lambda_1 = 400\text{nm}$ and $\lambda_2 = 694\text{nm}$.

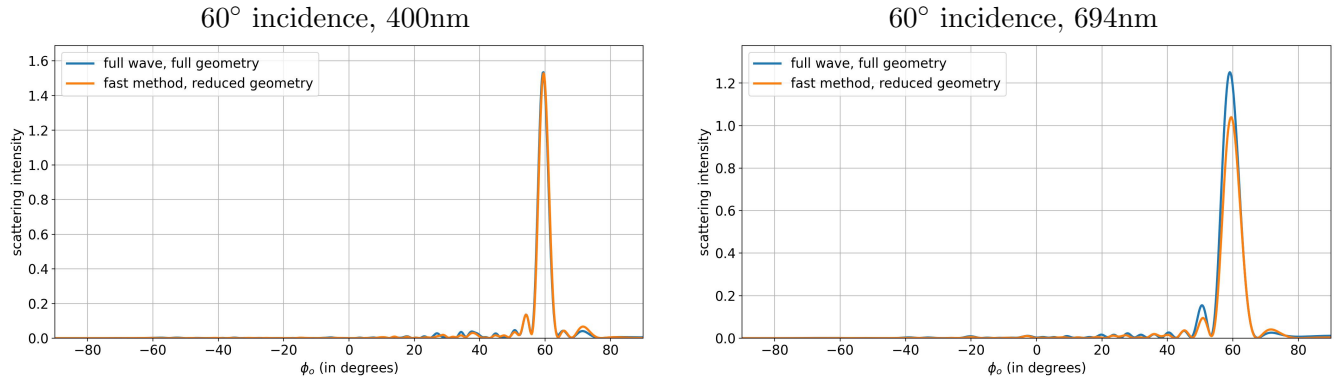


Figure 42: Hummingbird barbule scattering at 60° incidence, shown for $\lambda_1 = 400\text{nm}$ and $\lambda_2 = 694\text{nm}$.

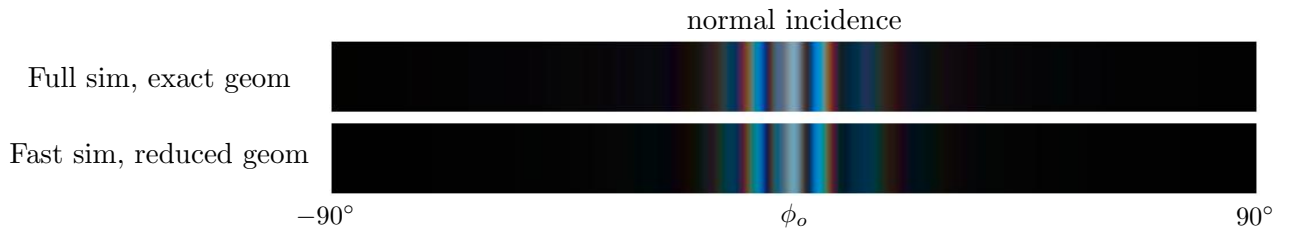


Figure 43: Mallard barbule scattering corresponding to 0° incidence, shown in RGB colors.

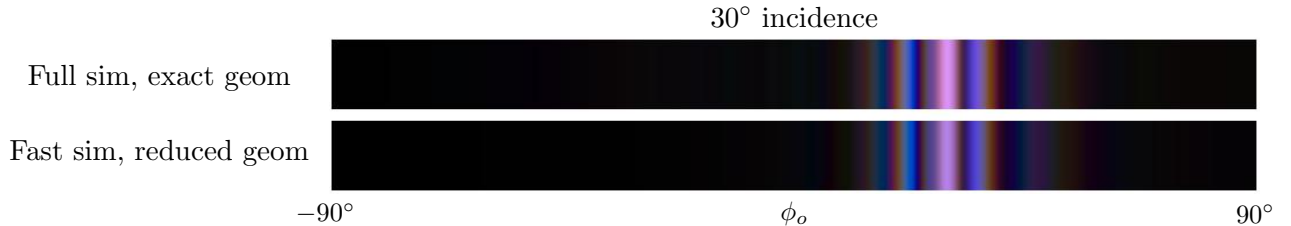


Figure 44: Mallard barbule scattering corresponding to 30° incidence, shown in RGB colors.

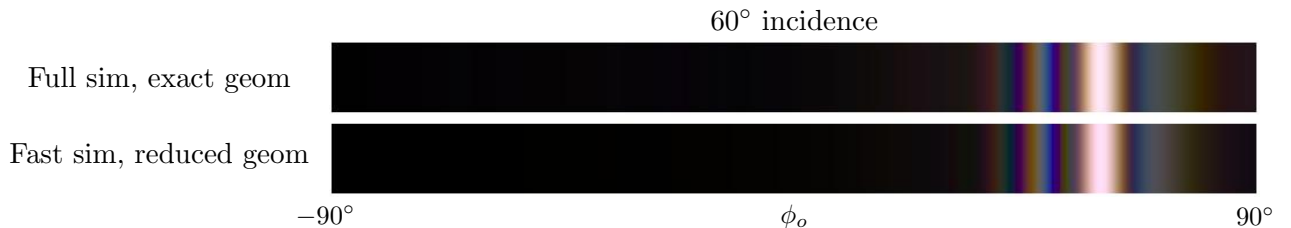
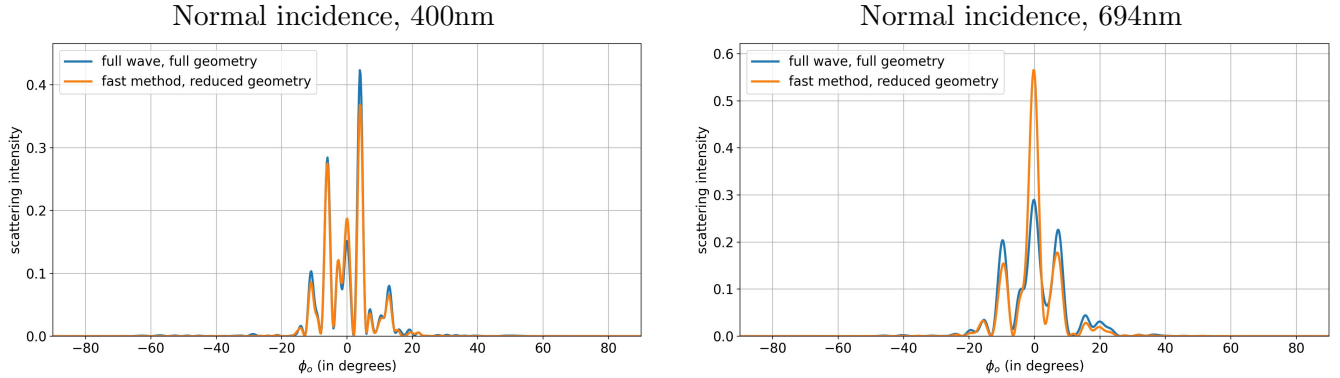
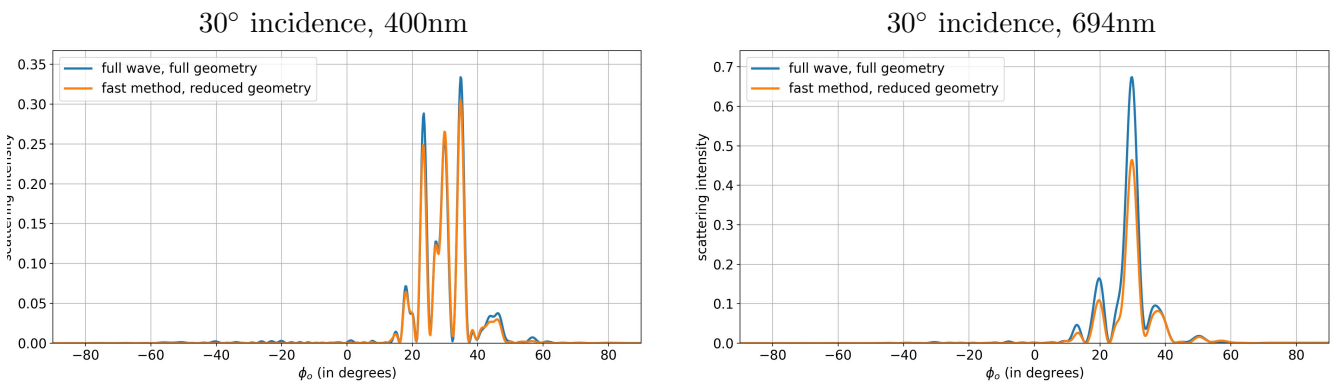
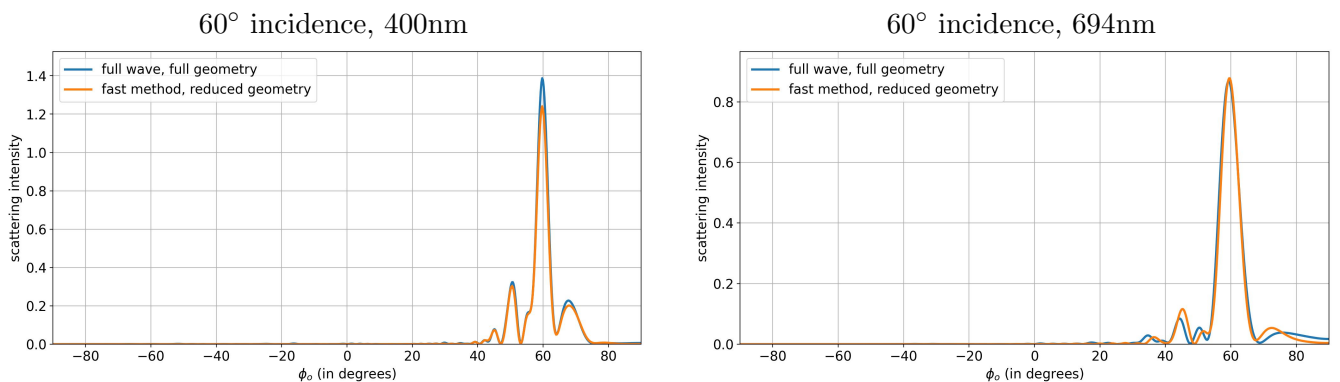


Figure 45: Mallard barbule scattering corresponding to 60° incidence, shown in RGB colors.

Figure 46: Mallard barbule scattering at 0° incidence, shown for $\lambda_1 = 400\text{nm}$ and $\lambda_2 = 694\text{nm}$.Figure 47: Mallard barbule scattering at 30° incidence, shown for $\lambda_1 = 400\text{nm}$ and $\lambda_2 = 694\text{nm}$.Figure 48: Mallard barbule scattering at 60° incidence, shown for $\lambda_1 = 400\text{nm}$ and $\lambda_2 = 694\text{nm}$.

6 Comparing 2.5D and 3D BRDFs

In Section 6.2 of the main paper, we presented 2.5D BRDFs generated using our method, as compared to BRDFs computed from 3D simulations on 3D barbule segments. Here we provide some examples of our 3D barbule structures and also include larger, clearer versions of the BRDF plots shown in the paper.

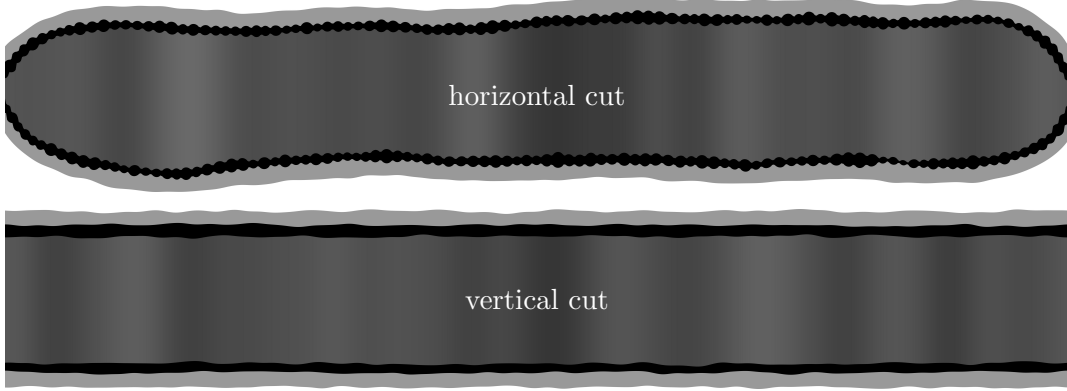


Figure 49: Illustration of a 3D barbule model with approximate translational symmetry.

6.1 Modeling 3D Barbule Segments

To qualify our assumption of translational symmetry in barbule structures, we generated some geometric models for each type of barbule in 3D and simulate these 3D barbules using the 3D version of our approximate simulator. Our goal is to directly compute BRDFs for these 3D barbules using wave simulations, and compare these 3D barbules' BRDFs to those we synthesize from 2.5D simulation results.

Since real barbules indeed have far more structural variations within their cross sections than along their longitudinal axes, most 3D barbule segments we model still have approximate, but not perfect, translational symmetry. These 3D barbule models are mostly adapted from the 2D cross section models—by replicating a cross section along the longitudinal axis and then isotropically perturbing each layer in the 3D model (making rock dove and hummingbird barbules are slightly more involved but the overall shapes of the barbules are also assumed to change very little along the longitudinal axes). As illustrated in Fig. 49, where we show a horizontal cut and a vertical cut obtained from a full, 3D barbule segment. The horizontal cut looks just like a starling barbule cross section that we showed in Fig. 4, and the vertical cut, along the perpendicular direction, shows that the barbule's layer heights are mostly invariant along its longitudinal axis, while we have incorporated some small-scale roughness.

6.2 Comparing BRDF Plots

Lastly, we present full, clearer versions of the BRDF plots that we showed in Section 6.2 of the main paper. Note that the 2.5D smooth BRDFs and BRDF instances were computed and synthesized using our proposed BRDF pipeline, while the 3D BRDF instances were raw simulation results corresponding to some 3D barbule segments, and the 3D smooth BRDFs were computed from averaging individual BRDFs from 50 simulated barbules (so they look not as smooth as the analytical, 2.5D smooth BRDFs).

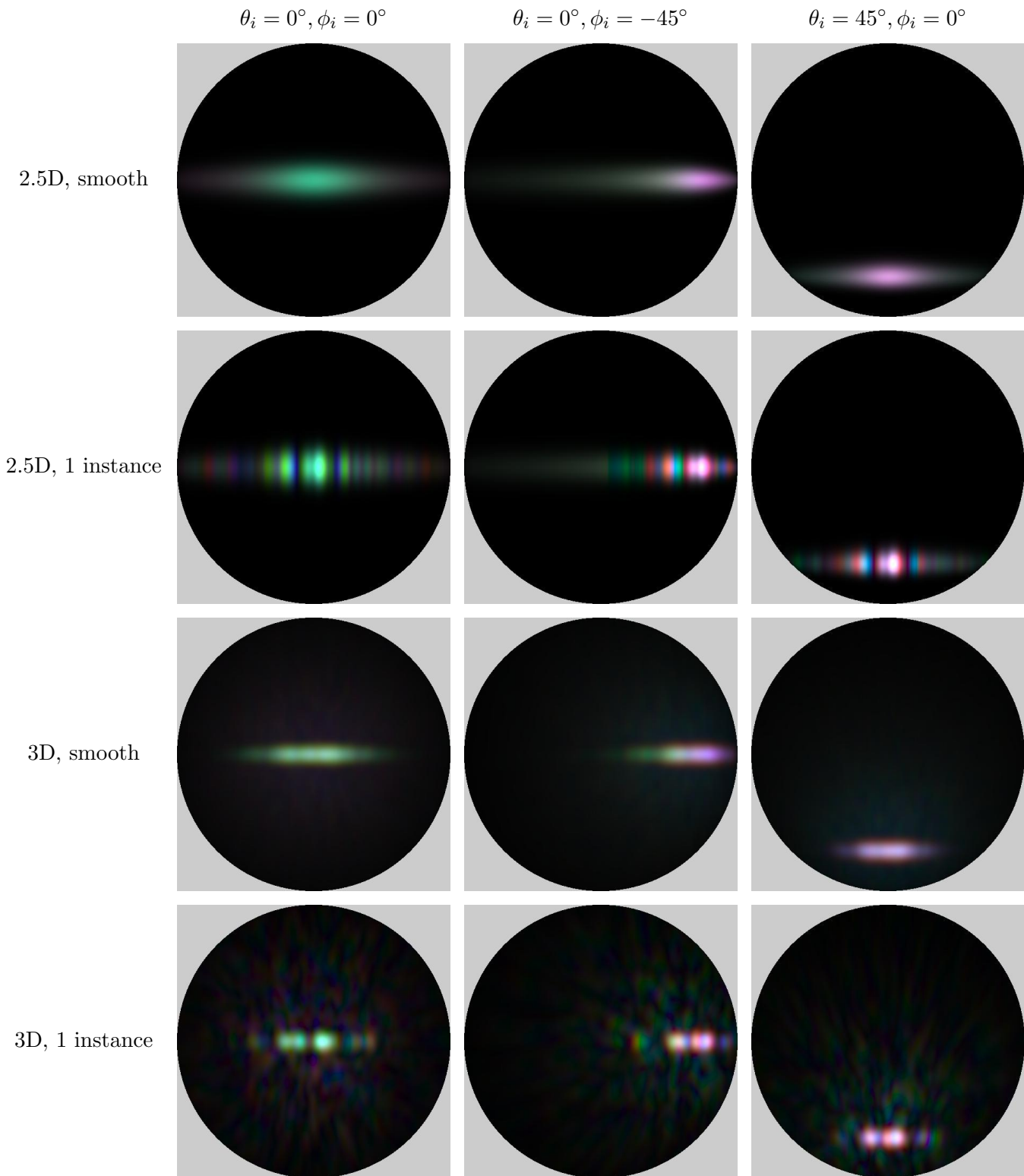


Figure 50: Comparing 2.5D and 3D BRDFs for rock dove barbules, featuring three incident directions.

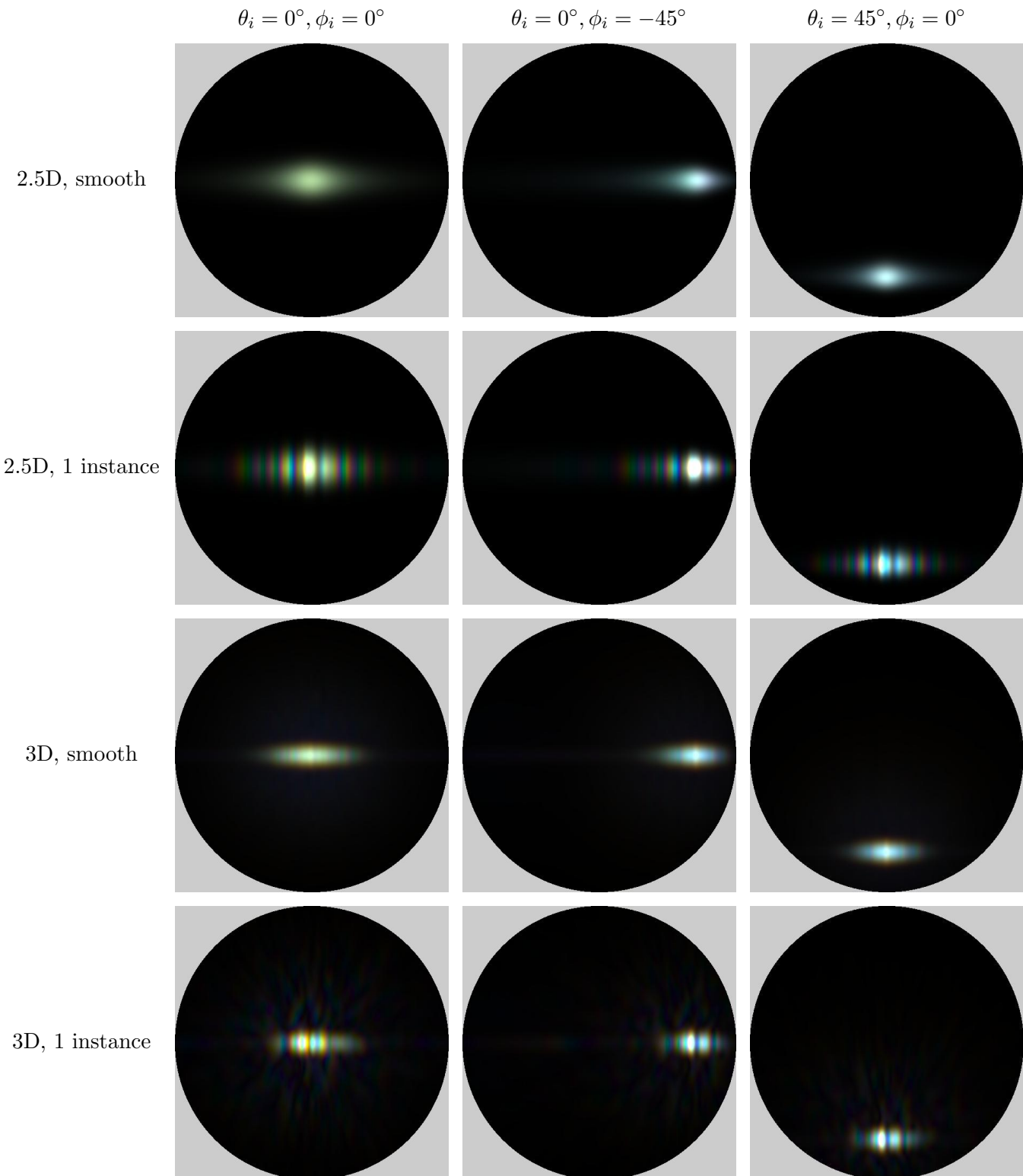


Figure 51: Comparing 2.5D and 3D BRDFs for starling barbules, featuring three incident directions.

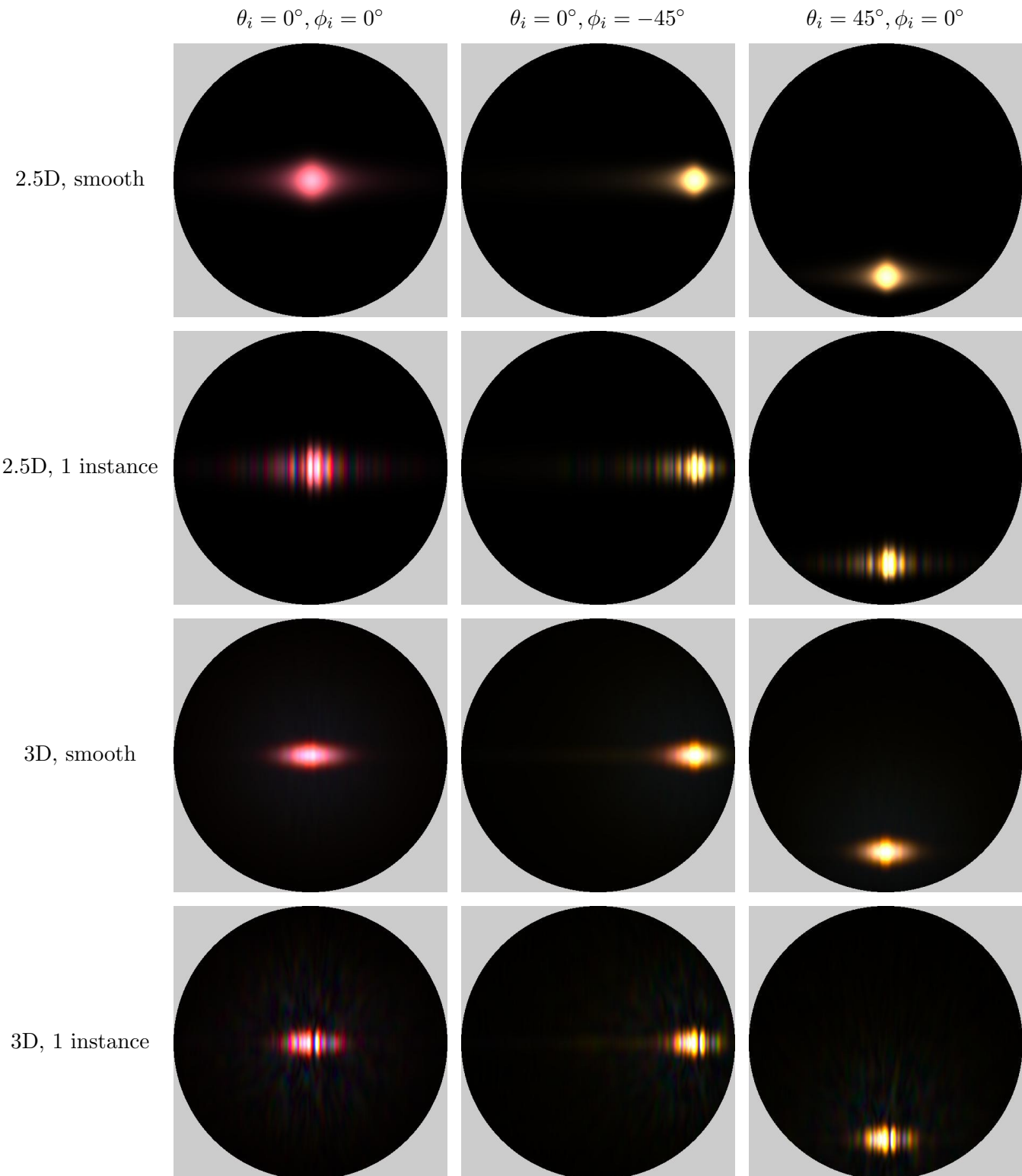


Figure 52: Comparing 2.5D and 3D BRDFs for bronzewing barbules, featuring three incident directions.

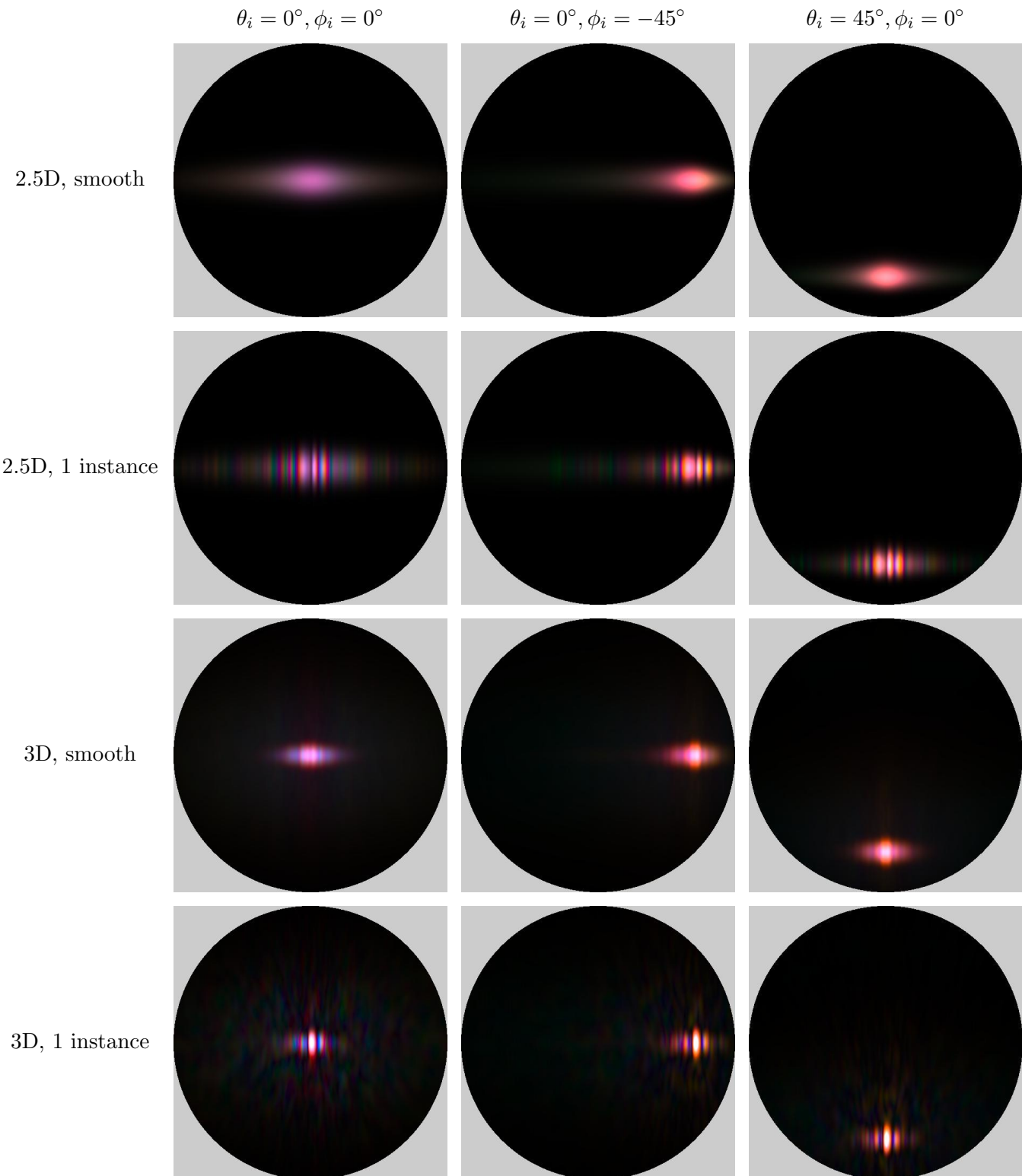


Figure 53: Comparing 2.5D and 3D BRDFs for hummingbird barbules, featuring three incident directions.

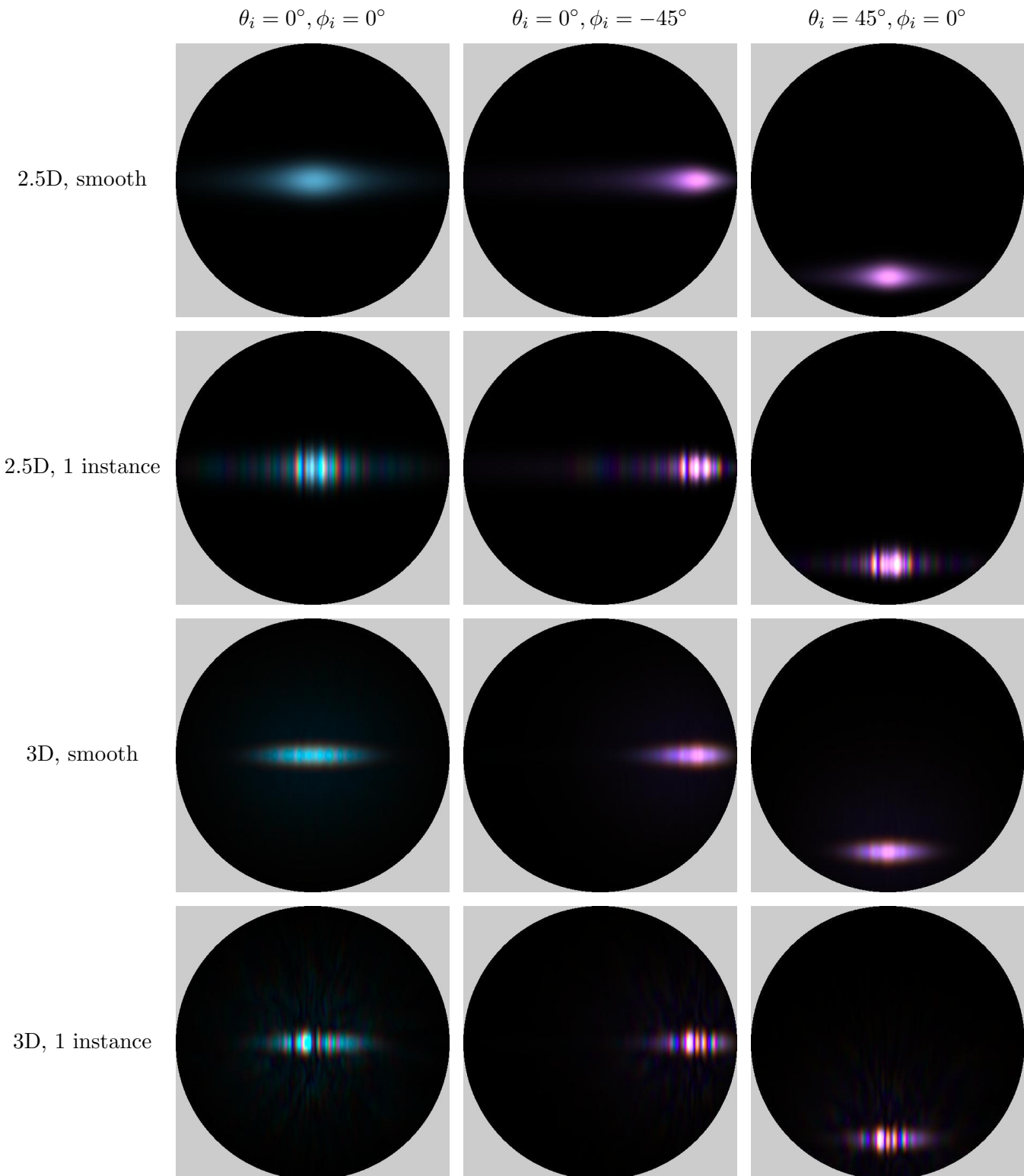


Figure 54: Comparing 2.5D and 3D BRDFs for mallard barbules, featuring three incident directions.

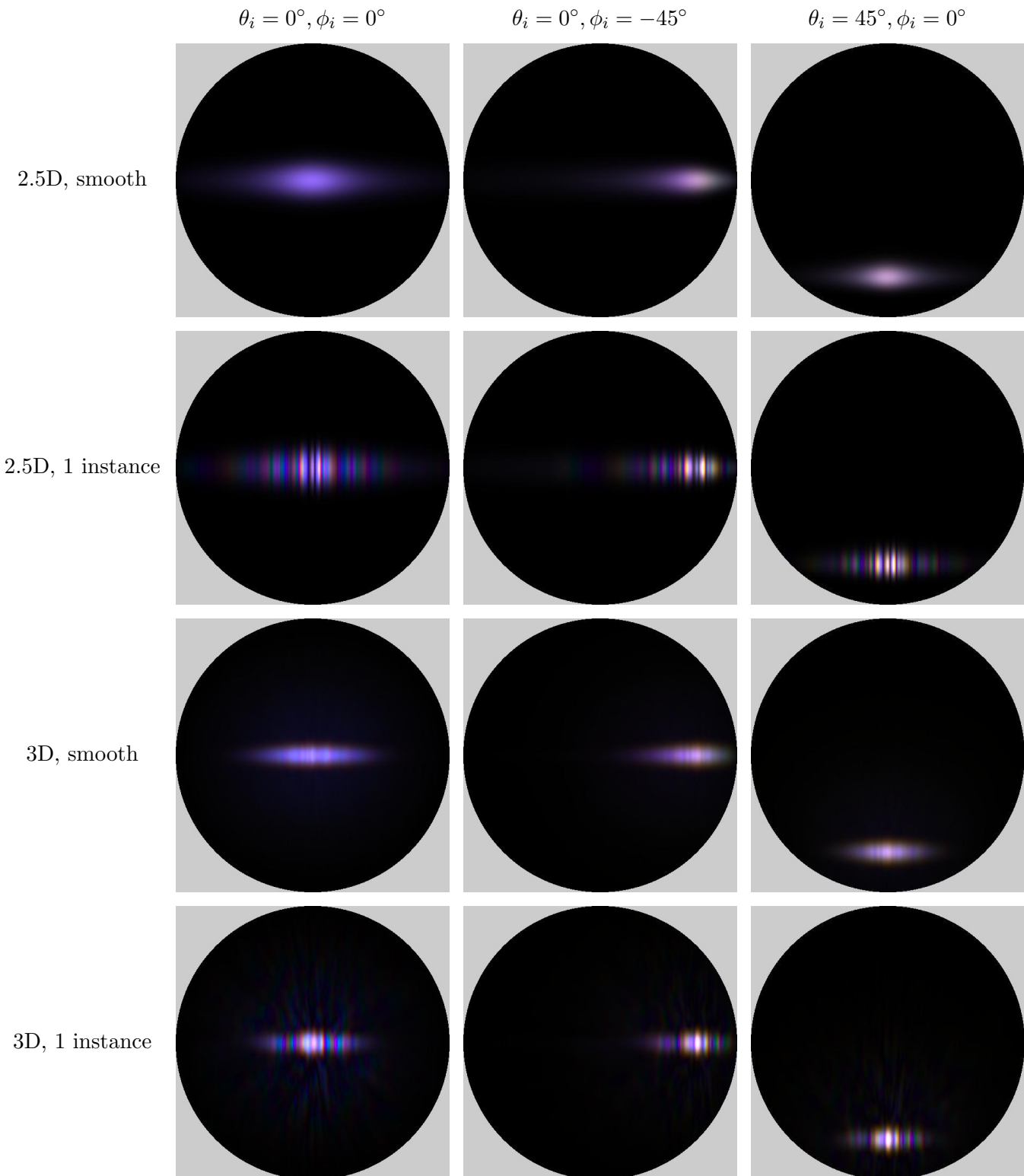


Figure 55: Comparing 2.5D and 3D BRDFs for magpie barbules, featuring three incident directions.

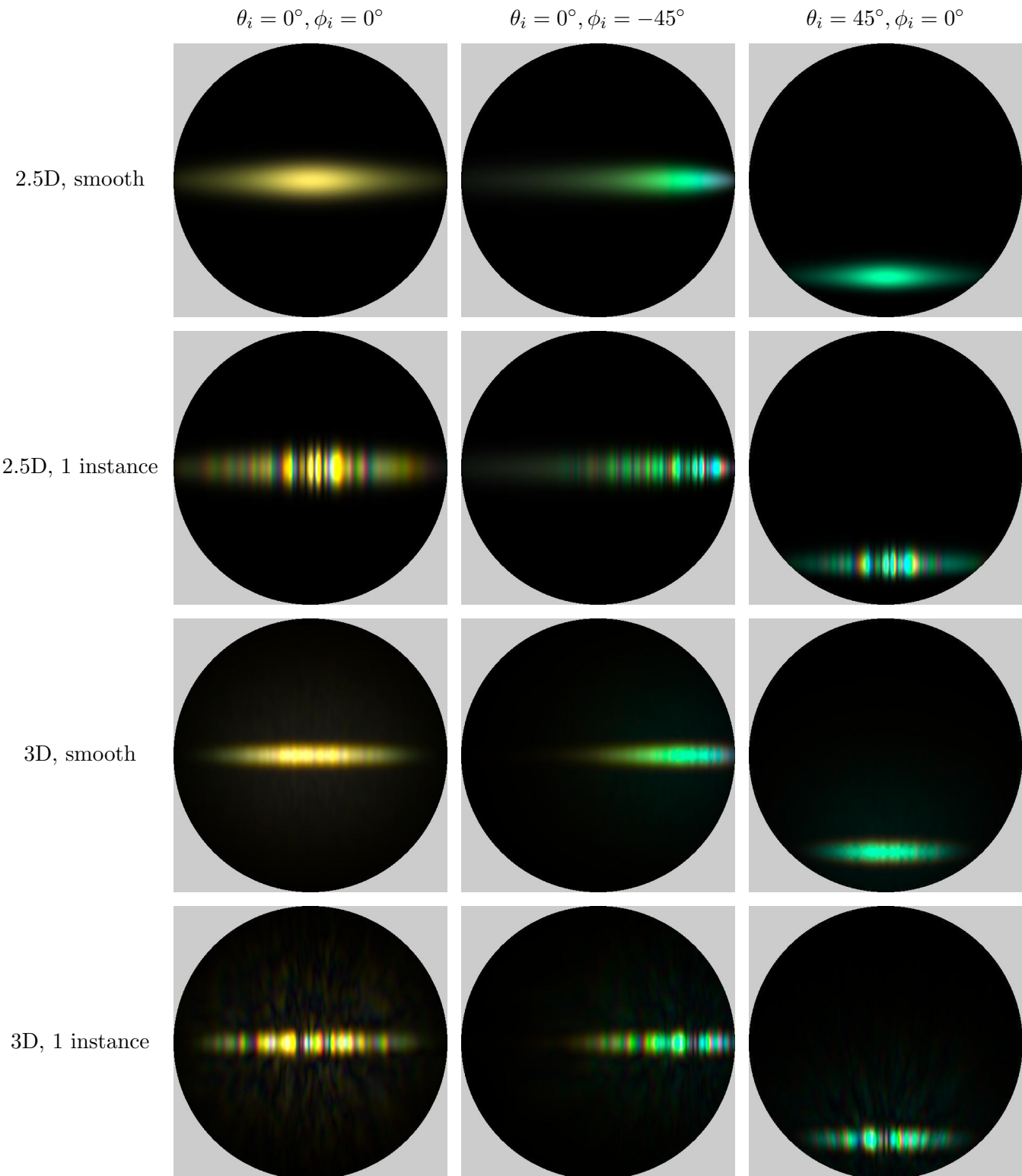


Figure 56: Comparing 2.5D and 3D BRDFs for peacock barbules, featuring three incident directions.

References

- Chad M Eliason, Rafael Maia, Juan L Parra, and Matthew D Shawkey. 2020. Signal evolution and morphological complexity in hummingbirds (Aves: Trochilidae). *Evolution* 74, 2 (2020), 447–458.
- Pascal Freyer and Doekele G Stavenga. 2020. Biophotonics of diversely coloured peacock tail feathers. *Faraday Discussions* 223 (2020), 49–62.
- Pascal Freyer, Bodo D Wilts, and Doekele G Stavenga. 2021. Cortex thickness is key for the colors of iridescent starling feather barbules with a single, organized melanosome layer. *Frontiers in Ecology and Evolution* 9 (2021), 746254.
- Marco A Giraldo, Juan L Parra, and Doekele G Stavenga. 2018. Iridescent colouration of male Anna's hummingbird (*Calypte anna*) caused by multilayered barbules. *Journal of Comparative Physiology A* 204 (2018), 965–975.
- Joseph W Goodman. 2007. *Speckle phenomena in optics: theory and applications*. Roberts and Company Publishers.
- Changhyun Han, Hanbit Kim, Hyunho Jung, Sang-Im Lee, Piotr G Jablonski, and Heonsu Jeon. 2017. Origin and biomimicry of weak iridescence in black-billed magpie feathers. *Optica* 4, 4 (2017), 464–467.
- Eri Nakamura, Shinya Yoshioka, and Shuichi Kinoshita. 2008. Structural color of rock dove's neck feather. *Journal of the Physical Society of Japan* 77, 12 (2008), 124801.
- SA Schelkunoff. 1936. Some equivalence theorems of electromagnetics and their application to radiation problems. *The Bell System Technical Journal* 15, 1 (1936), 92–112.
- Doekele G Stavenga, Hein L Leertouwer, and Bodo D Wilts. 2018. Magnificent magpie colours by feathers with layers of hollow melanosomes. *Journal of Experimental Biology* 221, 4 (2018), jeb174656.
- Doekele G Stavenga, Casper J Van Der Kooi, and Bodo D Wilts. 2017. Structural coloured feathers of mallards act by simple multilayer photonics. *Journal of The Royal Society Interface* 14, 133 (2017), 20170407.
- Shlomi Steinberg and Ling-Qi Yan. 2022. Rendering of subjective speckle formed by rough statistical surfaces. *ACM Transactions on Graphics (TOG)* 41, 1 (2022), 1–23.
- Mengqi Xia, Bruce Walter, Christophe Hery, Olivier Maury, Eric Michielssen, and Steve Marschner. 2023. A Practical Wave Optics Reflection Model for Hair and Fur. *ACM Transactions on Graphics (TOG)* 42, 4 (2023), 1–15.
- Mengqi Xia, Bruce Walter, Eric Michielssen, David Bindel, and Steve Marschner. 2020. A wave optics based fiber scattering model. *ACM Transactions on Graphics (TOG)* 39, 6 (2020), 1–16.
- Ming Xiao, Ali Dhinojwala, and Matthew Shawkey. 2014. Nanostructural basis of rainbow-like iridescence in common bronzewing Phaps chalcoptera feathers. *Optics express* 22, 12 (2014), 14625–14636.
- Yunchen Yu, Mengqi Xia, Bruce Walter, Eric Michielssen, and Steve Marschner. 2023. A Full-Wave Reference Simulator for Computing Surface Reflectance. *ACM Transactions on Graphics (TOG)* 42, 4 (2023), 1–17.